0 0 0 0 4 3 0 2 9 4 2

LBL-3758
c.1

OCT 7 1975
DOCUMENTS SECTION

DEFECTS IN BORON ION IMPLANTED SILICON

Wei-Kuo Wu
(Ph. D. thesis)

May 1975

Prepared for the U. S. Energy Research and
Development Administration under Contract W-7405-ENG-48

For Reference

Not to be taken from this room

LAWRENCE BERKELEY LABORATORY
UNIVERSITY OF CALIFORNIA
BERKELEY

LBL-3758
c.1

DISCLAIMER

This document was prepared as an account of work sponsored by the United States Government. While this document is believed to contain correct information, neither the United States Government nor any agency thereof, nor the Regents of the University of California, nor any of their employees, makes any warranty, express or implied, or assumes any legal responsibility for the accuracy, completeness, or usefulness of any information, apparatus, product, or process disclosed, or represents that its use would not infringe privately owned rights. Reference herein to any specific commercial product, process, or service by its trade name, trademark, manufacturer, or otherwise, does not necessarily constitute or imply its endorsement, recommendation, or favoring by the United States Government or any agency thereof, or the Regents of the University of California. The views and opinions of authors expressed herein do not necessarily state or reflect those of the United States Government or any agency thereof or the Regents of the University of California.

0 0 0 0 4 3 0 2 9 4 3

DEFECTS IN BORON ION IMPLANTED SILICON

Contents

Abstract v

I. Introduction 1

II. Experimental 5

1. Specimen Preparation 5

2. Sheet Resistivity Measurement 5

3. Electron Microscopy 6

III. Results 8

1. Sheet Resistivity Measurements 8

2. Transmission Electron Microscopy 8

A. General Observations 8

B. Contrast Analysis 9

C. Annealing Kinetics 19

D. On the Depth Distribution of Crystal Defects in Boron Ion Implanted Si 41

E. Direct Observation of Radiation Induced Precipitation in the High Voltage Electron Microscopy 45

IV. Discussion 51

Acknowledgements 56

References 57

Figure Captions 61

Figures 69

0 0 0 0 4 3 0 2 9 4 4

DEFECTS IN BORON ION IMPLANTED SILICON

Wei-Kuo Wu

Inorganic Materials Research Division, Lawrence Berkeley Laboratory and
Department of Materials Science and Engineering, College of Engineering;
University of California, Berkeley, California 94720

ABSTRACT

The crystal defects formed after post-implantation annealing of boron ion implanted silicon irradiated at 100 keV to a moderate dose ($2\times10^{14}/cm^2$) have been studied by transmission electron microscopy.

Both contrast analysis and annealing kinetics show that there exist at least two different kinds of linear rod-like defects along ⟨110⟩ directions. It is shown in the annealing kinetics study that one kind either shrinks steadily remaining on ⟨110⟩ at high temperatures (>850°C), or transforms into a perfect dislocation loop which rotates toward ⟨112⟩ perpendicular to its Burgers vector. The other kind shrinks steadily at moderate temperatures (~800°C). The activation energy for shrinkage of the latter kind has been determined to be 3.5±0.1 eV which is the same as the activation energy for boron diffusion in silicon. This suggests that this type of linear defect is a boron precipitate.

Besides these linear defects there are also a large number of small faulted dislocation loops on {111} planes which are hexagonal in shape and have Burgers vector a/3⟨111⟩. They grow in size during the time that the boron precipitates shrink and then subsequently shrink at higher temperature after prolonged annealing. Assuming that diffusion at 900°C takes place by motion of interstitials and that the loop shrinkage rate is emission controlled, the measured activation energy for shrinkage of these loops of 5.6±0.5 eV is consistent with the activation energy

for self-diffusion. This suggests that these interstitial dislocation loops consist mostly of silicon atoms.

In addition to the faulted dislocation loops, there also exist a large number of perfect dislocation loops with Burgers vector a/2⟨110⟩, also interstitial in nature. The loop plane for some of the perfect dislocation loop is clearly shown to be {110} with edges along ⟨110⟩ and ⟨112⟩.

The depth distribution of all these defects was determined by stereomicroscopy utilizing latex balls of diameter 1090Å±30Å as the reference points on the surface. It was shown that these boron precipitates lying parallel to the foil surfaces are at a depth of about 3500Å±600Å. The loops are also at the same depth, but with a broader spread, ±1100Å.

To further substantiate the hypothesis that the predominant type of linear defect is a form of boron precipitate silicon samples containing boron and samples containing no boron were irradiated on the hot stage in the 650 kV electron microscope. The specimens were: p-type (boron doped 0.75 Ω-cm) and n-type (phosphorous doped 2 Ω-cm) silicon. An irradiation at 620°C resulted in the growth of very long linear defects in the samples containing boron but not in the samples containing no boron.

This suggests that at 620°C silicon interstitials produced by the electron beam replace substitutional boron some of which precipitates in the form of long rods along ⟨110⟩. A similar replacement probably accounts for the observed reverse annealing stage and the growth of rod defects in boron implanted silicon.

I. INTRODUCTION

Ion implantation is the introduction of atoms into the surface layer of a solid substrate by bombardment of the solid with ions in the keV to MeV energy range.

It has proved to be a successful alternative method of introducing dopant atoms into a semicondcutor substrate. The advantage of this method for electronic circuitry is in providing a wide range of dopant species, easily introduced into any kind of substrate at quite low temperature, (usually room temperature) to an exact level of impurities, in a short time, in a very narrow region (shallow junction) near the surface. The conventional thermal diffusion method is restricted by the solid solubility of the dopant hence requiring higher diffusion temperatures (900°~1100°C) for longer times and usually produces much less sharp dopant concentration gradients.

Boron is a widely used three-valent, p-type dopant in four-valent semiconductors. It will occupy a substitutional lattice site and act as a hole which tends to absorb an electron due to its three-valent character (Fig. 1).

There has been a large volume of literatures on the electrical properties of ion implanted silicon within the past few years due to its potential of wide application in electronic circuitry. Among the electrical properties that have been investigated after ion implantation are sheet resistivity, junction location, and junction characteristics. These are determined primarily by the dopant and defect distributions, which control carrier densities, mobilities and lifetimes. A wide range of experimental techniques has been developed to determine these

properties. For example, Hall measurements or four-point probe technique combined with anodic oxidation and layer removing techniques have been successfully applied in determining the depth distribution of carriers and mobilities in both group III (B, Al, Ga and Tl) and group V (As, Sb and Bi) ion implanted silicon.[1-4] It has been found from these studies that the electrical carriers concentration[5] has a reverse annealing stage at about 600°C in boron ion implanted silicon for doses up to $10^{15}/cm^2$ (Fig. 2). A similar reverse annealing stage is also shown in the four-point probe sheet resistivity measurement (Fig. 3). However, no such reverse annealing stage is seen either for low temperature irradiation[6] (liquid nitrogen temperature) or heavy dose ion implanted silicon, where a complete surface amorphous layer is formed during irradiation.

Similar reverse annealing stages have also been seen in Al,[2] Ga[7] and P[8] ion implanted silicon.

These electrical properties have been correlated with channeling-effect measurements which detect the lattice location of boron atoms.[9-11] For lighter elements such as boron, the direct back scattering measurement[12,13] is of no use, hence a proton induced nuclear reaction, $^{11}B(P,\alpha)\,^{8}Be$, has been used to detect the lattice location of implanted boron atoms. It is shown in Fig. 4 that there are always a certain fraction of implanted boron atoms on substitutional lattice sites after implantation. There is a reverse annealing stage at about 600°C when the percentage of boron atoms on substitutional sites decreases and then increases again upon further annealing. After about 1000°C annealing, almost 90% of the implanted boron atoms become substitutional and

electrically active. Although the reverse annealing stage at about 600°C is important, not much is known about its mechanism.

Modern transmission as well as scanning electron microscopy techniques have been applied to study of the crystal defects formed during post-implantation annealing. The importance of studying these defects is that in order to recover the electrical properties after ion implantation, the implanted material has to be annealed as seen in Fig. 2, 3 and 4. One of the unavoidable effects after post-implantation annealing is the formation of defect clusters, dislocation loops, dislocation entanglements or precipitates, which may influence the electrical properties and the performance of devices.

For boron ion implanted silicon up to a dose of 10^{14} to $10^{15}/cm^2$, the crystal defects formed after post-implantation annealing are a large number of isolated dislocation loops and many linear defects along all the ⟨110⟩ directions.

Although extensive transmission electron microscopy work has been done in an attempt to identify the nature of these defects much controversy still exists. For example, the linear defects along ⟨110⟩ directions have been identified as boron precipitates,[14] lines of point defects,[15] or dislocation dipoles.[16] Similarly, the dislocation loops have been identified either as vacancy[8] or interstitial type,[17] or as perfect[17] or faulted.[8]

This thesis consists mostly of experimental results aimed at identifying the crystal defects formed during post-implantation annealing of boron ion implanted silicon to a dose of $2\times10^{14}/cm^2$.

It was found that the conventional bright field (B.F.) contrast analysis[18] was usually not enough, hence the weak-beam dark field (W.B.D.F.) technique[19] which gives very narrow images of dislocation lines was used to determine dislocation loop planes. This is crucial in the determination of loop types.[20] Although it has been found that at least two different kinds of linear defects exist due to their very narrow spacings the exact nature of these defects is still mysterious. In the present work, a newly developed outside the microscope thin film annealing technique permits repeated observation of the same defects (area) after different heat treatments.

These annealing kinetic studies, have provided new information on the nature not only of the linear defects but also of the very small dislocation loops. The stereomicroscopic technique, utilizing latex balls of diameter 1090±30Å as reference points on the foil surfaces, was also used to determine the depth distribution of defects. This gives information on the depth distribution of radiation damage during implantation and helps to clarify the mechanism of formation of linear defects.

To further substantiate the mechanism of formation of linear defects a high voltage transmission electron microscope operating at 650 kV equipped with a hot stage that can be heated up to 1000°C[21] was used to study the effect of boron atoms on the formation of linear defects.

These combined experiments utilizing contrast analysis, annealing kinetics, stereomicroscopy and high voltage transmission electron microscopy have resulted in a more complete understanding of the nature and mechanism of formation of linear and loop defects in boron implanted silicon.

II. EXPERIMENTAL

1. Specimen Preparation

n-type silicon slices, 5 Ω-cm, of ⟨111⟩ and ⟨100⟩ orientations were irradiated at room temperature with boron ions at 100 keV to a dose of $2\times10^{14}/cm^2$.

A piece of 1/2 in.×1 in. was scribed from the ⟨111⟩ slice for sheet resistivity measurements and the rest was ultrasonically cut into discs of 3 mm in diameter for transmission electron microscope observations.

The piece of sheet resistivity measurements was annealed isochronally from 400°C up to 1050°C in 50°C intravals for 20 min in a quartz tube furnace with dry nitrogen passing through it.

The discs for electron microscopical observations were annealed in the same tube furnace with dry nitrogen flow. The annealed specimens were then chemically polished from the unimplanted sides in one part solution A (2.5 g iodine and 1100 cc CH_3COOH) and two parts solution B ($1HF + 3HNO_3$).

2. Sheet Resistivity Measurement

The sheet resistivity measurements were performed by the four-point probe technique.[22]

In this technique a fixed current is injected through the two outer probes and the voltage drop is measured across the two inner probes (Fig. 5).

The sheet resistivity is then related to the current and voltage as:

$$\rho_s = C_1 C_2 \frac{V}{I}$$

ρ_s = sheet resistively

C_1 = geometrical factor depending on the shape of the specimen and the probe spacings

C_2 = doping depth correction factor

I = applied current

V = measured voltage

3. Electron Microscopy

The thinned specimens were repeatedly examined in the Philips 301 transmission electron microscope operating at 100 kV after each furnace anneal. The annealing temperatures were monitored to an accuracy within ±1°C by a chromel alumel thermocouple sealed in a small quartz tube positioned near the specimen.

It was observed that clean annealing could always be obtained not only for bulk specimens but also for thinned specimens in dry nitrogen flow up to 1000°C.

Most micrographs were taken under two beam diffraction conditions with s > o. The orientation of the micrograph was determined by making use of the Kikuchi map.

In the contrast analysis, the weak beam dark field (W.B.D.F.) technique was used to reveal the true shape of most defects, the $\vec{g}\cdot\vec{b} = o$ criterion was used to determine the Burgers vectors.

In the annealing kinetics study, great care was necessary to successfully take the specimen out of the microscope anneal it in dry nitrogen flow and then put it back. This technique not only gave a direct observation on the evolution of many defects but also can be used as a method for determining diffusion coefficients of both impurities and self-atoms.

For the measurements of depth distribution of defects, latex balls of diameter 1090±30Å were diluted in 5 cc distilled water with each drop and applied on the surfaces of the specimen. The tilting angle and tilting axis for stereo pictures were determined by making use of the Kikuchi map.

III. RESULTS

1. Sheet Resistivity Measurements

Typical sheet resistivity measurements after post-implantation annealing are shown in Fig. 3. It is seen that there exists a reverse annealing stage at about 600°C. A similar result was also reported by Bicknell et al.[14] No such reverse annealing stage is observed when the surface becomes completely amorphous during implantation.

2. Transmission Electron Microscopy

A. General Observations

For boron ion implanted silicon, the crystal defects formed after post-implantation annealing above 750°C consisted of a large number of linear defects along ⟨110⟩ directions and a large number of small dislocation loops as shown in Fig. 6.

The linear defects showed clear in-side and out-side contrast similar to that from dislocation loops (Fig. 7).[18] However, a close look at Fig. 7 shows that there exists two different kinds of linear defects showing different diffraction contrast (one shows in-side while the other shows out-side for the same diffraction conditions and vice versa) as marked by "A" and "$\bar{A}$". Nevertheless, these linear defects both go out of contrast completely when the diffracting vector is parallel to the ⟨110⟩ rod direction. This means that the Burgers vectors (if they are dislocation loops) or displacement vectors (if they are layers of impurities) are perpendicular to the elongated directions.

Besides these linear defects, there are a large number of small dislocation loops with a line of no contrast along ⟨110⟩. These are out of contrast when the operating $\bar{g}$ vector is along this ⟨110⟩ direction, see "a" and "b" in Fig. 7.

In the next sections, these defects will each be studied by contrast analysis, annealing kinetics, stereomicroscopy and high voltage hot stage transmission electron microscopy.

B. Contrast Analysis

i. Introduction

According to the two beam kinematical or dynamical theory of electron diffraction,[18] a crystal defect will give an additional phase factor,

$$e^{-2\pi i \vec{g}\cdot\vec{R}} ,$$

where $\vec{g}$ is the diffracting reciprocal lattice vector and $\vec{R}$ is the displacement or Burgers vector of the defect followed by the convention of Hirsch et al.,[18,20] in the wave equation. Hence, if $\vec{g}\cdot\vec{R} = o$, there would be no contrast due to the defect, this has been the basis for the determination of the Burgers vectors of dislocations.

It is necessary to know the inclination of the dislocation loop besides knowing the Burgers vector in order to determine the dislocation loop type, e.g., vacancy or interstitial. A quick method[23] for determining the sense of diffracting vectors unambiguously makes use of the Kikuchi pattern, so that the Burgers vectors of the dislocation loops can be determined correctly. Recently it has been reported[24] that similar small dislocation loops observed in P^+ implanted silicon show clear stacking fault fringes inside the loops. The weak beam dark field technique decreases the effective extinction distance, ξg, and gives a very sharp, narrow image of the dislocation lines (width of dislocation line $\sim 1/3\xi g$), so that the oscillating fringe contrast of the stacking fault can be seen clearly and the shape and loop can also be determined.

In the following contrast analysis, the W.B.D.F. technique is used extensively together with conventional B.F. and stereomicroscopy to reveal the dislocation loop plane by trace analysis and the stacking fault fringe contrast for small faulted dislocation loops.

ii. Determination of Dislocation Loop Types

a. For faulted dislocation loops. Figure 8 is a set of W.B.D.F. pictures of the same area with the diffracting vectors as indicated ($s > o$, where $\vec{s}$ is the deviation vector away from exact Bragg condition).

It is seen in Fig. 8, A and B, that most of the small dislocation loops are hexagonal in shape with edges along ⟨110⟩ directions. From trace analysis, loops a, b and c are clearly shown on the inclined {111} planes, while d is on the foil plane. This is further proved as shown in Fig. C, D, E and F of this sequence, when the foil was tilted from ⟨111⟩ orientation to ⟨112⟩ orientations so that loop c and a are showing edge-on in Fig. C and E respectively.

It is noted that loop b and c show in-side and out-side contrast when the diffracting vector $\vec{g}$ is inclined to the loop planes as in Fig. A and B, while loops a and d are showing residual contrast[18] ($g \cdot b = o$ and $\vec{g} \cdot \vec{b} \times \vec{u} \neq o$ where $\vec{u}$ is along the dislocation line), if the diffracting $\vec{g}$ vector is on the loop planes. These observations are all consistent with the assumption that loops of this kind are faulted Frank partial dislocation loops[25] with Burgers vectors, a/3⟨111⟩, perpendicular to the {111} loop planes.

Although it is not possible to see fringes due to the stacking fault in this set of pictures, the bright centers of the loops in Fig. C through E suggest that the fringes are too close together to be resolved.

In Fig. 9, where larger loops of the same kind are observed under similar conditions, the fringe contrast is clearly resolved. The fringes are parallel to the foil surface for those loops that were cut by the surface such as loop A as is expected from the contrast theory. However, the fringes appear to be bent so as to be parallel to the near by bonding partial dislocation lines for those loops that are completely inside the foil, e.g., loop B or E. Similar contrast is also observed in the bright field pictures as shown in Figs. 28-30. This result raises some interesting questions as to what factors determine the fringe contrast of stacking faults of small faulted dislocation loops. The fringe contrast is further evidence that all these small loops are Frank partial dislocation loops.

The contrast due to stacking faults and bounding partials were reported in detail by Booker and Tunstall[26] for the two dimensional defects present in silicon after annealing in air. In their case, the defects were very large so that both the fringes of the stacking faults and the contrast due to the bounding partials could be seen unambiguously. For the very tiny Frank loops observed in this case, an alternative method has to be used to identify the nature of these defects. Tunstall[27] has made some theoretical contrast calculations to prove the validity of utilizing the sign of $(\vec{g}\cdot\vec{b})s$ as a criterion for determining the sign of $\vec{b}$ (the sign of the Burgers vector $\vec{b}$ of a dislocation loop could always be either positive or negative as determined by $\vec{g}\cdot\vec{b} = o$ alone). He concluded that Frank loops with $(\vec{g}\cdot\vec{b})s$ positive would appear smaller than when $(\vec{g}\cdot\vec{b})s$ was negative. This was the same criterion used in determining the sign of b for perfect dislocation loops.[18,20] Tunstall[27] also pointed

out that $|\vec{g}\cdot\vec{b}| = 1/3$ might not be useful in determining the size of the loop since the contrast due to bounding partials should be weak.[28] He suggested an alternative method,[29] with $\vec{g}\cdot\vec{b} = +2/3$ (s > o) showing good contrast and $\vec{g}\cdot\vec{b} = -2/3$ (s > o) showing weak or invisible contrast, that enables the nature of partial dislocations to be determined. However, this method is again the same as utilizing the sign of $(\vec{g}\cdot\vec{b})s$ as criterion, so that loops with $(\vec{g}\cdot\vec{b})s > o$ (no matter 1/3, 2/3 or 4/3) would show strong, in-side contrast while $(\vec{g}\cdot\vec{b})s < o$ would show weak, invisible or out-side contrast of the partials. This is shown to be true in Fig. 8, for all small faulted loops.

The contrast of these very small Frank dislocation loops are tabulated in Table 1. It is concluded that all these loops are interstitial type lying on all four possible {111} planes.

b. <u>For perfect dislocation loops</u>. Besides these small faulted Frank dislocation loops, there are also some perfect dislocation loops with loop planes either {111} or {110}.

A typical example is shown in Fig. 8. Loop $\bar{C}$ with an elongated direction along $[01\bar{1}]$ lying on $(\bar{1}\bar{1}\bar{1})$ plane as determined from trace analysis. It shows strong in-side and out-side contrast when the operating $\bar{g}$ vector is on the loop plane (Fig. 8A and B). This excludes the possibility of its being faulted with Burgers vector a/3[111]. However, it did show weak residual contrast (also shown by loop "d" in Fig. A and B), which is characterized by remaining the same size, when the g vector is reversed in the direction in Fig. 8E and F. The contrast of this loop is also tabulated in Table 1. It is concluded that this perfect loop,

Table I.

	$\vec{g}$			$\vec{n}$	$\vec{b}$	$\vec{b}\cdot\vec{n}$	Type
	$[2\bar{2}0]$	$[\bar{1}11]$	$[11\bar{1}]$				
a	R	O	E-O	$[\bar{1}\bar{1}1]$	$a/3[111]$	Neg.	Int.
b	I	O	I	$[\bar{1}1\bar{1}]$	$a/3[1\bar{1}1]$	Neg.	Int.
c	O	E-O	O	$[1\bar{1}\bar{1}]$	$a/3[\bar{1}11]$	Neg.	Int.
d	R	I	I	$[\bar{1}\bar{1}\bar{1}]$	$a/3[111]$	Neg.	Int.
$\bar{c}$	O	I	R	$[\bar{1}\bar{1}\bar{1}]$	$a/2[011]$	Neg.	Int.

R: Residual Contrast ($\vec{g}\cdot\vec{b} = 0$; $\vec{g}\cdot\vec{b}\times\vec{u} \neq 0$)
I: Inside Contrast
O: Outside Contrast
E-O: Edge-on
Neg: Negative Value
Int: Interstitial Type

XBL 753-5928

0 0 0 0 4 3 0 2 9 5 1

is interstitial in nature, lies on (111) and, has a Burgers vector perpendicular to its elongated direction.

In another example shown in Fig. 10, a very large perfect dislocation loop A (no stacking fault fringes or dark center) with edges of the loop lying along either ⟨110⟩ or ⟨112⟩ directions is observed together with faulted Frank loops B and C lying on the inclined {111} planes. From trace analysis, loop A is lying on $(\bar{1}0\bar{1})$ plane. The loop shows residual contrast when the operating $\vec{g}$ vector is parallel to the loop edges along $[10\bar{1}]$ direction. This shows that the Burgers vector is a/2[101] perpendicular to both the loop edges along the $[10\bar{1}]$ direction and the loop plane. Hence, it is a pure edge interstitial typed dislocation loop. This big loop slipped out of the foil during further annealing as shown in Fig. 10b.

Besides these regularly shaped perfect dislocation loops, many irregularly shaped perfect dislocation loops were also observed, which tended to lie with long dimensions along ⟨112⟩ directions and with Burgers vectors perpendicular to the ⟨112⟩ direction. A typical example is shown in Fig. 17, where one end of the linear defect B suddenly broke up and became a dislocation loop C which continued to rotate so as to lie along $[\bar{1}\bar{1}2]$ (Fig. 17a through f). The loop C has a different displacement vector from that of the linear defect B from which it originated as shown in Fig. 11g and h. When the $\vec{g}$ vector is parallel to $[20\bar{2}]$, loop C shows strong contrast while defect B is out of contrast. However, if the $[\bar{1}\bar{1}1]$ diffracting vector is used, defect B is in contrast and loop "C" shows weak residual contrast. This suggests that loop C has a perfect

Burgers vector perpendicular to its elongated ⟨112⟩ direction.

iii. On the Contrast Study of Linear Defects

As was pointed out in Fig. 7, the observation of two kinds of linear defects, one showing outside contrast while the other shows inside contrast may indicate that one is vacancy type while the other is interstitial type but with the same inclination with respect to the electron beam. They may also be of the same type, e.g., both vacancy or both interstitial, but having opposite inclinations as shown in Fig. 11. Since both kinds of linear defects disappear when the operating $\vec{g}$ vector is along the elongated ⟨110⟩ direction, this indicates that the displacement vectors of both are perpendicular to the elongated ⟨110⟩ directions. However, for each ⟨110⟩ direction, this leaves at least three low index possibilities for displacement vector, e.g., a/x⟨110⟩, a/x⟨111⟩ and a/x⟨100⟩ where x may not be an integer. The existence of more than one kind of defect has not previously been pointed out. Madden and Davidson[16] concluded that the linear defects were lying on {100} planes with Burgers vectors a/x⟨100⟩ perpendicular to them and interstitial in nature.

It is found that in order to determine the Burgers vector of displacement vector unambiguously by contrast analysis, observation of the same defect for many different $\vec{g}$ vectors is desirable. Hence, a ⟨100⟩ oriented foil was used in place of ⟨111⟩ foils and the selection of g vector was facilitated by a high angle tilting stage which could be rotated up to 60° in any direction.

A typical example is shown in Fig. 12. Figures 12a through h were taken near [001] orientation. The foil was then rotated to [011] and

[$0\bar{1}1$] orientations with the diffracting g vectors as indicated (Fig. 12i through l). It is seen that linear defects a and d are showing very weak contrast in [001] orientation, while "A", "$\bar{A}$" and "D" are showing strong in and outside contrast. When the foil is tilted away from [001] to either [$\bar{1}01$] or [011] orientation, a and d also show strong contrast too. It is noted that A and $\bar{A}$ show different contrast in Fig. 12a and b. As mentioned before, this might be due to the fact that they are either of different types or that they have different inclinations. The different contrast of A and $\bar{A}$ is also shown in Fig. 12i and j, where defect $\bar{A}$ shows strong but same contrast when the $\vec{g}$ is reversed in direction (typical of an edge-on view) while defect A shows very weak residual contrast. The reverse is observed in Fig. 12k and l.

A complete contrast analysis starting with all possible displacement vectors of these linear defects is tabulated in Table II. It is observed that only a Burgers vector along the [$\bar{1}\bar{1}\bar{1}$] direction (here we ignore the magnitude of the Burgers vector) satisfies all the observec contrast observations for loop A, the other possible Burgers vectors can not satisfy the observed contrast either in [011] or [$0\bar{1}1$] orientation. Similarly, only [$11\bar{1}$] and [$\bar{1}1\bar{1}$] satisfies all observed contrast for loop $\bar{A}$ and D. The loop plane for loop A, $\bar{A}$ or D is obtained from the orientation where it shows edge-on. It is, therefore, concluded that loop A, $\bar{A}$ and D observed in this case are elongated faulted Frank dislocation loops, interstitial in nature.

The very weak contrast for defects a and d in [001] orientation with all different diffracting $\vec{g}$ vectors suggests that the Burgers vector is parallel to the beam direction, e.g., ±[001]. The weak contrast is,

Table II. Diffracting contrast of rod-like defects with different g vectors.

Loop No.	$\vec{g}$: $\hat{n}=[001]$ [220]	[2$\bar{2}$0]	[$\bar{4}$00]	[040]	$\hat{n}=[0\bar{1}1]$ [022]	$\hat{n}=[011]$ [0$\bar{2}$2]	Possible $\vec{b}$	$\vec{b}$	$\vec{n}$	$\vec{b}\cdot\vec{n}$	Type
A	O	N	I	O	E-O	R	[$\bar{1}\bar{1}$0][00$\bar{1}$] [$\bar{1}\bar{1}\bar{1}$][$\bar{1}\bar{1}\bar{1}$]	[$\bar{1}\bar{1}\bar{1}$]	[111]	-	Interstitial
$\bar{A}$	I	N	O	I	R	E-O	[110][00$\bar{1}$] [111][11$\bar{1}$]	[11$\bar{1}$]	[$\bar{1}\bar{1}$1]	-	Interstitial
D	N	O	I	I	R	E-O	[$\bar{1}$10][00$\bar{1}$] [$\bar{1}$11][$\bar{1}$1$\bar{1}$]	[$\bar{1}$1$\bar{1}$]	[1$\bar{1}$1]	-	Interstitial
a	R	N	R	R	O	O		[00$\bar{1}$]	[001]	-	Interstitial
b	E-O	E-O	E-O	R	H-O	N		±[100]			
c	E-O	E-O	R	E-O	I	I		±[010]	±[0$\bar{1}$0]	-	Interstitial
d	N	R	R	R	O	O		[00$\bar{1}$]	[001]	-	Interstitial
e	E-O	E-O	R	E-O	I	I		±[010]	±[0$\bar{1}$0]	-	Interstitial
f	E-O	E-O	E-O	R	N	H-O		±[100]			

O Outside Contrast
I Inside Contrast
R Residual Contrast; $\vec{g}\cdot\vec{b} = 0$, $\vec{g}\cdot\vec{b}\times\vec{u} \neq 0$
N No Contrast; $\vec{g}\cdot\vec{b} = 0$, $\vec{g}\cdot\vec{b}\times\vec{u} = 0$
E-O Edge-On
H-O Head-On

0 0 0 0 4 3 0 2 9 5 3

therefore, due to the residual contrast.[18] From the contrast observed in [011] and [0$\bar{1}$1] orientations, the Burgers vector for defect a and d is further substantiated to be [00$\bar{1}$]. The magnitude of the Burgers vector is tentatively assigned as a/x. The loop plane is very difficult to determine in this orientation, since a tilting of up to 90° may be required to make it show edge-on. However, some defects d which show clear in and outside contrast in both [0$\bar{1}$1] and [011] orientations as shown in Fig. 12i through l, is, therefore, not lying on {111} planes. It can not also lie on the {110} plane which is parallel to the displacement vector. In an ⟨111⟩ foil, the spacing of a similar defect C in Fig. 8i was observed to increase as tilted from ⟨111⟩ to ⟨112⟩ orientation (comparing the spacing of defect C in Fig. b and e). This excludes the possibilities of either {111} or {110} habit planes which should correspond to a decrease in the spacing of the defect when tilted from ⟨111⟩ to ⟨112⟩ and is consistent with the idea that linear defect of this kind are lying on the {100} planes.

The existence of linear defects lying on {100} planes with a/x⟨100⟩ Burgers vectors is further substantiated from the contrast observations for these defects along the inclined ⟨110⟩ directions, e.g., b, c, e and f in Fig. 12. These defects all show about the same kind of contrast when the $\vec{g}$ is reversed in direction (typical of an edge-on view) in Fig. 12a to d. They show very weak or invisible contrast when the $\vec{g}$ vectors are parallel to the projected elongated loop directions in Figs. 12e to h. The complete contrast analysis for these defects is also tabulated in Table II. It is noted that the signs of plane normal

and Burgers vector for defect c and e suffer an inversion from $[0\bar{1}1]$ to [011] orientation following the convention of Hirsch et al.[18] However, they are still interstitial in nature. The sign of plane normal for defect b or f is undetermined, since the habit plane is always parallel to the electron beam.

From these results and that in the previous section, it is concluded that there are at least three kinds of linear defects, two kinds are on the {111} planes with Burgers vectors of a/3⟨111⟩ type perpendicular to the loop plane or of a/2⟨110⟩ type* still perpendicular to the elongated direction. The other type is on {100} with Burgers vector a/x⟨100⟩ perpendicular to the loop plane. They are all interstitial in nature.

The different contrast of linear defects lying along the same direction as observed in Fig. 7 is due to the defects being of different inclinations instead of being of different types (Fig. 11).

C. Annealing Kinetics

i. Introduction

In the previous contrast analysis, the Burgers vectors or displacement vectors and the habit planes of all defects including dislocation loops and linear defects are determined. However, a layer or layers of impurities may show similar contrast as a dislocation loop, so that there is no way to distinguish a plate of impurities from a layer of self atoms by contrast analysis alone. Also it is not clear from the contrast analysis why there exists at least two major kinds of linear defects with different displacement vectors and habit planes? Nor is it understood how irregularly

*Since this type of linear defect is rarely seen and usually shorter and fatter, hence it will not be treated as linear defect in the following sections. In the following sections, type A and $\bar{A}$ are assigned to the linear defects on {111} and {100} planes respectively.

shaped perfect dislocation loops which are sometimes connected to linear defects are formed.

In order to resolve these problems, repeated observations of the same defect during an annealing sequence at different annealing temperatures and for different times were made. The aim was to find out the activation energy for diffusion of the atoms that these defects are composed of. This method also provides direct observation on the evolution of all defects, so that their true natures can be more fully understood.

ii. General Observations

In order to find out the temperature range where these defects would start to shrink, an isochronal annealing sequence from 800°C up to 1050°C for 20 min with 50°C intervals was performed. The following results were obtained.

a. The existence of two kinds of linear defects. This is clearly shown in Figs. 13 and 14. Type $\bar{A}$ and A defects are parallel to each other but show different kinds of contrast (one shows outside contrast while the other inside and vice versa). Type $\bar{A}$ usually shrinks much faster than type A and completely disappears after about 950°C. Though type A sometimes show drastic irregular shrinkage as in Figs. 13a and b, yet it will shrink continuously up to 1050°C and show clear stacking fault fringes. This is consistent with the conclusions of the contrast analysis that one kind of linear defect is a faulted Frank dislocation dipole. It is also noted that the widths of type $\bar{A}$ defects remain the same during their shrinkage, while the widths of type A increase.

b. The transformation of type A linear defects into a perfect elongated dislocation loop that then rotates to a ⟨112⟩ direction. This is chown in Fig. 15, where a type A linear defect similar to that found in Fig. 14 suddenly changes into a perfect dislocation loop and rotates into a ⟨112⟩ direction with its new Burgers vector perpendicular to its elongated direction. A similar example is shown in Fig. 15A.

c. The nucleation and growth of a perfect dislocation loop when type $\bar{A}$ linear defects are shrinking. This is shown in Fig. 16, where a perfect dislocation loop B is formed adjacent to the linear defect $\bar{A}$. This perfect dislocation loop has an elongated direction and tends to lie parallel to a ⟨112⟩ direction with its Burgers vector perpendicular to it. It grew when the linear defect $\bar{A}$ was shrinking. Another example is shown in Fig. 17.

d. The evolution of irregularly shaped dislocation loops. Irregularly curved dislocation loops such as loop A and B in Fig. 18 were also observed. They also show a tendency to lie along a ⟨112⟩ direction with a Burgers vector perpendicular to it.

e. Breaking up of elongated dislocation loops into strings of smaller loops. Though loop A in Fig. 18a appears to be starting to break up into smaller loops, no such sequence of breaking up has ever been observed in the annealing sequences carried out on thin foils. However. when a thick sample was annealed up to 1050°C before thinning, the elongated dislocation loops (type A linear defects) would break up into strings of smaller loops as shown in Figs. 19, 28 and 29. The absence of strings of smaller loops during thin foil annealing shows that the free surface plays an important role in determining whether an elongated

dislocation loops will shrink steadily from its ends as in Figs. 13 or 14, or first break up into strings of smaller loops.

f. <u>The evolution of small dislocation loops</u>. The small dislocation loops formed along with the linear defects first grow in size even in a thin foil when the type $\bar{A}$ linear defects are shrinking. At a later stage they then shrink too. This is shown in Fig. 20, where small loop 3 (Frank loop) and 4 (perfect loop) both grow in size as the linear defects are shrinking as shown in Figs. 20a through c. They subsequently shrink and disappear after the type $\bar{A}$ linear defects have been annealed out (Figs. 20d and e).

g. <u>Interactions between dislocation loops</u>. During high temperature annealing, the mobility of dislocations increases. Therefore, mutual interaction may cause displacement.

A typical example is shown in Fig. 21, where a more mobile perfect dislocation loop B on the inclined $(\bar{1}1\bar{1})$ plane with a Burgers vector $a/2[1\bar{1}0]$ perpendicular to its long direction is influenced strongly by the strain field of a near-by faulted Frank dislocation loop A also on the same plane. A schematic illustration of the interaction between these loops is shown in Fig. 22. This interaction can be represented by their Burgers vectors.

$$\vec{b}_1 + \vec{b}_3 \rightarrow \vec{b}_2$$

$$a/3[1\bar{1}1] + a/6[1\bar{1}\bar{2}] \rightarrow a/2[1\bar{1}0]$$

$$b^2 \qquad \frac{1}{3}a^2 \qquad \frac{1}{6}a^2 \qquad \frac{1}{2}a^2$$

It is noted that the recombined segment of the dislocation loops has a Burgers vector $\vec{b}_3$ and elastic energy (αb^2) smaller than both $\vec{b}_1$

and $\vec{b}_2$. The recombination is, therefore, energetically favorable. $\vec{b}_3$ also lies on the loop plane, so that it can glide easily into loop A and sweep away the stacking fault as shown by the disappearance of the dark center in loop A.

Another kind of interaction between dislocation loops of the same kind is shown in Fig. 28, where two Frank dislocation loops on the same plane climb together and coalesce at A.

iii. On the Annealing Kinetics of Type $\bar{A}$ Linear Defects

a. Introduction. From the contrast analysis, type $\bar{A}$ linear defects show contrast similar to that expected for an elongated dislocation loop on {100} with displacement vector a/x⟨100⟩ perpendicular to the elongated ⟨110⟩ direction and loop plane.

The above characterization confirms that of Madden and Davidson.[16] They also reported that these linear defects should be composed mostly of silicon atoms since they were also observed in Neon[30] and high energy electron[31] irradiated silicon.

However, the annealing study in the previous section indicated that type $\bar{A}$ linear defects shrank steadily and disappeared completely at a lower temperature range than type A linear defects. This fact suggests that these two types of linear defects may be composed of different atoms with different thermal diffusion coefficients which control the shrinkage rate.

In order to investigate this possibility a more extensive set of annealing observations was conducted in the temperature range from 750°C to 850°C. The activation energy for shrinkage of type $\bar{A}$ defects was determined.

b. Model for shrinkage of an elongated dislocation loop.

Dislocation loops tend to shrink during annealing due to the line tension of the dislocation[32] and the energy of the stacking fault. The type $\bar{A}$ linear defects have very narrow spacings and straight edges along ⟨110⟩ directions. Because they are probably more widely dissociated on the long sides and because the climb force on the dislocation is greater at the ends it is not surprising that the defects are observed to shrink in length during annealing without any apparent change in width.

It was pointed out by Seeger[33] that self-diffusion in silicon below 900°C was possibly controlled by a vacancy mechanism. The vacancy self-diffusion mechanism was assumed to operate in the temperature range from 750°C to 850°C in the following analysis.

The ends of the dislocation loops act like point sinks for vacancies migrating from the foil surfaces which cause the dislocation loops to shrink. At steady state, the concentration of vacancies between the foil surfaces and the ends of the loop near the center of the foil of thickness 2ℓ can be expressed as (based on a spherical diffusional geometry):

$$C(r) = \frac{C_o^V\left[r\left(\ell - R\cdot\exp\frac{-\mu_v}{2kT}\right) - R\ell\left(1 - \exp\frac{-\mu_v}{2kT}\right)\right]}{r(\ell - R)} \qquad (1)$$

where μ_v is the chemical potential of vacancies at the dislocation loop due to the line tension and stacking fault energy.

$$\mu_v = \frac{Gb^2B^2}{4\pi(1 - \nu)\,R}\ln\frac{R}{r_o} + \gamma B^2$$

and G is the shear modulus of silicon

ν is the Poisson's ratio of silicon

b is the Burgers vector of the dislocation loop

B^2 is the cross sectional area of an atom on the loop plane

γ is the stacking fault energy of silicon

r_o is the dislocation core radius

C_o^v is the equilibrium vacancy concentration at the foil surface

$2R$ is the width of the dislocation loop.

(The factor 2 occurred in the exponent in Eq. (1) because each lattice point is associated with two atoms in diamond cubic lattice.)

The flux of vacancies at the ends of the dislocation loop, which causes it to shrink is:

$$F = -D_m^v N_o \left.\frac{\alpha C}{\alpha r}\right)_R \simeq \frac{-D_m^v C_o^v N_o}{R}\left(1 - \exp - \left(\frac{\mu_v}{2kT}\right)\right) \qquad (2)$$

where D_m^v is the vacancy migration coefficient

N_o is the atomic density of silicon.

The number change of atoms inside each loop is, therefore, expressed as:

$$\frac{dN}{dt} = \frac{d\,\frac{L\times 2R\times 2}{B^2}}{dt} = 4\pi R^2(F) \qquad (3)$$

hence;

$$\frac{dL}{dt} = -\pi B^2 N_o D^{SD}\left(1 - \exp - \left(\frac{\mu_v}{2kT}\right)\right) \qquad (4)$$

where $D^{SD} = D_m^v C_o^v$ is the self-diffusion coefficient for silicon.

c. Model for shrinkage of sheets of boron atoms of n-layers thick. Sheets of impurities, like partially-coherent precipitates, will also show contrast similar to that of dislocation loops.[18] The driving force for shrinkage of this kind of precipitate contains terms similar to the above except that it envolves diffusion of the solute atoms. Assuming that the type $\bar{A}$ linear defects are boron precipitates with a boron concentration approaching one, the boron density in silicon after boron ion implantation at 100 keV to a dose of 2×10^{14} B/cm^2 distributed uniformly through a depth of 6000Å would be only about 3×10^{18} atom/cm^3, as compared to the atomic density of silicon, 5×10^{22} Si/cm^3. Therefore, boron precipitates will tend to redissolve by thermal diffusion during annealing.

Based on a spherical diffusion geometry, the shrinkage rate of a linear defect composed of impurities can be expressed as:

$$\frac{dL}{dt} = -\frac{2\pi B^2 N_o D^B}{n}(C_s - C_o) \qquad (5)$$

where, D^B is the diffusion coefficient for boron in silicon

$= D_o^B \exp - \frac{Q}{kT}$

n is the number of layers of impurities

C_s, C_o are the impurity concentrations at the defects and free surfaces respectively.

d. Results. In order to avoid the errors inherent in comparing shrinkage rates of different defects that may have different widths and be at different depths the same defects (same area) were studied at different annealing temperatures for different times.

A typical annealing sequence is shown in Fig. 24. Again it is shown that small interstitial type dislocation loops, e.g., b and g in

Fig. 24, are growing while the type $\bar{A}$ linear defects are shrinking. It is also shown that a small perfect dislocation loop a is nucleated or grows to a visible size and continues to grow while linear defect 1 is shrinking. The growth of these dislocation loops is thought to be caused by their acting as vacancy sources similar to the behavior observed during Cu precipitation in Si[34] or NbC precipitation in austenitic stainless steel.[29] These dislocation loops can cause a near-by linear defect to shrink rapidly as long as its end is near a loop. This is shown by the shrinkage of linear defect 1 in Fig. 24 which is near a number of loops. Its shrinkage rate is shown as curve (1) in Fig. 25. Sometimes, they can even cause an originally single defect to break up into two as shown by loop g in Fig. 24. These results strongly suggest that the shrinkage of linear defects in this temperature range is diffusion controlled instead of emissional controlled.

For linear defects such as 4 and 5 in Fig. 24 which are far away from internal vacancy sources such as interstitial loops, the shrinking rates are very regular as shown by curves (4) and (5) in Fig. 25. This behavior has been confirmed by many other similar defects. It is also noted that the type A linear defects such as 3 in Fig. 24 occasionally shrinks rather drastically and becomes wider, but mostly shows a much slower shrinking rate as shown by the dotted lines in Fig. 25.

From Eqs. (4) or (5) in the previous sections, it is shown that the shrinkage rate (length change) of linear defects should be constant at constant temperature. The temperature dependence of the shrinking rate for a given defect is, therefore, determined by the diffusion coefficient, i.e., D^{SD} or D^{B}.

Plotting the logarithmic shrinking rates of these linear defects with respect to the reciprocal of the annealing temperatures (Fig. 26), an Arrhenius plot is obtained which gives an activation energy of 3.5±0.1 eV, which corresponds to that of diffusion of boron atoms in silicon.[35]

If all known parameters are inserted into Eq. (4), it is shown that

$$\frac{dL}{dt} \doteq -2.5\times10^{8}\times D^{SD}\ \frac{cm}{sec} \quad .$$

Since D^{SD} is only about 10^{-20} cm^2/sec at 802°C,[33] hence the resultant shrinking rate based on the shrinkage of dislocation loops of self atoms would be at least 1000 times smaller than observed in Fig. 25.

However, putting reasonable values into Eq. (5), the calculated result fits the observed rate, if sheets of boron atoms of 12 layers are assumed.

e. Discussion and conclusions. From the temperature dependence and the magnitude of the shrinkage rate of type $\bar{A}$ linear defects it is concluded that they are boron precipitates. Although they show a contrast similar to that of a dislocation loop on {100} planes with Burgers vector a/x⟨100⟩ perpendicular to both the ⟨110⟩ elongated direction and to the loop plane, however, they are apparently coherent precipitates of boron atoms several layers thick (possibly 12) on {100} planes.

The mechanism that causes their growth may be similar to that proposed by Watkins and Corbett[36] for electron irradiated Al-dopped silicon where interstitial silicon eject the substitutional Al impurity atoms from substitutional sites. A difference between Al dopped silicon

and this case is that an Al atom is much larger than silicon, while a boron atom is smaller. This should tend to make displacement of a boron atom by a silicon interstitial even more likely. Ion implantation produces a large number of supersaturated silicon interstitials or very small clusters of silicon interstitials. During low temperature post implantation annealing the latter probably break up and then displace boron atoms which have already found a substitutional site after implantation as shown in Fig. 4. These interstitial boron atoms then diffuse rapidly at the annealing temperature and precipitate out as linear defects. The 600°C reverse annealing phenomenon observed in the electrical measurements is probably related to this displacement of boron from substitutional sites. Since the silicon single interstitial is thought to have a low activation energy for migration ($E_I^M \approx 0.8$ eV),[33] this temperature probably corresponds to the break up of small interstitial clusters into single interstitials which then displace boron atoms. Since the linear boron precipitates observable in the transmission electron microscope are seen only after 750°C annealing which is at least 150°C higher than the temperature that reverse annealing occurs, this indicates that the boron interstitials are not mobile until at least 750°C. To a first approximation, the diffusion length, $\sqrt{D^B t}$, of boron atoms in silicon is 0.84Å at 600°C as compared to 26Å at 750°C for 20 min annealing. So that as the annealing temperature is raised, the locally supersaturated interstitial boron atoms diffuse rapidly and precipitate out as rod defects.

These linear boron precipitates tend to be redissolved by thermal diffusion at higher annealing temperature, because the density of boron

atoms a short distance away from the precipitates is always much lower than the solid solubility of boron in silicon. This is shown in Fig. 2, where the boron concentration at the peak region after implantation to a dose 10 times larger than the present case is still much smaller than the solid solubility. (The solid solubility of boron in silicon at 800°C is about 2×10^{20} B/cm^3.) This also proves that the precipitation of boron atoms is not due to a dose that has exceeded the solid solubility, but is due to the clustering of boron interstitials.

The bounding dislocation line around the precipitate probably causes it to shrink only from the ends. There is no indication why and how these precipitates should behave like this; however, the stress field of the coherent precipitate may cause preferential drift of vacancies to the ends and the annihilation of a vacancy may be able to take place readily only at the ends. The redissolved boron atoms occupy substitutional lattice sites and result in the observed increase in conductivity.

The irregular and slower shrinking rate for type A linear defects such as 3 in Fig. 24, indicates that linear defects of this kind are composed mostly of silicon atoms which have a much smaller self-diffusion coefficient. They often transform into a perfect dislocation loop and rotate on the resulting glide cylinder to a ⟨112⟩ direction as is shown in Fig. 15. This behavior is consistent with the assumption that they are formed mostly by interstitial silicon.

Occasionally, it is also observed that a portion of a boron precipitate transforms into a perfect dislocation loop which also rotates to a ⟨112⟩ direction as is shown in Fig. 17. This may suggest that

some silicon atoms are incorporated in the boron precipitates as the boron diffuses away the remaining silicon tends to form a new perfect dislocation loop composed mostly of silicon atoms.

iv. The Climb of Dislocation Loops

a. Introduction. Silcox and Whelan[37] were the first to study the climb of dislocation loops in a thin film using transmission electron microscopy. Although this technique has proven to be useful for measuring self-diffusion coefficients and stacking fault energies in metals[38-41] and ionic crystals,[42,43] no one has applied the technique to silicon. Also, all previous observations of dislocation loop shrinkage or migration have been made on vacancy type loops.

In this section, both faulted circular or hexagonal dislocation loops with Burgers vector a/3⟨111⟩ and elongated perfect dislocation loops formed during post-implantation annealing in boron ion implanted silicon were studied in the temperature range between 940°C to 1000°C.

The mechanism of shrinkage of dislocation loops is discussed based on the experimental observations. The activation energy for shrinkage of these loops is determined.

b. On the mechanism of climb of dislocation loops

Diffusion vs emission controlled mechanism

Interstitial type dislocation loops, both faulted and perfect, were observed to shrink after the boron precipitates had been redissolved as observed previously.

There are two extreme cases for the shrinkage of dislocation loops. Silcox and Whelan[37] proposed that the rate of shrinkage was controlled by the emission of vacancies at jogs for the climb of prismatic

dislocation loops in quenched aluminum. On the other hand, Seidman and Balluffi[44] proposed that the rate controlling process should be the diffusion of point defects away from the dislocation loops. Theoretical considerations[45] indicate that the two mechanisms lead to essentially the same functional form of the rate equation and that the difference in rate is marginal and too small to allow any definite conclusion as to which process is rate controlling.

The general equation for the shrinkage of a circular dislocation loop of radius r in most metals (fcc structure) can be expressed as:[46] Based on the emission controlled process:

$$\frac{dr}{dt} = -\frac{3D}{b}\left[\exp\left(\frac{FcB^2}{kT}\right) - 1\right] \qquad (1)$$

where D is the coefficient of self-diffusion, b is the Burgers vector of the dislocation loop and B^2 is the cross-sectional area of an atom on the {111} plane. Fc is the driving force for climb and for a faulted loop is given by Bacon and Crocker.[47]

$$Fc = \frac{3Gb^2}{8\pi r}\left[\ln\left(\frac{2\pi r}{b}\right) - 0.37\right] + \gamma \qquad (4)$$

where G is the shear modulus and γ the stacking fault energy.

Based on the diffusion controlled process:

$$\frac{dr}{d\ell} = -\frac{2\pi D}{b \ln \frac{\ell}{b}}\left[\exp\left(\frac{FcB^2}{kT}\right) - 1\right] \qquad (3)$$

with $r > \ell$ (hald foil thickness), (assuming cylindrical diffusion geometry) and:

$$\frac{dr}{dt} = -\frac{2D}{b}\left[\exp\left(\frac{FcB^2}{kT}\right) - 1\right] \tag{4}$$

for $r < \ell$ (assuming spherical diffusion geometry).

Comparing Eqs. (1), (3) and (4), it is seen that the functional forms for the shrinkage rate of dislocation loops are the same. The only difference among them is the pre-exponential term. However, the shrinkage rate of Eq. (1) based on the emission controlled process is independent of the diffusion distance between the dislocation loop and sinks for point defects, whereas for the diffusion controlled process, this should not be the case. This difference provides a criterion for determining whether the process is emission or diffusion controlled experimentally. Hence, it is expected that if the process is diffusion controlled, then changes in the loop to sink distance should alter the climb rate for big loops. The shrinkage rate for large loops should depend on the depth of the loop in the foil.

The present experimental results show that the shrinkage rate of large dislocation loops in silicon is independent of the diffusion distance between the dislocation loops and sinks, both for external sinks such as a free surface or internal sinks as a dislocation line or a bigger loop. In Fig. 28, a Frank loop "F" , cut by the surface does not shrink faster than loops "D" or "E" of comparable size which are not touching the surface and, therefore, have longer diffusion lengths. It is also noted that two loops of different sizes close together such as at A all shrink independently, instead of the bigger one growing at the expense of the smaller one as would have expected on the basis of the diffusion controlled process. A similar behavior

is also observed in Fig. 29. Loops cut by the surface do not shrink faster than those of the same size inside the foil. These results strongly suggest that point defect concentration is essentially the same and close to the equilibrium value throughout the foil so that the shrinkage of dislocation loops is controlled by the emission or absorption of point defects rather than by their diffusion away from or to the defects.

Vacancy vs interstitial mechanism

Sanders and Dobson[48] observed that extinsic stacking faults grow into a silicon wafer during thermal oxidation and shrink on annealing in vacuo at the same temperature. They explained this behavior in terms of the diffusion of vacancies between defect and surface. The sense of this flow depends on the vacancy concentration in equilibrium with the surface. During thermal oxidation, the faults emit vacancies to the surface, causing fault growth, whereas the vacancy flow is reversed on annealing in vacuo.

This diffusion of vacancies can also be interpreted as the diffusion of interstitials in the opposite direction. In order to accommodate the inward growing oxide which is controlled by the transport of oxygen,[49] either vacancies should flow to the surface or excess interstitials produced by thermal oxidation should flow into the substrate. However, in order to explain experimentally observed abnormal impurity concentration profiles[50] which were not of the expected complementary error-diffusion type, Dobson[51,52] concluded that impurity diffusion in silicon occurred by the interstitialcy mechanism. Similarly prussin[53] attributed the growth of stacking faults and dislocation loops during wet oxidation to the

continuous generation of interstitials and distruction of vacancies at the silicon-oxide interface.

The existing data to date do not conclusively prove whether self-diffusion in silicon in the temperature range 950 to 1000°C is by a vacancy or an interstitial mechanism. Seeger[33] suggested from the existing data that in order to account for the unusually large pre-exponential factor for self-diffusion at high temperatures in silicon an interstitial mechanism is needed. He, therefore, concluded that above 900°C, an interstitial mechanism is more likely than a vacancy mechanism.

The temperature range in this study is between 940°C and 1000°C, therefore, a self-interstitial mechanism is assumed. More sophisticated annealing studies during wet oxidation might be capable of deciding the question.

c. <u>Models for shrinkage of circular and elongated dislocation</u> loops. Based on emission control and an interstitial mechanism, the interstitials must be emitted from the jogs on the dislocation loop as illustrated in Fig. 31. The jog velocity V_j depends on the climb force acting on the dislocation. Following Friedel:[54]

$$V_j = \frac{z\nu b}{\sin\alpha} \exp - \frac{U_f^i + U_m^i}{kT} \exp \frac{S_f^i + S_m^i}{kT} \left[\exp \frac{FcB^2}{2kT} - \frac{C_1}{C_o}\right] \qquad (5)$$

where z is the coordination number of an interstitial, ν is the atomic vibrational frequency, α is the angle between Burgers vector and dislocation line ($\sin\alpha = 1$ for an edge dislocation), b is the Burgers vector, U_f^i and U_m^i are the formation and migration energy for interstitials, S_f^i and S_m^i are the entropies of formation and migration for interstitials,

B^2 is the cross-sectional area of atoms on {111} planes, C_1 and C_o are the interstitial concentration around the dislocation loop under non-equilibrium and equilibrium condition respectively. Fc is the driving force for dislocation climb and can be expressed by Eq. (2).

At thermal equilibrium which would be the case during annealing, the average jog concentration can be expressed as:

$$C_j = \exp\left(\frac{S_j}{k}\right) \exp - \left(\frac{U_j}{kT}\right) \tag{6}$$

where S_j and U_j are the entropy and energy of formation of a jog on a dislocation line respectively.

The flux of point defects (interstitials) emitting away from the dislocation loop per unit length is, therefore, expressed as:

$$\phi = \frac{C_j V_j}{b^2} \tag{7}$$

Hence, the number of atoms change inside a circular loop of radius r is:

$$\frac{dn}{dt} = \frac{d\,\frac{2\times\pi r^2}{b^2}}{dt} = -2\pi r\times\phi \rightarrow \tag{8}$$

$$\frac{dr}{dt} = -\frac{1}{2} z\nu b \exp -\left(\frac{U_f^i + U_m^i + U_j}{kT}\right) \exp\left(\frac{S_f^i + S_m^i + S_j}{k}\right) \left[\exp\left(\frac{FcB^2}{2kT}\right) - \frac{C_1}{C_o}\right]$$

Similarly the shrinkage rate of an elongated dislocation loop of length L and width 2r which shrinks only in the length direction due to the smaller radius of curvature at the ends of the loop as shown in Fig. 23 can be expressed as:

$$\frac{dn}{dt} = \frac{d\,\frac{2\,L\,2r}{b^2}}{dt} = -\,2\pi r \times \phi \rightarrow$$

$$\frac{dL}{dt} = -\,\frac{\pi}{2}\,z\nu b \exp - \frac{U_f^i + U_m^i + U_j}{kt} \exp \frac{S_f^i + S_m^i + S_j}{} \left[\exp \frac{FcB^2}{2kT} - \frac{C_1}{C_o}\right] \qquad (9)$$

d. Results

General

Circular or hexagonal faulted dislocation loops, either parallel to the foil surfaces as loop "B" and "C": in Fig. 30, or on the inclined {111} planes as loop "A", all shrink steadily during annealing in the absence of oxidation. However, if surface oxidation occurs as shown in sequence 1 and 2 of Fig. 28-30 (due to forgetting to turn on the dry nitrogen flow) all loops bigger than the critical loop size "G" in Fig. 28 or "C" in Fig. 29 grew into hexagonal shape, while those smaller still shrank. This behavior is expected from Eq. (8), the line tension and stacking fault energy associated with the dislocation loop contained in Fc tend to make the dislocation loop shrink, while supersaturation of interstitials caused by oxidation as expressed by C_1/C_o tends to make the dislocation loop grow. At the critical loop size, these two driving forces cancel out.

It is also shown in Figs. 32 and 33 that elongated perfect dislocation loops along ⟨112⟩ directions such as "A" in Fig. 32 or in Fig. 33, show a tendency to break up into smaller loops during bulk annealing but during a thin film anneal, they either continue to shrink in the elongated

direction with the original shape or become more circular as they shrink.

The annealing rate of faulted dislocation loops

Shrinkage rates for a number of faulted dislocation loops at different annealing temperatures are shown in Fig. 34. The curves A, B and C are the annealing rates for loop A, B and C in Fig. 29 respectively. Curve D is the annealing rate for loop A in Fig. 30.

It is shown in this figure that the annealing rates for bigger loops are always slower than that for the smaller ones. The shrinkage rates accelerate as the loop sizes decrease.

This result is expected as predicted by Eq. (8). Under equilibrium annealing conditions, $C_1 = C_o$, the driving force for faulted dislocation loops to shrink would be the line tension and stacking fault energy. Figure 35 shows the variation of line tension with respect to the loop radius. Also illustrated are the stacking fault energy (55 ergs/cm^2)[55] and the corresponding thermal energy (kT) at different temperatures.

Since the line tension term is loop size dependent and has a smaller value for big loops as compared to the stacking fault energy, hence for big loops, the driving force for shrinkage is mainly due to the stacking fault. It is also noted that for smaller loops, such as B and C, the line tension plays an important role so that loop C shrinks faster than "B", yet the slower shrinkage rate at this temperature (942°C) makes them still fall on a straight line. However, if the shrinkage curves were corrected for the difference in the line tension[56] the results are as shown by the dotted lines in Fig. 34. It is then observed that all loops shrink at the same rate independent of loop size, due to the constant driving force of the stacking fault. The logarithmatic

shrinkage rates are plotted with respect to the reciprocal of the annealing temperatures in Fig. 36. The data gives an activation energy of 5.65±0.5 eV.

The annealing rate of perfect dislocation loops

Perfect dislocation loops such as those in Figs. 32 and 33 shrink steadily only in the length direction. This results in a constant driving force of line tension which depends on the radius of curvature at the ends of the loop. The dependence of driving force on the width of elongated loops is shown in Fig. 32, where loop C is narrower than loop B, therefore, has a larger driving force for shrinkage. Hence although loop B is longer than loop C, loop B shrinks faster than loop C.

Curve 1 in Fig. 37 shows the shrinkage rate of the loop in Fig. 33, curve 2 shows that of loop A in Fig. 32. It is noted that the shrinkage rates are constant at constant temperatures as expected in Eq. (9). The widths of these two loops are about the same, therefore, they show almost the same shrinkage rates at the same temperature because of the same driving force. If the logarithmic shrinkage rates are again plotted with respect to the reciprocal of the annealing temperatures (Fig. 36) an Arrhenius plot is again obtained which gives the same activation energy for shrinkage, 5.65±0.5 eV, as for faulted dislocation loops.

e. Discussion and conclusion. The remaining dislocation loops both faulted and perfect are observed to shrink after the linear boron precipitates have been redissolved. However, there exists a critical loop size above which the loop will grow instead of shrinking if any thermal oxidation is taking place as was also observed by Sanders and Dobson[48] and Prussin.[53] From a preliminary calculation, it is concluded that oxidation at 942°C causes a supersaturation of interstitials up

to 1.4 times that in equilibrium in the absence of oxidation.

The experimentally observed fact that loops of similar sizes shrink at the same rate independent of the positions of the loops in the foil strongly suggests that the loop shrinkage is controlled by the emission of point defects instead of by diffusion.

Equations (8) and (9) express the shrinkage rate of a faulted circular loop and an elongated perfect dislocation loop respectively. The activation energy for shrinkage obtained experimentally is 5.65±0.5 eV in both cases as would have been expected from Eqs. (8) or (9). If the activation energy for self-diffusion $U_j^i + U_m^i$, is assumed to be 5.13 eV as reported from radio-tracer analysis by Fairfield and Masters,[57] a jog formation energy U_j of about 0.5 eV is obtained from Eq. (8) or (9). Putting all known values into either Eq. (8) or (9) and using the shrinkage rate as observed experimentally, the total entropies were calculated to be 17.9 k. If we assume that the entropy for self-diffusion is 15 k,[33] the entropy for jog formation in silicon is then roughly 2.9 k. Therefore, as pointed out by Seeger[33] the enormously large entropy or pre-exponential factor for self-diffusion, makes the vacancy mechanism as observed in most metals seems imparable for silicon.

Because the activation energy for loop shrinkage corresponds to that for silicon self-diffusion, it is concluded that both faulted Frank loops and perfect loops are composed mostly of silicon atoms.

D. On the Depth Distribution of Crystal Defects in Boron Ion Implanted Si

i. Introduction

The depth distribution of defects in crystals is important in many cases such as when studying surface effects or the factors that control defect nucleation and growth. It is particularly important for studying the defect distribution in radiation damaged crystals such as after ion implantation in silicon.

The depth distribution for the primary defects is very difficult to determine experimentally with known technology. However, theoretical considerations[58] based on interactions between incoming particles and the substrate lattice atoms have made it possible to determine the depth distribution of the incident ions theoretically. It is expected that the depth distribution of the incident ions in an amorphous material (or crystalline material in the absence of channeling effects) is roughly Gaussian in shape.

Akasaka et al.[59] have determined the depth distribution of boron atoms and radiation induced defects in boron ion implanted silicon by utilizing the $^{11}B(P,\alpha)^{8}Be$ nuclear reaction and by channeling analysis with 1.5 MeV He^{+} ions, combined with anodic oxidation and stripping for removal of a known thickness. They observed that the distribution of boron atoms and the primary defects are asymmetric and significantly deviated from the Gaussian distribution. They also observed that the secondary defects have a Gaussian distribution, the peak depth of which almost coincides with that of the boron distribution.

It is the purpose of the following experiment to study the depth distribution of the secondary defects after post-implantation annealing

utilizing transmission electron microscopy, so that direct correlation between the crystal defects and electrical properties, and a better understanding of the mechanism of formation of these defects, especially the linear boron precipitates, can be achieved.

ii. Experimental

Latex balls of diameter 1090±30Å were diluted in distilled H_2O (1 drop concentrated + 5 cc H_2O) before being applied to the thin foil surfaces.

The thin foil was then put into a Philips 301 transmission electron microscope equipped with a high angle tilting stage that could be tilted up to 60°. Pictures were taken with more than two beams operating, so that all defects could be in contrast simultaneously. All pictures were taken either near ⟨111⟩ or ⟨112⟩ orientations. The tilting axis, tilting angle and tilting direction were correctly determined from the Kikuchi pattern as described previously.[23]

iii. Results

In order to determine the depth of defects inside the thin foil, some reference points on the foil surfaces are required. Uniformly sized latex balls were first suggested as reference points by Sadhukhan,[60] later also by von Heimendahl,[61] for determination of foil thickness. Geometrical considerations enable us to distinguish between latex balls on one side of the foil from those on the other, if the tilting axis and the tilting direction are known. This technique provides an accurate method for foil thickness determination.

A further utilization of latex balls is the determination of the depth distribution of crystal defects.

A typical example is shown in Fig. 38. The first picture was taken near ⟨111⟩ (see the included diffraction pattern) orientation, the second was taken near ⟨112⟩ orientation. The double images, due to more than one diffracting vector operating, are clearly shown for defect "F". It is also noted that defect "D" and "E" are parallel to each other near ⟨111⟩ orientation, however, defect "D" lies parallel to defect "C" which is along the ⟨110⟩ tilting axis when tilted to ⟨112⟩ orientation, while defect "E" is still inclined to defect "C". This further proves that linear defects lie along all six possible ⟨110⟩ directions and that there exist some perfect dislocation loops with elongated directions along ⟨112⟩ such as "C".

From the measured projected distance change between latex balls "A" and "B", it is concluded that both balls are on the same top surface of the foil. Then from the Eq. (9) in the Appendices, the defect distribution can be determined accurately.

Figure 39 shows the depth distribution of boron precipitates that are parallel to the foil surfaces in the unit of length per volume. Also shown in this figure are the positions of the ends of those precipitates that are inclined to the foil as marked by 1, 2, 3 etc.

Figure 40 shows the depth distribution of the dislocation loops in the unit of area per unit volume.

iv. Discussions and Conclusions

The depth distribution of linear boron precipitates, is very shallow and not symmetric. If an imaginary Gaussian distribution curve is applied to these data as shown by the dotted line in Fig. 39, it is noted that the peak depth is about 3500Å from the implanted side which is exactly as reported by Akasaka et al.[50] for the distribution of boron atoms as determined by an entirely different method. This also suggests that these linear defects are closely related to boron atoms (precipitates). The asymmetric nature of the distribution of boron precipitates is probably due to the surface effect as reported previously. As pointed out in Section iii, the growth of these linear boron precipitates is explained as the diffusion of supersaturated boron atoms to the precipitation sites. For boron atoms above the peak depth, they can very easily become substitutional again not only because they are closer to the free surface but also because a lot of vacancies produced during ion implantation are available. However, the supersaturated boron atoms distributed deeper than the peak depth have more difficulty finding a vacancy during bulk annealing, so that they tend to precipitate out forming linear boron precipitates. This surface efects on the formation of linear boron precipitates is most clearly shown in Fig. 41, where Fig. 41a shows the morphology of a sample thinned down before successively annealing to the temperatures indicated. Figure 41c shows the effect of first bulk annealing to 700°C before thinning down and then reannealing to the temperatures indicated. Figure 41e shows the result of bulk annealing to the temperatures indicated before thinning down. If the specimen was subjected to two free surfaces during annealing, most of

the supersaturated boron atoms tended to become substitutional again, so that only very few narrow faint boron precipitates were observed. However, if the specimen was bulk annealed to the temperature where boron atoms are mobile, the supersaturated boron atoms distributed deeper than the peak region tended to precipitate out to form the linear defects along ⟨110⟩ directions.

It is also noted that most linear boron precipitates inclined to the foil surfaces were nucleated around the peak region and then grew mostly toward the implanted free surface, but some also grew inward as marked by 2 or 3 in Fig. 39.

The depth distribution for small dislocation loops also shows a peak depth at about 3500Å from the implanted side, but it was a much wider spread as compared to the boron precipitates. This result is also in good agreement with the secondary defect distribution as reported by Akasaka[59] with peak depth of 0.34±0.2μ and peak width 0.18μ.

E. Direct Observation of Radiation Induced Precipitation in the High Voltage Electron Microscope

i. Introduction

The advantages of high voltage electron microscopy (HVEM) (operating at 300 kV or more) lie not only in its larger penetration power, capable of examining specimens a few microns thick[62] as compared to 0.05μ to 0.5μ for the normal 100 kV instrument (so that the structures observed in the HVEM are more representative of that in the bulk material), but also in its simple mode of producing radiation damage without the introduction of impurities and without collision cascades.[63,64] HVEM has been proven to be a powerful instrument for studying radiation damage in situ.

Nes and Washburn[31] first observed radiation induced precipitation in high purity Lopex (low-oxygen dislocation-free silicon) which had been contaminated with copper. They observed two kinds of radiation induced precipitation, 1) at room temperature, a whisker-like precipitate structure which developed along the dislocation lines, 2) during hot stage observations, long needle-shaped precipitates oriented along ⟨110⟩ directions were formed. They did not identify these precipitates.

However, the linear rod-like defects observed in boron ion implanted silicon which have been proved to be boron precipitates in the previous section, take the same shape as the long needle-shaped precipitates. Similar defects are also observed in Ne ion implanted silicon.[30] It is, therefore, of interest to study the effects of boron atoms and irradiation temperature on the formation of these linear defects by direct observation in HVEM equipped with a hot stage, so that the mechanisms that cause the formation of these linear defects can be better understood.

ii. Experimental

P-type, boron doped, ⟨111⟩ oriented silicon wafers of resistivity 0.75 Ω-cm ($\sim 2.5\times10^{16}$ B/cm^3), and n-type, phosphorous doped, ⟨111⟩ oriented silicon wafers of resistivity 2 Ω-cm (2.7×10^{15} P/cm^3) were used in this experiment.

They were cut into discs and then thinned down from one side as described previously.[23] The thinned foil was then put into a Mo-tipped hot stage specimen holder of the Berkeley Hitachi HVEM operating at 650 kV. The temperature of the hot stage was pre-calibrated to an accuracy of ±10°C.

iii. Results

Figure 42 is an example of the formation and development of linear defects in p-type silicon irradiated with 650 keV electrons at 620°C. It is noted that these linear defects develop very rapidly in the three ⟨110⟩ directions parallel to the foil surface and become saturated in about 20 min. This latter fact strongly suggests that the formation of these defects is limited by the boron content which, therefore, implies that they are some sort of boron precipitate. It is also noted that there are a lot irregularly shaped dislocation loops similar to those in boron ion implanted silicon. Figure 43 shows a comparison between the morphology in boron ion implanted silicon after annealing at 800°C and high voltage electron irradiated boron doped silicon.

The formation of linear defects (boron precipitates) is very temperature sensitive as is shown in Fig. 44, where Fig. 44a, shows the morphology during 720°C irradiation as compared to Fig. 44b during 620°C irradiation. The defects formed during 720°C irradiation show a characteristic similar to that of stacking faults on the inclined {111} planes. There has been no effort to identify the nature of these defects.

No defects of any kind were observed in the phosphorous doped silicon irradiated at the same temperatures as boron doped up to 1 hr irradiation.

iv. Discussion and Conclusion

The formation of linear defects, in high voltage electron irradiated boron doped silicon implies that:

1) The mechanism for formation of these linear defects is probably coprecipitation of silicon and boron interstitials. Some of the interstitial boron is probably produced by replacement reaction with interstitial silicon.

2) If the irradiation temperature is too high, the critical supersaturation of boron and silicon interstitials necessary for nucleation and growth of rod shaped precipitates is probably not achieved. Most of the point defects reach the surfaces of the thin foil. Irradiation at 720°C resulted in formation of a few defects that appeared to be Frank loops.

As was pointed out by Makin,[65] the electron energy E required so that an energy Em can be given to an atom of mass M_2 during a Rutherford collision is given by

$$E_m = \frac{2E(E + 2mc^2)}{M_2C^2} \qquad (1)$$

where m is the electron rest mass and c the velocity of light. The values of E for a range of Em in the vicinity of the displacement energy Ed are given in Table III for Si and B.

It is clear that the operating voltage, 650 kV, is high enough to produce lattice displacements for both B and Si in this case. Since the ratio of boron atoms to silicon atoms is very small, (10^{-6}), nearly all the direct interstitials are silicons.

The collision cross section for lattice displacements as given by Dugdale and Green[66] is:

Table III. Electron energy E required to transfer Em to a Si or B atom.

Em (eV)	20	25	30
E (keV) (Si)	217	270	315
E (keV) (B)	91	111	131

$$\sigma_d = \frac{4Z_2^2E_R^2}{m^2c^4}\left(\frac{Em}{Ed}\right)\pi A_o^2\left(\frac{1-\beta^2}{\beta^4}\right)\left\{1 + 2\pi\alpha\beta\left(\frac{Ed}{Em}\right)^{1/2} - \left(\frac{Ed}{Em}\right)\left[1 + 2\pi\alpha\beta + (\beta^2 + \pi\alpha\beta)\ln\frac{Em}{Ed}\right]\right\} \qquad (2)$$

where Z_2 is the atomic number of the target atoms, E_R is the Rydberg energy (13.6 eV), πA_o^2 is 8.8×10^{-17} cm^2, α is $Z_2/137$ and β is ν/c, where ν is electron velocity. If all the known values are put into Eq. (2) σ_d for silicon is about 10 barns (10^{-24} cm^2).

The displacement rate "K" can be estimated as:

$$K = \text{No. of displacement/cm}^3\text{, sec} = \sigma_d No \phi_e P \qquad (3)$$

where No is the atomic density for silicon, ϕ_e is the flux of electrons, $P = 1 + \ln\frac{Em}{2E_d}$, for $E_m > 2E_d$.

The value for ϕ_e is about 10^{19} $e^-/cm^{-2}sec^{-1}$ (0.4 μA in a 5μ spot) which is much higher (>1000×) than in a conventional electron accelerator.

Therefore, the displacement rate of silicon atoms during high voltage electron microscope observation is approximately $\sim5\times10^{18}$ Frankel pairs cm^{-3}, sec^{-1}.

This very high production rate of silicon interstitials explains why only a few minutes are required to reach the critical supersaturation of silicon and boron interstitials, most of the boron interstitials probably resulting from replacement of a substitutional boron atom by a silicon interstitial.

IV. DISCUSSION

The crystal defects formed after post-implantation annealing in boron ion implanted silicon have been investigated and identified as described in the previous chapter.

The very long type $\bar{A}$ linear defects which appear in boron ion implanted silicon have been shown to be boron precipitates which are best described as having a {100} habit plane a a/x⟨100⟩ burgers vector and a ⟨110⟩ long axis. Since this type of defect is also observed in boron-doped silicon when it is irradiated at 620°C in the beam of the high voltage electron microscope but is not observed in phosphorous doped silicon under similar conditions, this again suggests that these defects cannot be entirely silicon defects. Interstitial boron atoms must play a critical role in their nucleation or growth. The temperature dependence of the shrinkage rate of these defects during annealing suggests that a large fraction of the atoms making up the rod defects are boron atoms. The probable mechanism of nucleation and growth of these linear defects during high voltage electron irradiation at 620°C is represented schematically in Fig. 45. The high energy electrons first produce Frankel pairs at 1, the silicon interstitials then move about and substitute a boron atom at 2. The substituted boron atoms, therefore, cause local supersaturation of boron interstitials and nucleate a precipitate or migrate interstitially to existing precipitates and cause them to grow.

From the experimental results described in the previous chapter, it is concluded that during boron ion implantion at room temperature, the silicon and many of the boron interstitials form small clusters that are metastable at room temperature.

As the annealing temperature is raised to the range 600°C, to 750°C. Some of these clusters gradually break up releasing mobile silicon interstitials. The silicon interstitials replace substitutional boron atoms, so that a reverse annealing stage is observed in sheet resistivity Fig. 3. Most of the silicon and boron atoms in the clusters are released at about 750°C where growth of rod shaped defects is observed. The results also suggest that boron diffusion in silicon must be by an interstitial mechanism as pointed out by Dobson.[51,52] Otherwise the replaced interstitial borons would not diffuse to form precipitates but rather would become substitutional again after a single diffusion jump.

The reverse annealing observed after boron ion implantation to moderate doses is, therefore, closely related to the replacement of substitutional boron by interstitial silicon.

Besides these type $\bar{A}$ linear defects, there also exists a type A linear defect which can best be described as narrow spaced Frank dislocation loops with a ⟨110⟩ long axis. Unlike type $\bar{A}$ defects which maintain their width during their shrinkage at moderate temperature (~800°C), type A linear defects usually shrink more slowly and become fatter up to about 1000°C. Occasionally they also shrink irregularly fast from one end of the loop (Fig. 13 and Fig. 24) or change into a perfect dislocation loop with a ⟨112⟩ long axis (Fig. 15 and Fig. 15A). From the shrinkage rate of either the small Frank dislocation loops which originated from the breaking up of an elongated type A defect during bulk annealing or from the shrinkage rate of perfect elongated dislocation loops with ⟨112⟩ long axis it is concluded that type A defects are composed mostly of silicon atoms. The occasionally observed

irregularly fast shrinkage from one end of type A defects suggests that some segments of these loops may be impurity rich. The gradual increase in the loop width compared to its length may be attributed to the decrease of dislocation strain energy.

The sudden change of a type A defect into a perfect elongated loop which rotates to ⟨112⟩, usually happens during the first time the thin foil is annealed. This suggests that the image force acting on a dislocation loop near the surface may help in nucleating a Shockley partial which can sweep away the enclosed stacking fault.

The reason for coexistence of two different types of rod-like defects, e.g., A and $\bar{A}$, on different planes is not understood. However, one kind composed mostly of boron atoms (type $\bar{A}$) and the other composed largely of silicon atoms (type A) suggest that during their nucleation and growth, silicon interstitials are probably more easily precipitated on {111} planes while boron interstitials on {100} plane. There might be some interruption on the regular precipitation of Si and B interstitials on {111} and {100} planes, respectively. So that some segment of type $\bar{A}$ defects might be composed largely of silicon atoms instead of borons as possibly suggested by the different contrast of segment x of defect A in Fig. 46. This possible silicon rich segment may also account for the occasional observation of nucleation and growth of a perfect dislocation loop with long axis along ⟨112⟩ adjacent to a type $\bar{A}$ defect. Similarly, the precipitation of silicon interstitials on {111} plane may also be interrupted by borons or other impurities (like oxygen) which can cause the irregular shrinkage of type A defects from one end.

The contrast for small loops as well as narrow spaced dipoles is complicated particularly when observations are made in weak beam dark field conditions by several factors; e.g., s value, foil thickness, width and depth of defects.[67,68] As shown in Fig. 46, defects of the same kind (parallel to the same direction) varies in contrast (visibility) under the same conditions (same picture). (Obviously due to depth or width or b vector of the defect.) They also vary in visibility when the s value is changed, as shown by the disappearance of defect K, D or X in Fig. 46; $s = 6\times10^{-3}$, 4.7×10^{-3} and 7.56×10^{-3} Å from left to right. This makes Burgers vector determination very diffisult under weak beam dark field (s>>o) on higher order reflection bright field condition as was pointed out by Chen and Thomas.

In order to avoid this complication in contrast under W.B.D.F or higher order bright field conditions, the diffracting condition was carefully chosen for the Burgers vector determination in this experiment. All pictures for contrast analysis were taken under B.F. conditions with only the first order reflection excited with s slightly larger than zero. This diffracting condition usually gives reasonable visibility which is insensitive to the foil thickness and depth of defects.[18] The W.B.D.F technique though useful in determining the shape of small defects is not appropriate in determining dislocation Burgers vectors as was also pointed out by Chen and Thomas.[67]

The weak contrast of type $\bar{A}$ defects, e.g., a and d in Fig. 12(a-k), is, therefore, thought to be due to residual contrast of the dislocation lines instead of being due to any of the above factors.

From the contrast analysis, it is concluded that there exist at least two different types of linear defects, e.g., A and $\bar{A}$, both interstitial in nature. It is also concluded that most of the small hexagonal or circular dislocation loops are interstitial Frank sessile loops lying on all four {111}.

ACKNOWLEDGEMENTS

I want to express my deep gratitude to Professor Jack Washburn for his guidance and encouragement throughout this research. The continued interest of Professor Gareth Thomas in this work is also appreciated. I also want to express my gratitude to the supporting staff of IMRD. Special thanks are due to Shirley Ashley, Jean Wolslegel, Douglas Kreitz, Gloria Pelatowski and Phila Wetherell for preparing the manuscript and photographs.

I am also in great debt to my parents, Mr. and Mrs. Fong-Shiang and Tsai-Chich Lee Wu, who directed me to pursue the truth of nature during my early years of study. I also want to express my gratitude to my parents in law, Mr. and Mrs. Thomas Meng-Cheng and Kwei-Jen Wang Chang, for their encouragement.

Most of all, I want to thank my wife, Mrs. Dolly Chung-Yen Chang Wu, for her pleasant companionship and encouragement that maked my study and research work more successful. Without her tender care of my life and constant encouragement in my work, I would not have been able to finish this work in less than two years.

I am also indebted to many of my friends in both the Materials Science and Electrical Engineering Departments, who have created a very pleasant atmosphere in research and have given me a very good opportunity to learn.

This work was done under the auspices of the U. S. Energy Research and Development Administration.

REFERENCES

1. G. Dearnaley, J. H. Freeman, G. A. Gard and M. A. Wilkins, Can. J. Phys. 46, 587 (1968).
2. R. Baron, G. A. Shifrin and O. J. Marsh, J. Appl. Phys. 40, 3702 (1969).
3. B. L. Crowder and R. S. Title, Rad. Effects 6, 63 (1970).
4. J. A. Davies, G. C. Ball, F. Brown and B. Domeij, Can. J. Phys. 42, 1070 (1964).
5. S. M. Davidson, II International Conference on Ion Implantation in Semiconductors (Springer-Verlag, Berlin, 1971) p. 79.
6. D. E. Davies, Appl. Phys. Letters 14, 227 (1969).
7. N. G. Johansson and J. W. Mayer, Solid State Electron 13, 123 (1970).
8. R. W. Bicknell, Phil. Mag. 26, 273 (1972).
9. J. A. Davies, J. Denhartog, L. Eriksson and J. W. Mayer, Can. J. Phys. 45, 4053 (1967).
10. G. Fladda, P. Mazzoldi, E. Rimini, D. Sigurd and L. Eriksson, Rad. Effects 1, 249 (1969).
11. G. Fladda, K. Björkquist, L. Eriksson and D. Sigurd, Appl. Phys. Letters 16, 313 (1970).
12. L. Eriksson, J. A. Davies, N. G. E. Johansson and J. W. Mayer, J. Appl. Phys. 40, 842 (1969).
13. K. Björkquist, B. Domeij, L. Eriksson, G. Fladda, A. Fontell and J. W. Mayer, Appl. Phys. Letters 13, 379 (1968).
14. R. W. Bicknell and R. M. Allen, Rad. Effects 6, 45 (1970).
15. L. T. Chadderton and F. H. Eisen, Rad. Effects 7, 129 (1971).
16. P. K. Madden and S. M. Davidson, Rad. Effects 14, 271 (1972).

17. S. M. Davidson and G. R. Booker, Rad. Effects 6, 33 (1970).

18. P. B. Hirsch, A. Howie, R. B. Nicholson and D. W. Pashley, Electron Microscopy of Thin Crystals (Butterworths, London, 1965).

19. D. J. H. Cockayne, Z. Natur. Forsch. 27a, 452 (1972).

20. W. Wu and J. Washburn, J. Appl. Phys. 45, 1085 (1974).

21. W. Worthington, R. Sinclair and G. Thomas, LBL-2587, March 1974.

22. L. J. van der Pauw, Philips Tech. Review 20, 220 (1958-59).

23. W. Wu, L. J. Chen, J. Washburn and G. Thomas, J. Appl. Phys. 45, 563 (1974).

24. K. Seshen and J. Washburn, Phys. Stat. Solidi 26, 345 (1974).

25. D. Hull, Introduction to Dislocations (Pergamon Press, London, 1965), p. 95.

26. G. R. Booker and W. J. Tunstall, Phil. Mag. 13, 71 (1966).

27. W. J. Tunstall, Phil. Mag. 20, 701 (1969).

28. A. Howie and M. J. Whelan, Proc. R. Soc. A267, 206 (1962).

29. J. W. Silcock and W. J. Tunstall, Phil. Mag. 10, 361 (1964).

30. D. J. Mazey, R. S. Barnes and R. S. Nelson, Proc. 6th International Conference on Electron Microscopy (Kyoto, 1966), p. 363.

31. E. Nes and J. Washburn, J. Appl. Phys. 42, 3559 (1971).

32. J. Friedel, Dislocations (Pergamon Press, Oxford, 1964), p. 127.

33. A. Seeger, Rad. Effects 9, 15 (1971).

34. E. Nes and J. Washburn, J. Appl. Phys. 44, 3682 (1973).

35. H. F. Wolf, Silicon Semiconductor Data (Pergamon Press, London, 1969) p. 138.

36. G. D. Watkins and J. W. Corbett, Phys. Rev. 138A, 543 (1965).

37. J. Silcox and M. J. Whelan, Phil. Mag. 5, 1 (1960).

38. J. W. Edington and R. E. Smallman, Phil. May. 11, 1109 (1965).

39. J. P. Tartour and J. Washburn, Phil. Mag. 18, 1257 (1968).

40. J. Washburn and M. J. Yokota, Cryst. Lattice Defects 1, 23 (1969).

41. V. C. Kannan and G. Thomas, J. Appl. Phys. 37, 2363 (1966).

42. J. Narayan and J. Washburn, Phil. Mag. 26, 1179 (1972).

43. J. Narayan and J. Washburn, Cryst. Lattice Defects 3, 91 (1972).

44. D. N. Seidman and R. W. Balluffi, Phil. Mag. 13, 649 (1966).

45. M. J. Whelan, Phil. Mag. 14, 195 (1966).

46. P. S. Dobson, P. J. Goodhew and R. E. Smallman, Phil. Mag. 16, 9 (1967).

47. D. J. Bacon and A. G. Crocker, Phil. Mag. 12, 195 (1966).

48. I. R. Sanders and P. S. Dobson, Phil. Mag. 20, 881 (1969).

49. M. M. Atalla, Properties of Elemental and Compound Semiconductors, edited by H. Gatos (Interscience Publishers Inc., New York, 1960) Vol. 5, p. 163.

50. R. N. Ghoshtagore, Phys. Rev. Letters 25, 856 (1970); Phys. Rev. B. 3, 389 (1971a), ibid. 3, 397 (1971b).

51. P. S. Dobson, Phil. Mag. 24, 567 (1971).

52. P. S. Dobson, Phil. Mag. 26, 1301 (1972).

53. S. Prussia, J. Appl. Phys. 45, 1635 (1974).

54. J. Friedel, Dislocations (Pergamon Press, Oxford, 1974).

55. I. L. F. Ray and D. J. H. Cockayne, Phil. Mag. 22, 853 (1970).

56. P. S. Dobson and R. E. Smallman, Phil. Mag. 14, 357 (1966).

57. J. M. Fairfield and B. J. Masters, J. Appl. Phys. 38, 3148 (1967).

58. J. Lindhard and M. Sharff, Phys. Rev. 124, 128 (1961).

59. Y. Akasaka, K. HOrie, K. Yoneda, S. Kawabe and A. Tohi, J. Appl. Phys. 44, 220 (1973).

60. P. Sadhukhan, Philips Bulletin, No. EM 54 (1970).

61. M. von Heimendahl, Micron 4, 111 (1973).

62. G. Thomas and J. C. Locaze, J. of Microscopy 97, 301 (1973).

63. J. T. Buswell, S. B. Fisher, J. E. Harbottle, D. I. R. Norris and K. R. Williams, Proceedings of the 1971 International Conference on Radiation--Induced Voids in Metals (1972), p. 533.

64. F. A. Garner and L. E. Thomas, Effects of Radiation on Substructure and Mechanical Properties of Metals and Alloys, ASTM STP 529 (1973) p. 305.

65. M. J. Makin, Phil. Mag. 18, 637 (1968).

66. R. A. Dugdal and A. Green, Phil. Mag. 45, 163 (1954).

67. L. J. Chen and G. Thomas, Phys. Stat. Sol.(a) 25, 193 (1974).

68. J. Washburn and Th. Cass, Journal de Physique 27, 63 (1966).

FIGURE CAPTIONS

Fig. 1. Electrons and holes associated with boron impurities in silicon.

Fig. 2. Electrical carrier profiles for 40 kV B^+ in silicon irradiated at room temperature (courtesy of S. M. Davidson[5]).

Fig. 3. Sheet resistivity annealing curve for Si.

Fig. 4. Concentration of boron atoms on substitutional sites as a junction of annealing temperatures (courtesy of Appl. Phys. Lett.[11]).

Fig. 5. The electrical configuration for sheet resistivity measurement.

Fig. 6. Typical crystal rejects formed after post-implantation annealing in boron ion implanted silicon.

Fig. 7. The existence of two kinds of linear defects, A and $\bar{A}$, parallel to the same direction, but showing different contrast.

Fig. 8. 8i. The W.B.D.F. contrasts of defects as observed at different orientations. The loop planes of these small dislocation loops are determined from the trace analysis and tilting experiments. Figure A and B are near $[\bar{1}\bar{1}\bar{1}]$ orientation. Figure C and D are near $[\bar{2}\bar{1}\bar{1}]$ orientation. Figure E and F are near $[\bar{1}\bar{1}\bar{2}]$ orientation.

Fig. 9. Showing the starting fault fringe contrast of small dislocation loops. It is noted that the fringes are parallel to the bounding partials for loops inside the foil, e.g., E. Loop A and B are on the inclined {111} planes and loop D is on the foil plane.

Fig. 10. Showing the coexistence of a pure edge perfect dislocation loop A on {111} plane and small faulted dislocation loops B and C on the inclined {111} planes. Loop A has been annealed out of the foil at 942°C for 1 hr as shown in Fig. 2.

Fig. 11. Illustration of the effect of inclinations of the same kind of defects on the observed contrast. Figure (b) shows the top view of Fig. (a). Figure (c) shows the observed contrast of Fig. (a).

Fig. 12. Showing the contrast of linear defects in different orientations Fig. a-e are near [001] orientation. Figure f and g are near [101] and Fig. h and i are near 011 orientation. The spotly background reveals the oxide sites etched in deoxide solution after the thin foil was made.

Fig. 13. Isochronal annealing sequence of linear defects A and $\bar{A}$ in boron ion implanted silicon thin foil. Figure is bulk annealed at 800°C in 20 min before thinning. Figure b-e are thin foil annealed at 850°C, 900°C, 952°C and 1017°C for 20 min successively. It is noted that the closely spaced type A linear defect shrinks continuously and becomes wider showing contrast similar to that of the Frank dislocation loop.

Fig. 14. Similar sequence as in Fig. 13.

Fig. 15. Similar annealing sequence as in Fig. 13. It is noted that type A linear defect may suddenly change into an elongated perfect dislocation loop along ⟨112⟩ direction. The dotted line is the position where linear defect A was.

Fig. 15A. Another example of the transformation of type A defect into a perfect dislocation loop along ⟨112⟩. Also shown is an inclined defect "a" that has transformed into a small loop as shown in Fig. b. Figure a is bulk annealed at 800°C for 30 min and Fig. B is thin foil annealed at 800°C for 25 min.

Fig. 16. Similar annealing sequence as Fig. 13. This sequence shows the evolution of a perfect dislocation loop "B" formed adjacent to a type $\bar{A}$ linear defect. Ti is noted that loop B will grow when defect $\bar{A}$ shrinks and then loop "B" shrinks too.

Fig. 17. The annealing sequence of type $\bar{A}$ linear defects. Figure a is bulk annealed at 800°C for 30 min. Figure b-d are thin foil annealed at 802°C for 25 min successively. Figure 3 is annealed at 802°C for 50 min additionally. Figure f is annealed at 750°C for 70 min. It is noted that defect "B" suddenly bends from one end and forms a perfect dislocation loop C which tends to lie along ⟨112⟩ direction. The original defect B is out of contrast when the $\bar{g}$ vector is along its axis as shown in Fig. 2 and loop "C" shows weak residual contrast when the $\bar{g}$ vector is $[\bar{1}\bar{1}1]$ as shown in Fig. h. This indicates that the Burgers vector for loop "C" is a/2⟨110⟩ perpendicular to the elongated loop direction and different than that of the original linear defect.

Fig. 18. Showing the evolution of irregularly shaped dislocation loops A and B. Figure a-d as thin foil annealed at 850°C, 900°C, 952°C and 1017°C for 20 min respectively. It is noted that perfect dislocation loop A and B tend to lie along ⟨112⟩ directions.

Fig. 19. Showing the shrinks of small Frank dislocation loops along ⟨110⟩ directions. It is thought that they are originated by breaking up big elongated dislocation loops.

Fig. 20. Showing the evolution of small dislocation loops. The heat treatment is the same as Fig. 13. It is noted that small dislocation loops such as loop 3 and 4 just grow in size when the linear defects are shrinking and then shrink too.

Fig. 21. Showing the sequence of interaction between a faulted dislocation loop "A" and a perfect dislocation loop "B". The starting fault of loop A was swept away during this interaction as shown by the disappearance of dark center for loop A. The heat treatment is the same as Fig. 18.

Fig. 22. Sequential illustration of interaction of dislocation loops A and B in Fig. 21.

Fig. 23. Schematic illustration of elongated defect of length L and width 2R sit at the center of foil of thickness 2ℓ.

Fig. 24. Showing the annealing sequence of type $\bar{A}$ linear defects. The heat treatment is the same as in Fig. 17. It is noted that a new perfect dislocation loop a is nucleated and continue to grow when defect 1 is shrinking. Also noted is the slower irregular shrinkage rate for defect 3 which shows different contrast than others.

Fig. 25. The shrinkage rate for linear defects at different annealing temperatures. The solid lines represent the shrinkage curve for type $\bar{A}$ linear defects. The dotted lines are for type A. The parabolic-like solid line shows the effect of diffusion length on the shrinkage rate.

Fig. 26. The plot of logarithmic shrinkage rate with respect to the reciprocal of absolute annealing temperature.

Fig. 28. The annealing sequence of faulted Frank dislocation loops. Figure 1 is bulk annealed isochronally from 400°C to 1050°C for 20 min in 50°C intervals before thinning. Figure 2-4 are thin foil annealed at 942°C for 1 hr successively. Figure 5-7 are then annealed at 970°C for 15 min and 30 min respectively. Figure 8 and 9 are annealed at 1001°C for 10 and 20 min. It is noted two loops at A coalesced into one. Loop F is cut by the surface.

Fig. 29. Similar annealing sequence of small dislocation loops as in Fig. 28.

Fig. 30. Similar annealing sequence of dislocation loops as Fig. 28. Loop B and C are parallel to the foil plane and loop A is inclined to it.

Fig. 31. The schematic illustration of jogs on the preiphery of a dislocation loop of radius r. The emission of atoms at jogs is also illustrated in terms of jog volicity ν_j.

Fig. 32. The annealing sequence for perfect dislocation loop A, B and C. The heat treatment is similar to Fig. 28.

Fig. 33. Similar annealing sequence for perfect dislocation loop as in Fig. 32.

Fig. 34. The shrinkage rates for faulted dislocation loops at different annealing temperatures. The open insides indicate the measured data. The closed circles indicate that after line tension correction. The accelerating shrinkage rate for smaller loops is noted.

Fig. 35. The dislocation energy due to line tension as a junction of loop radius. r_o is the dislocation core radius. Also known are the starting fault energy and thermal energies (kT) at different temperatures.

Fig. 36. The plot of logarithmic shrinkage rates and the reciprocal of annealing temperatures for both perfect and faulted dislocation loops.

Fig. 37. The shrinkage rates for perfect dislocation loops at different annealing temperatures.

Fig. 38. Stereo pairs of the defects in boron ion implanted silicon. Figure 1 is taken near ⟨111⟩ orientation and Fig. 2 is near ⟨112⟩. The tilting axis and tilting direction are shown as indicated. Latex balls A and B are used as reference points on the foil surface, so that the depth distribution of defects can be determined.

Fig. 39. The depth distribution for boron precipitates parallel to the foil surface in a bulk annealed silicon at 800°C for 30 min. The number shows the positions of boron precipitates inclined to the foil surfaces.

Fig. 40. The depth distribution of dislocation loops in the same foil as in Fig. 39.

Fig. 41. Showing the effect of free surfaces on the formation of defects. Figure a and b are thinned before annealing from 400°C up to the temperatures indicated. Figure c and d are bulk annealed to 700°C before thinning and followed by the annealing as indicated for 20 min. Figure e and f are bulk annealed at 800°C and then thin foil annealed at 850°C for 20 min respectively.

Fig. 42. The sequence of nucleation and growth of linear boron precipitates in high voltage electron (650 keV) irradiated boron doped silicon at 620°C. The time intervals between each pictu-e are as indicated.

Fig. 43. The comparison between the defect structures in boron ion implanted silicon after annealing at 800°C for 30 min (Fig. A) and HVEM on boron doped silicon at 620°C (Fig. B).

Fig. 44. Showing the effect of irradiation temperature on the defect structures in high voltage electron irradiated boron doped silicon.

Fig. 45. The schematic diagram on the formation of boron precipitates by the proposed replacement mechanism during high energy electron irradiation.

Fig. 46. The W.B.D.F. pictures of some defects with different s values. The variation of contrast due to the depth of defects and slightly change in s values is clearly shown. $s = 6\times10^{-3}$, 4.7×10^{-3} and 7.56×10^{-3} Å^{-1} from 1-3.

0 0 0 0 4 3 0 2 9 7 9

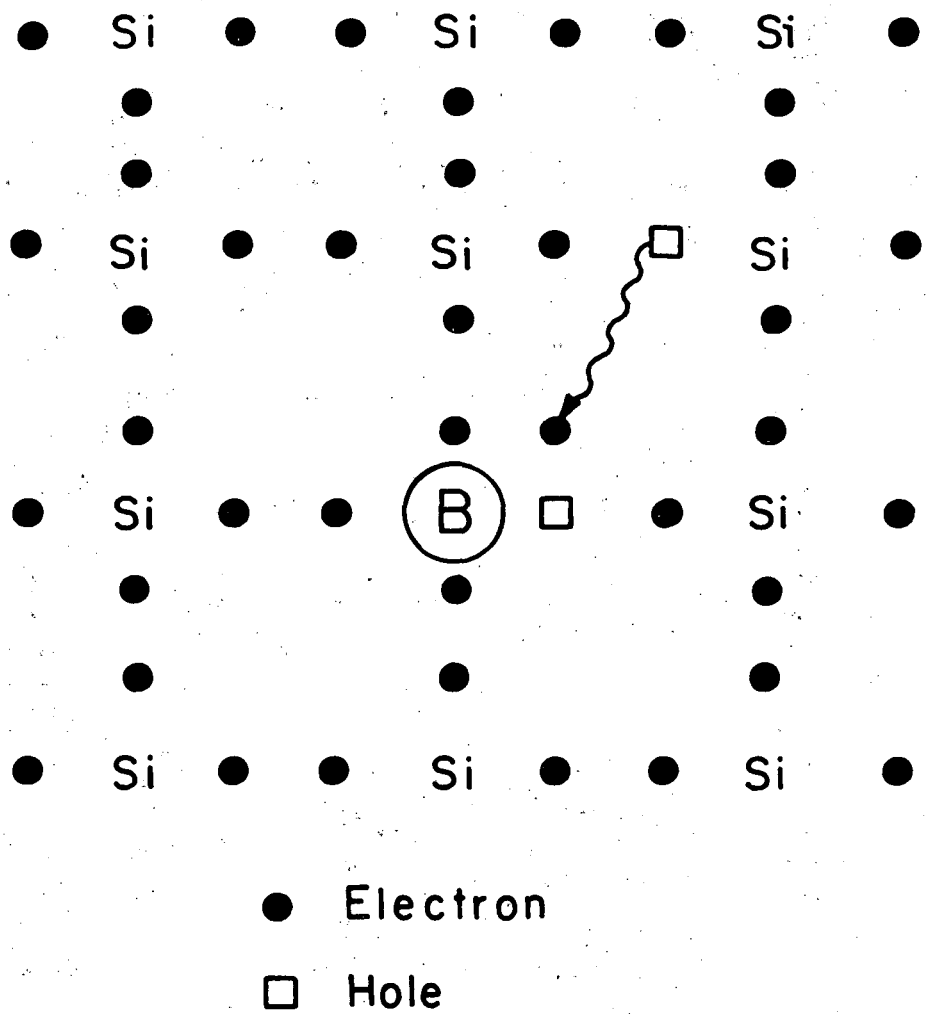

XBL 753-5930

Fig. 1

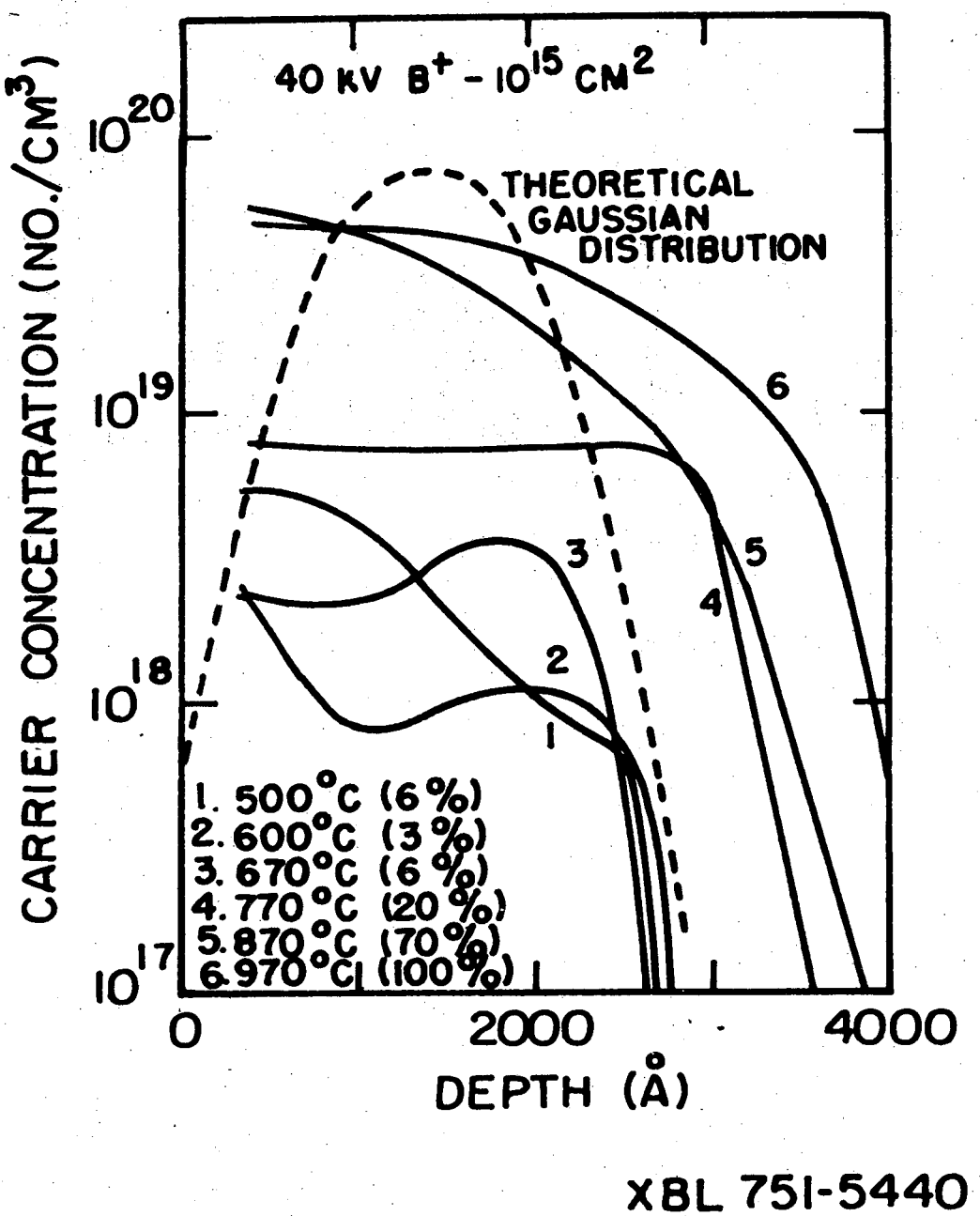

XBL 751-5440

Fig. 2

0 0 0 0 4 3 0 2 9 8 0

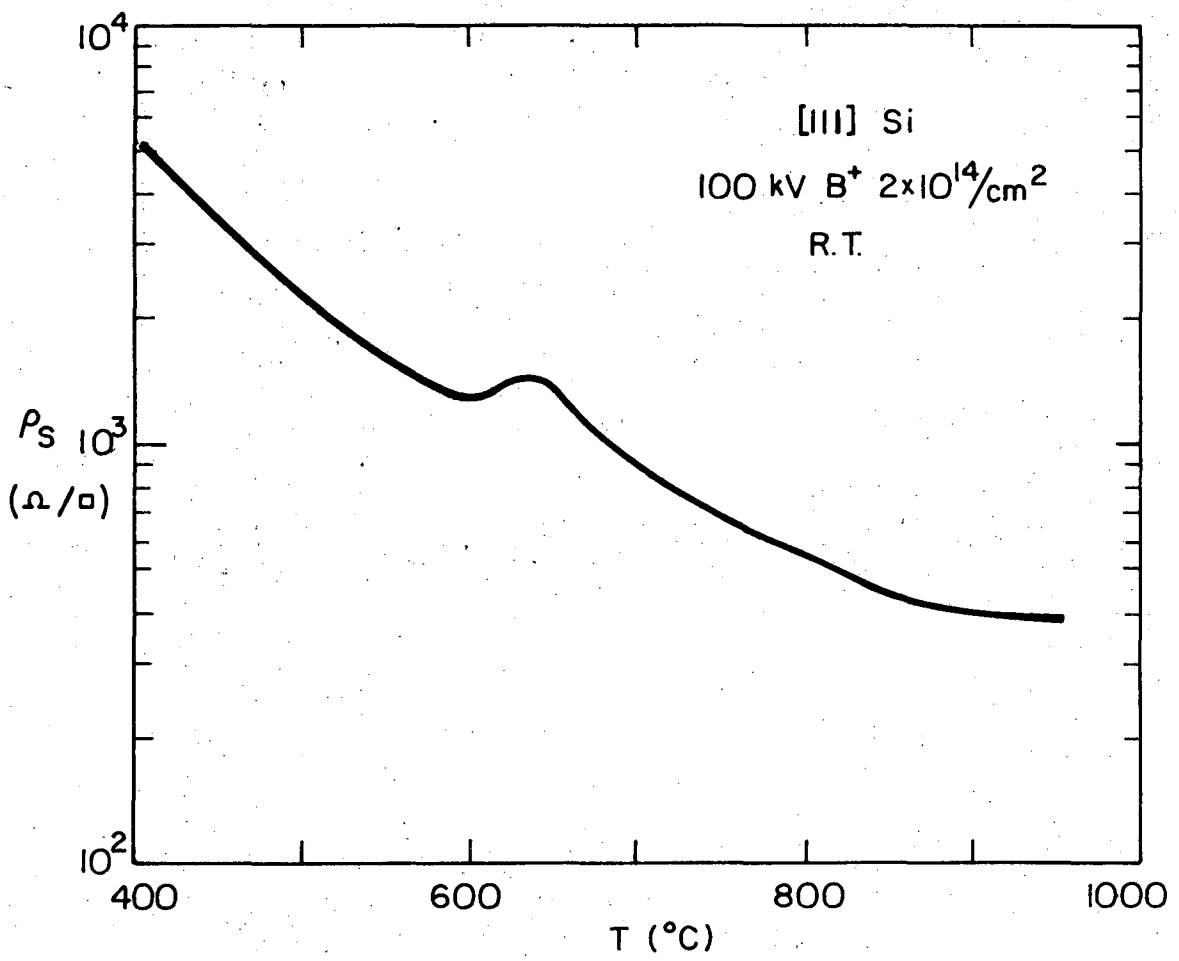

XBL 7412-7633

Fig. 3

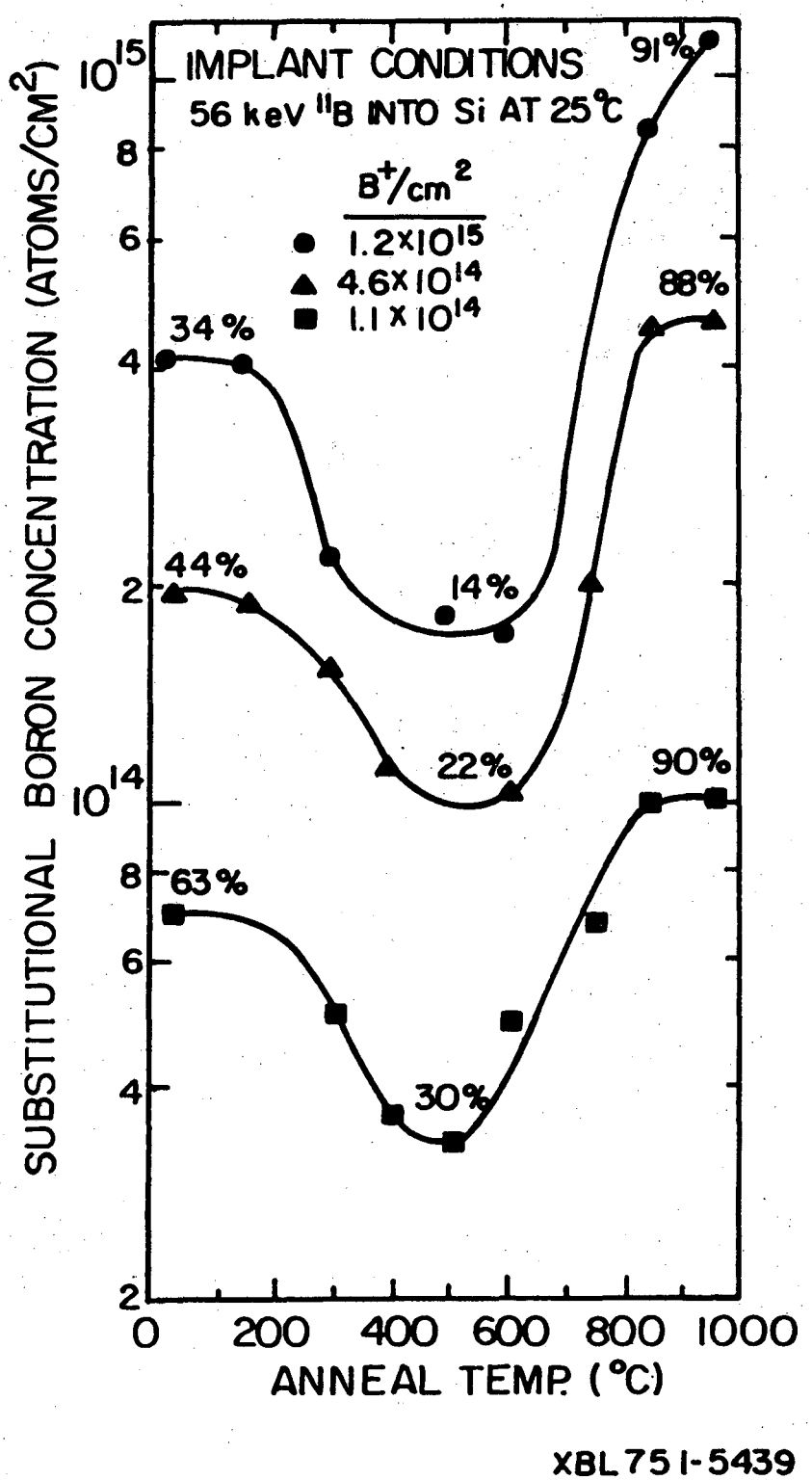

XBL 751-5439

Fig. 4

0 0 0 0 4 3 0 2 9 8 1

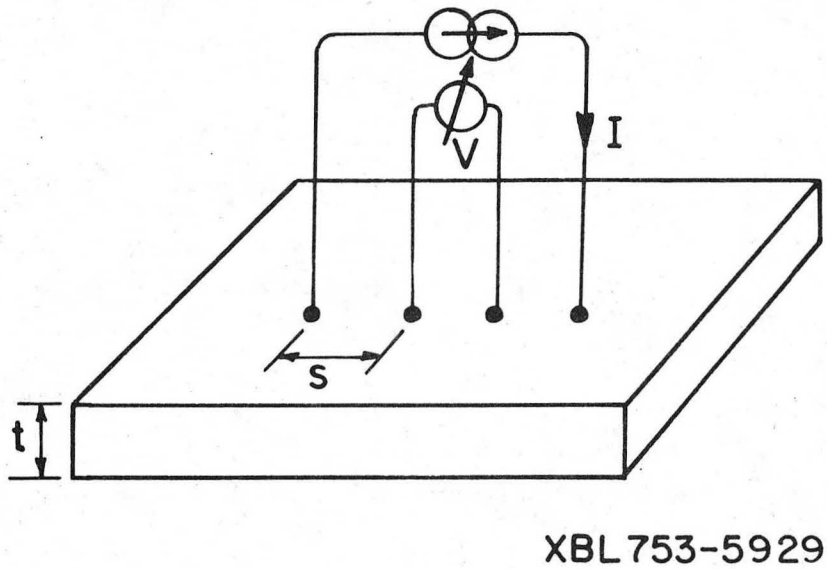

Fig. 5

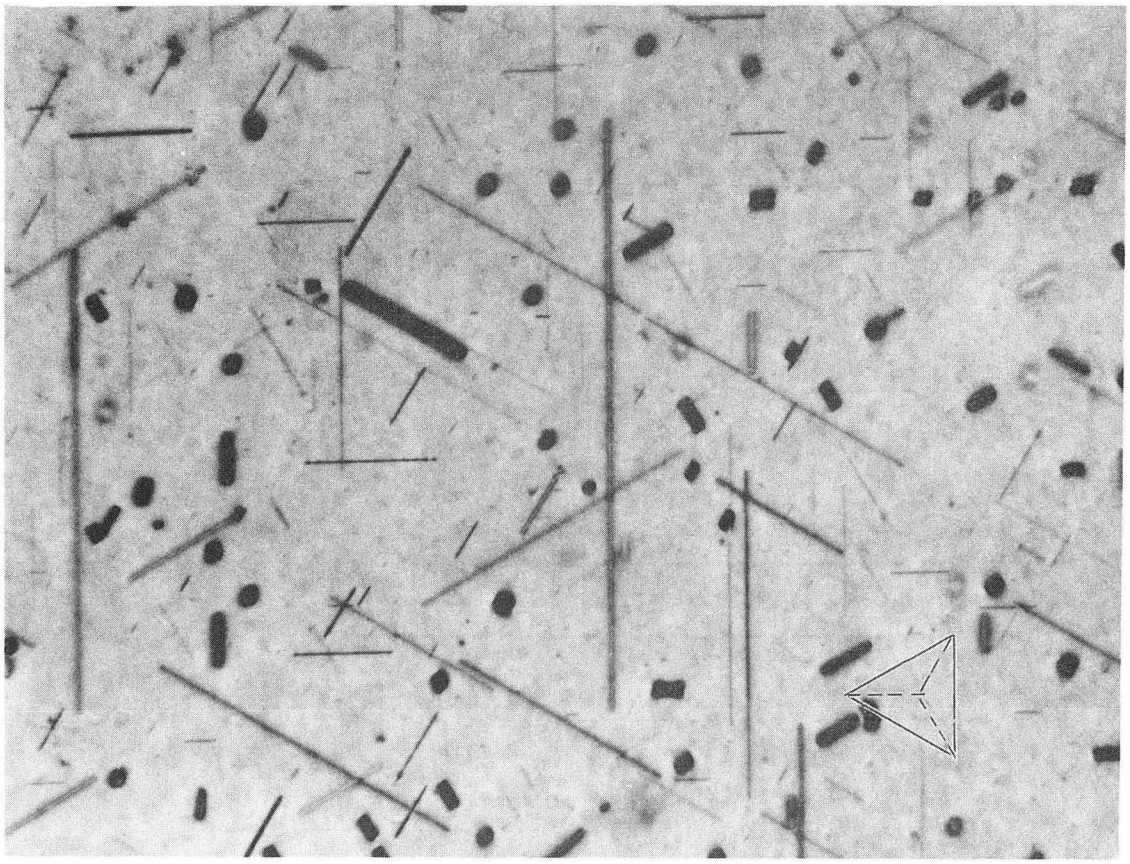

XBB 7411-7673

Fig. 6

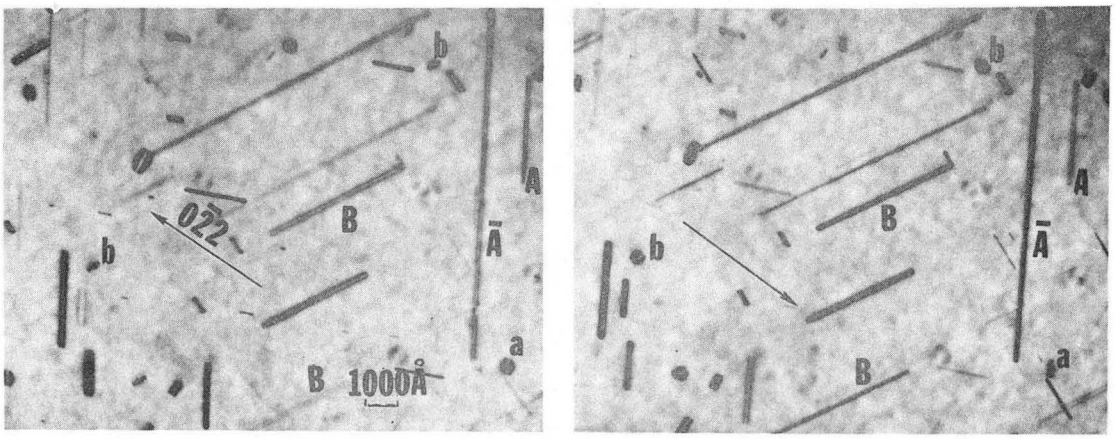

XBB 7411-7674

Fig. 7

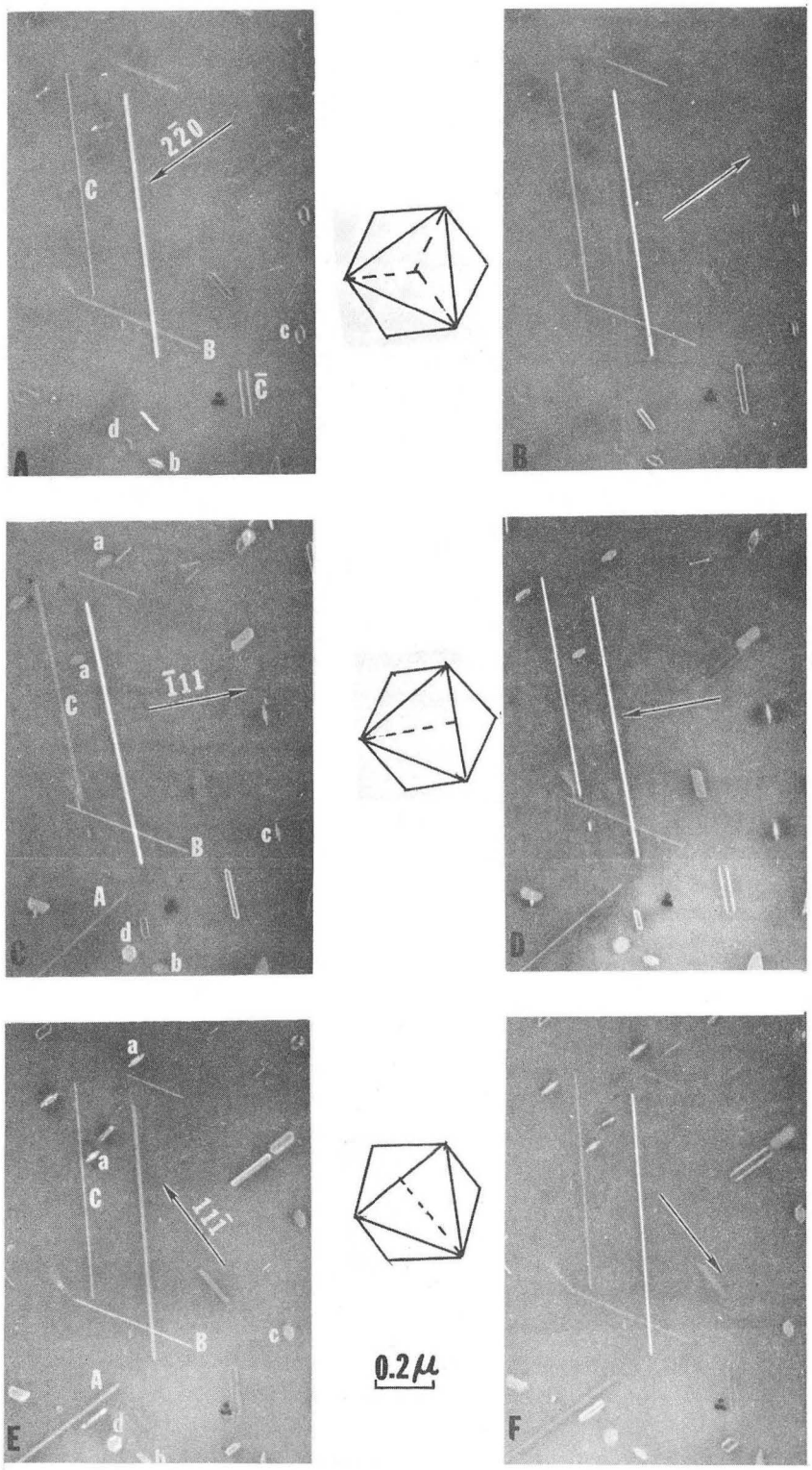

XBB 753-1850A

Fig. 8

0 0 0 0 4 3 0 2 9 8 3

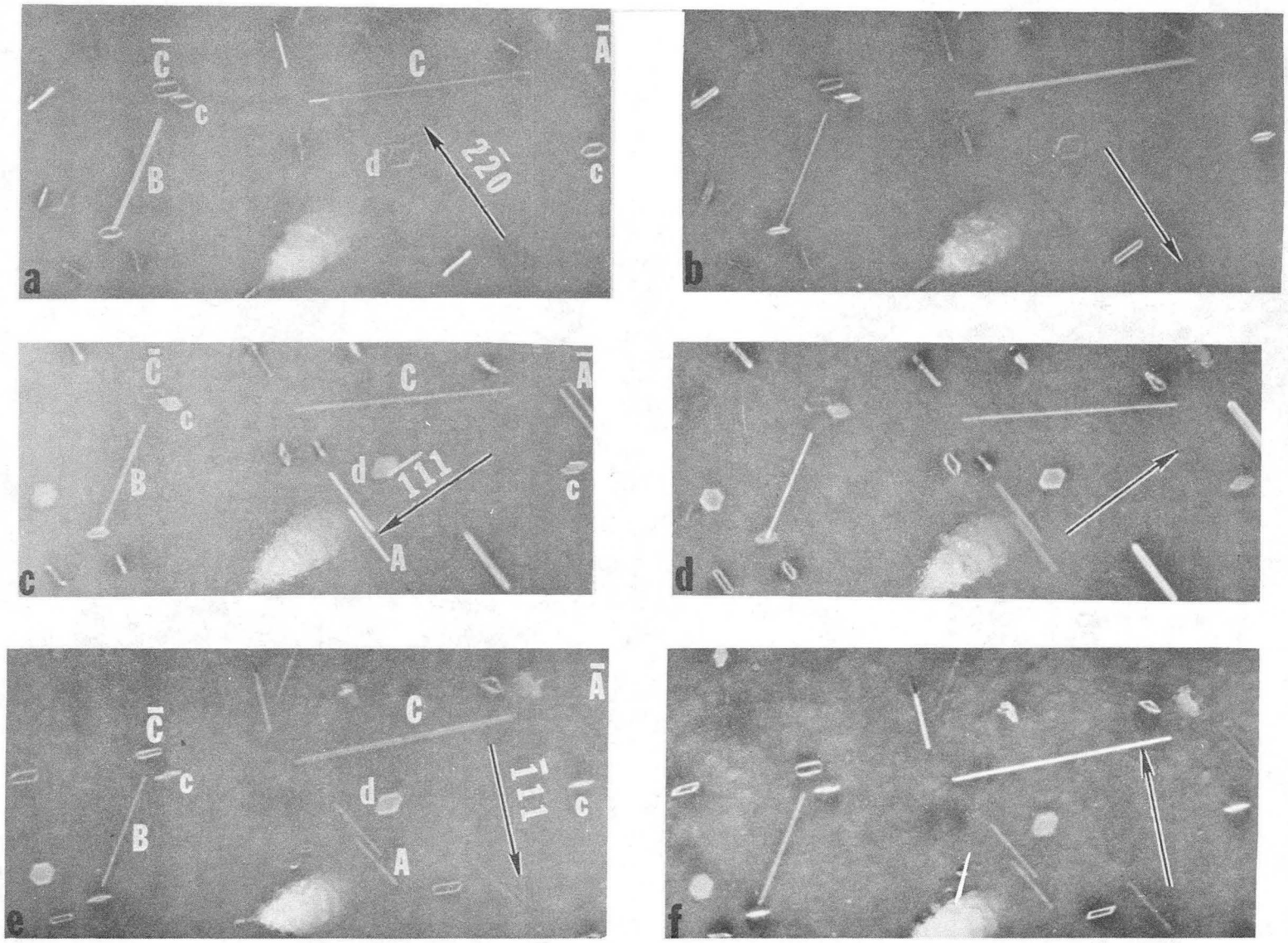

XBB 753-1856

Fig. 8i

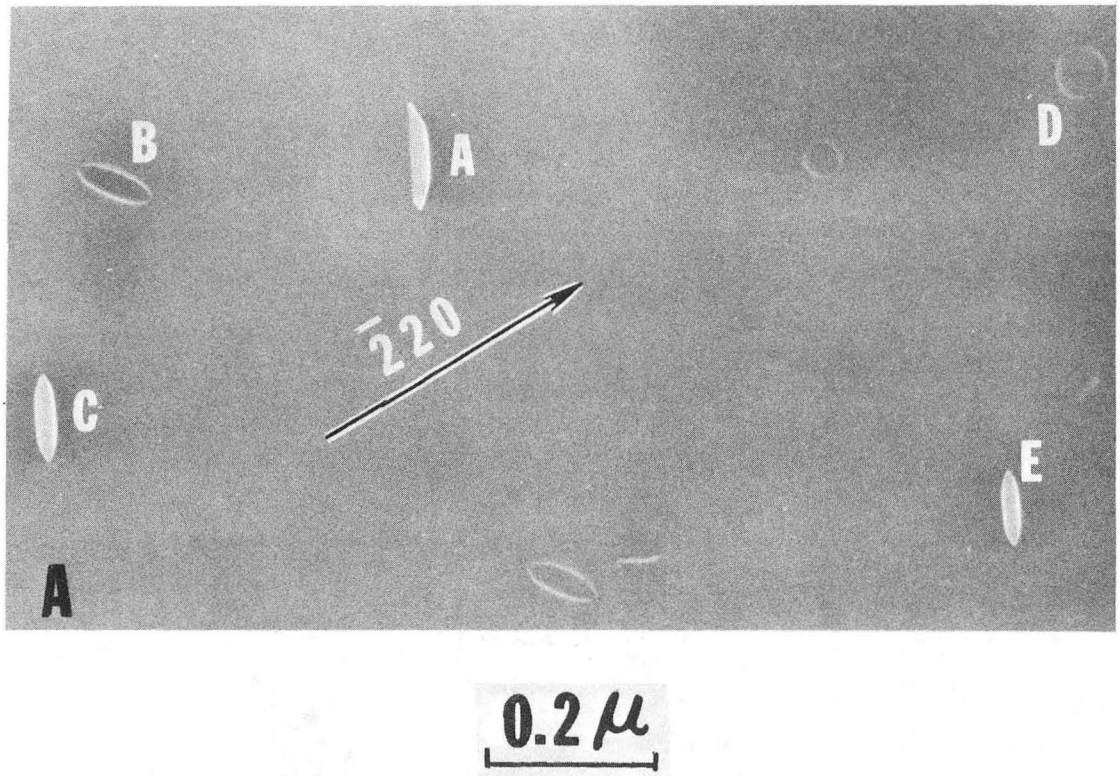

XBB 753-1855A

Fig. 9

0 0 0 0 4 3 0 2 9 8 4

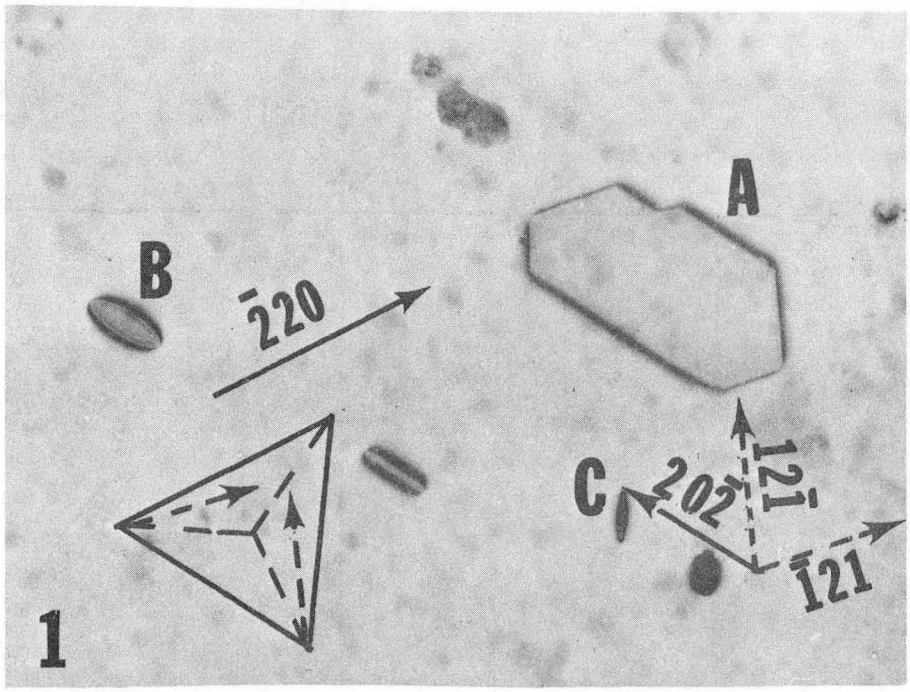

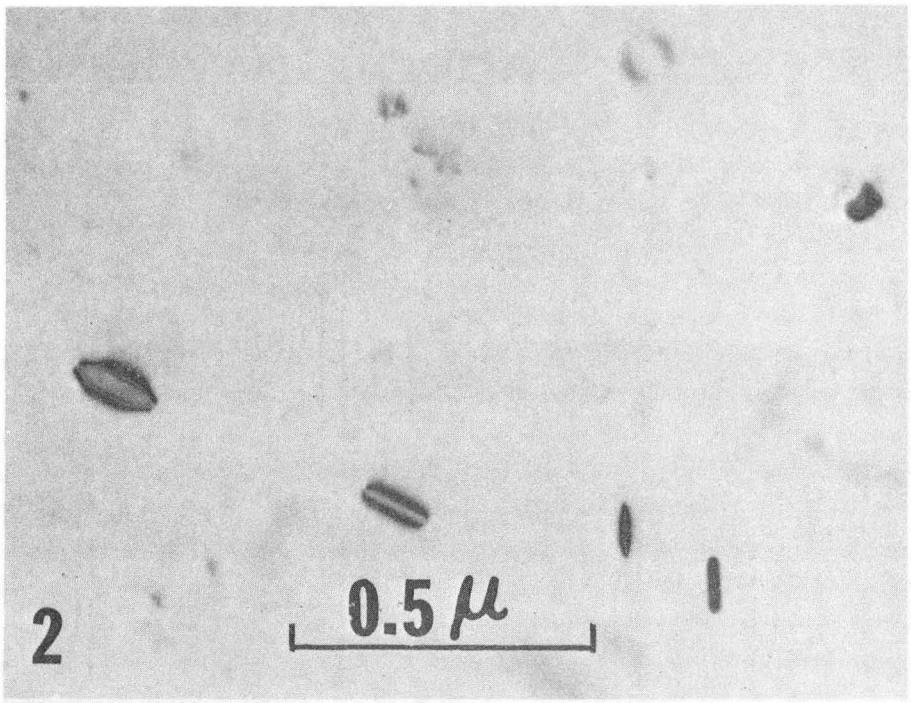

XBB 753-1854

Fig. 10

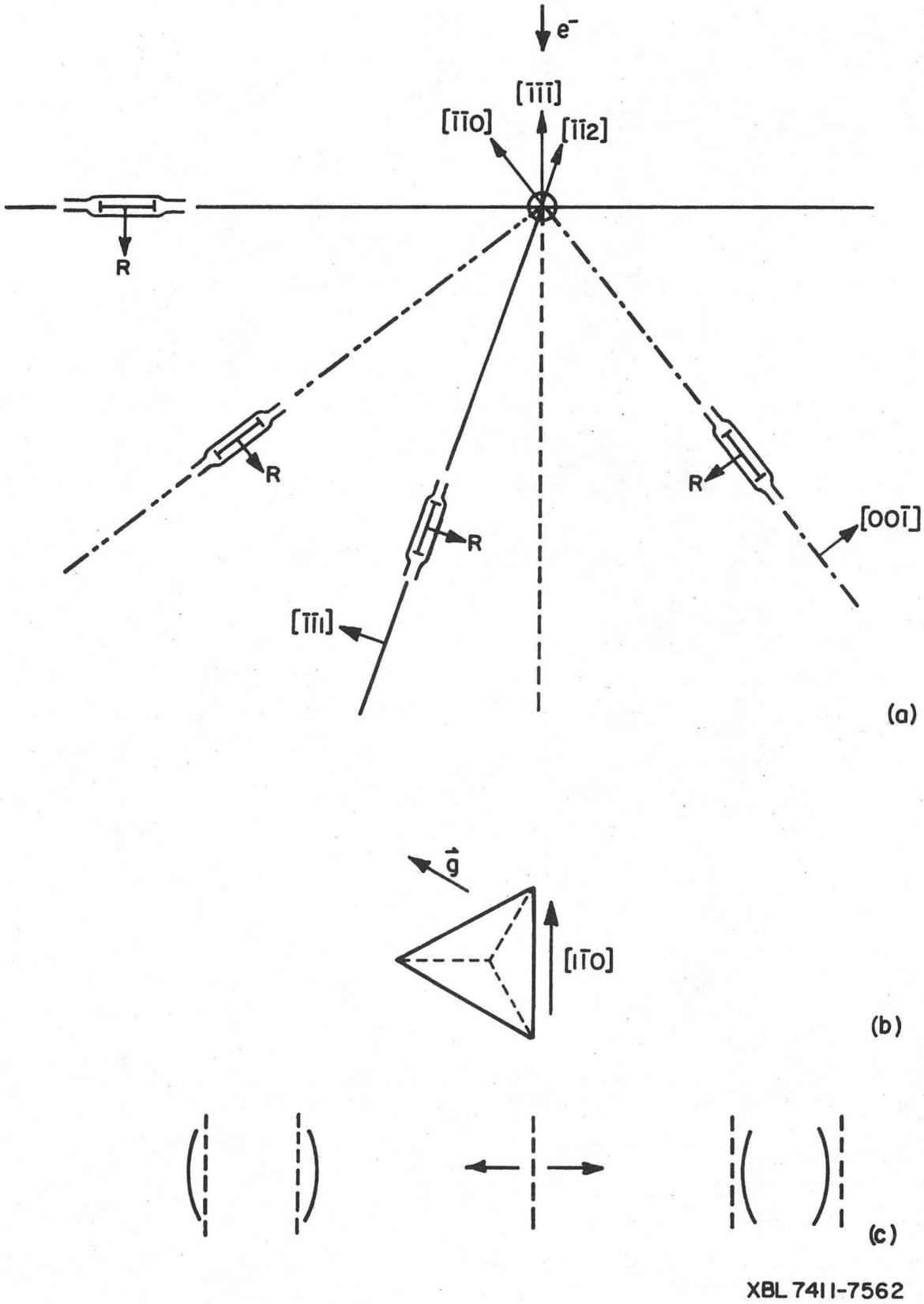

Fig. 11

0 0 0 0 4 3 0 2 9 8 5

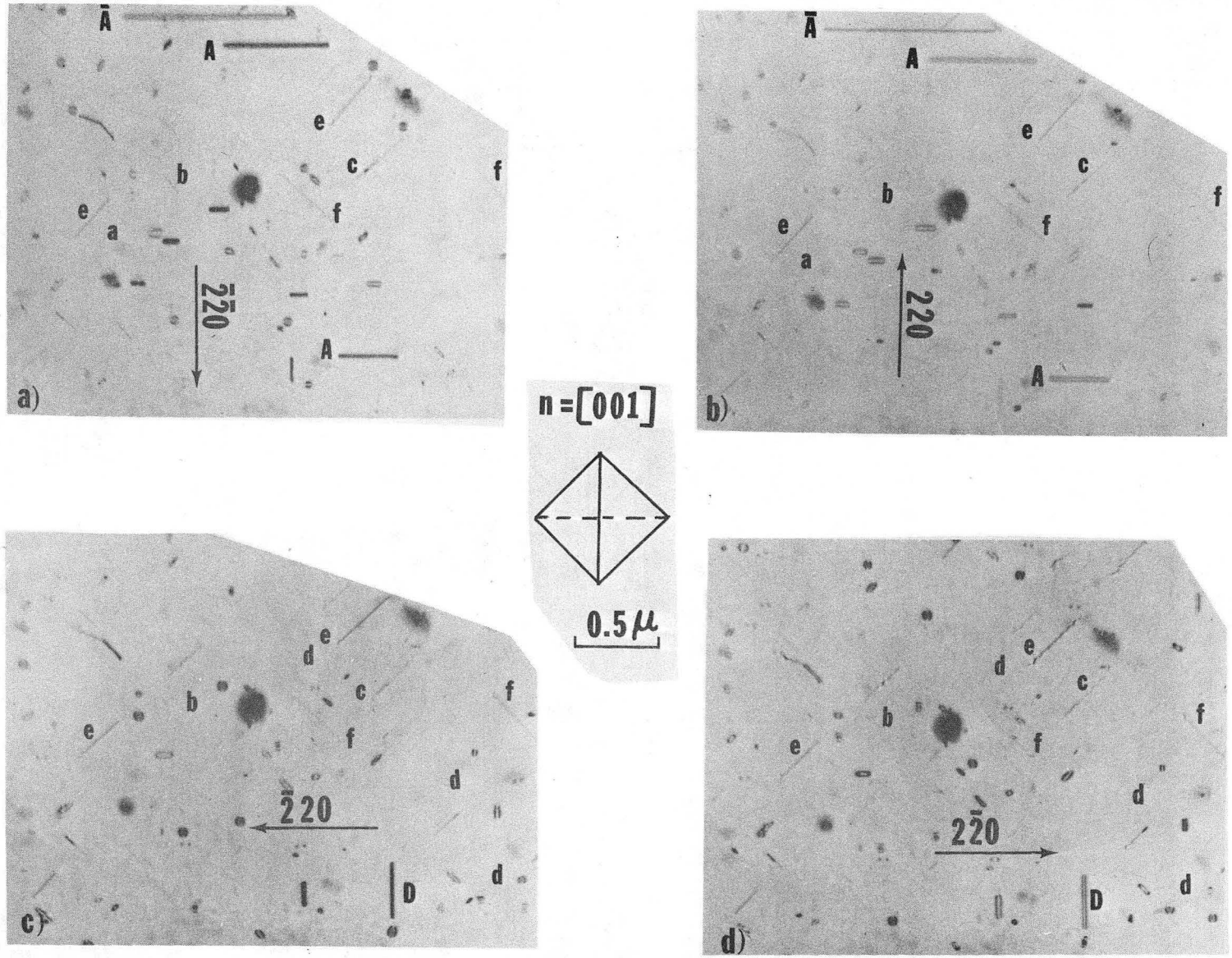

XBB 754-3054

Fig. 12

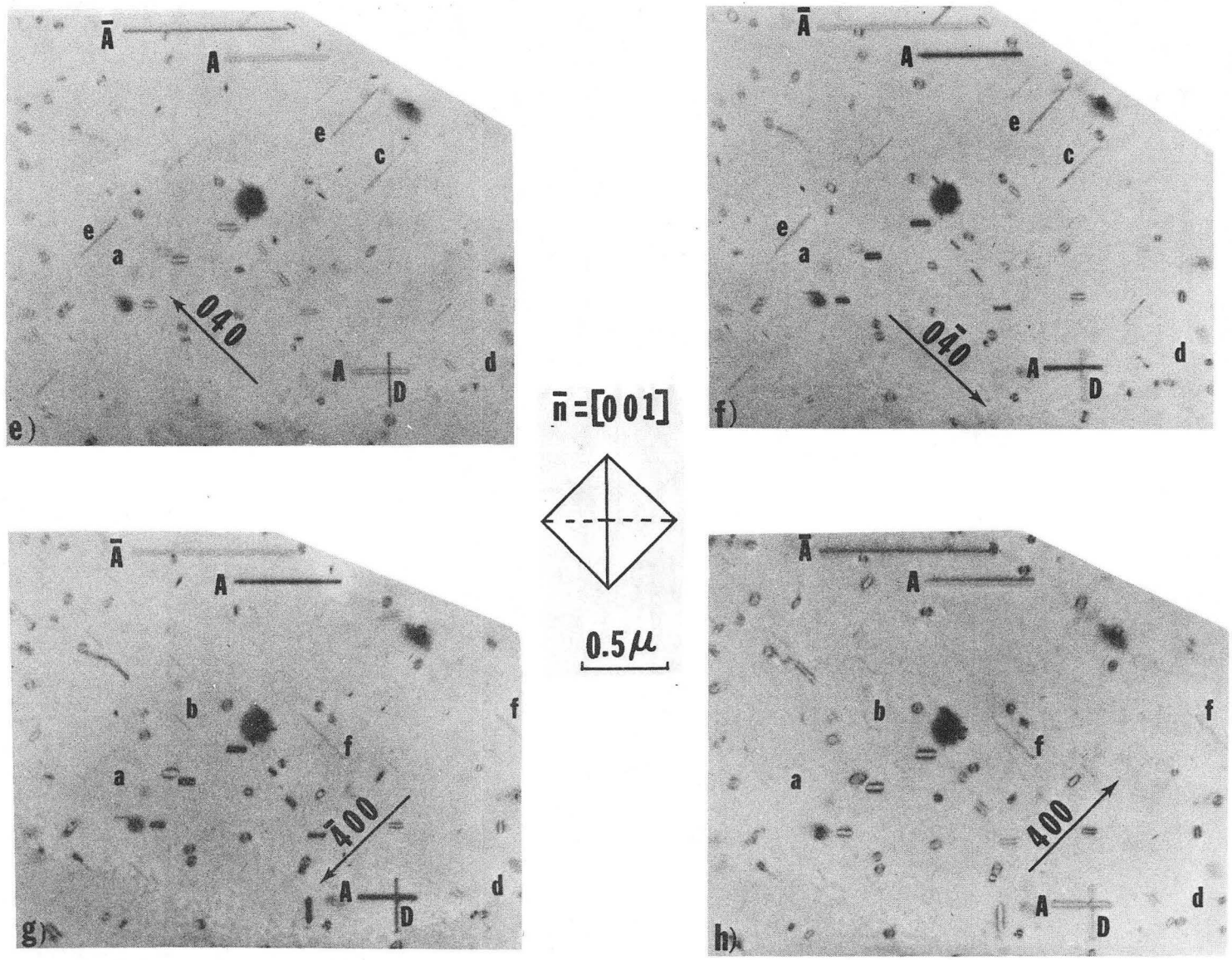

XBB 754-3053

Fig. 12 cont.

0 0 0 0 4 3 0 2 9 8 6

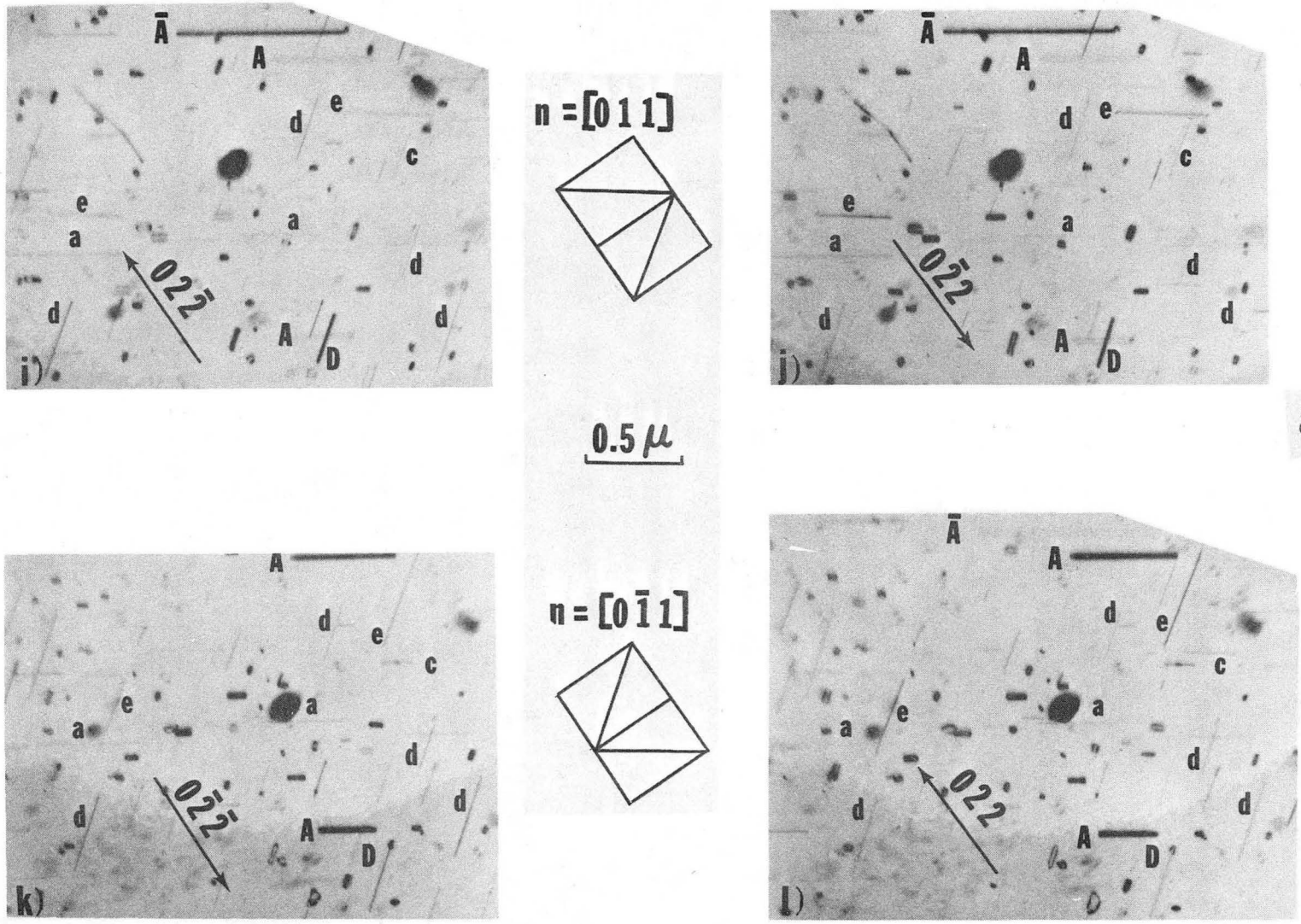

XBB 754-3055

Fig. 12 cont.

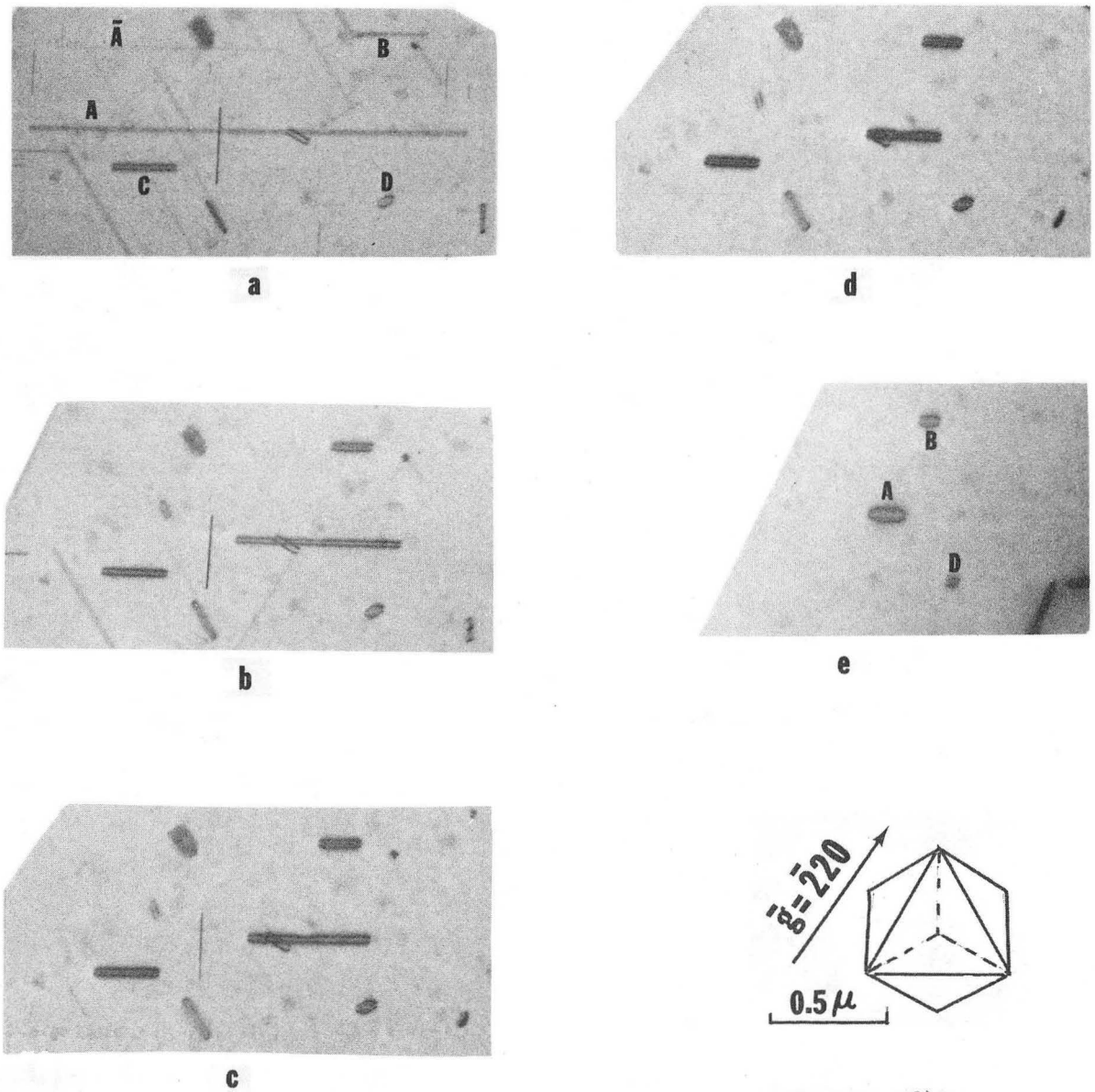

XBB 753-1847

Fig. 13

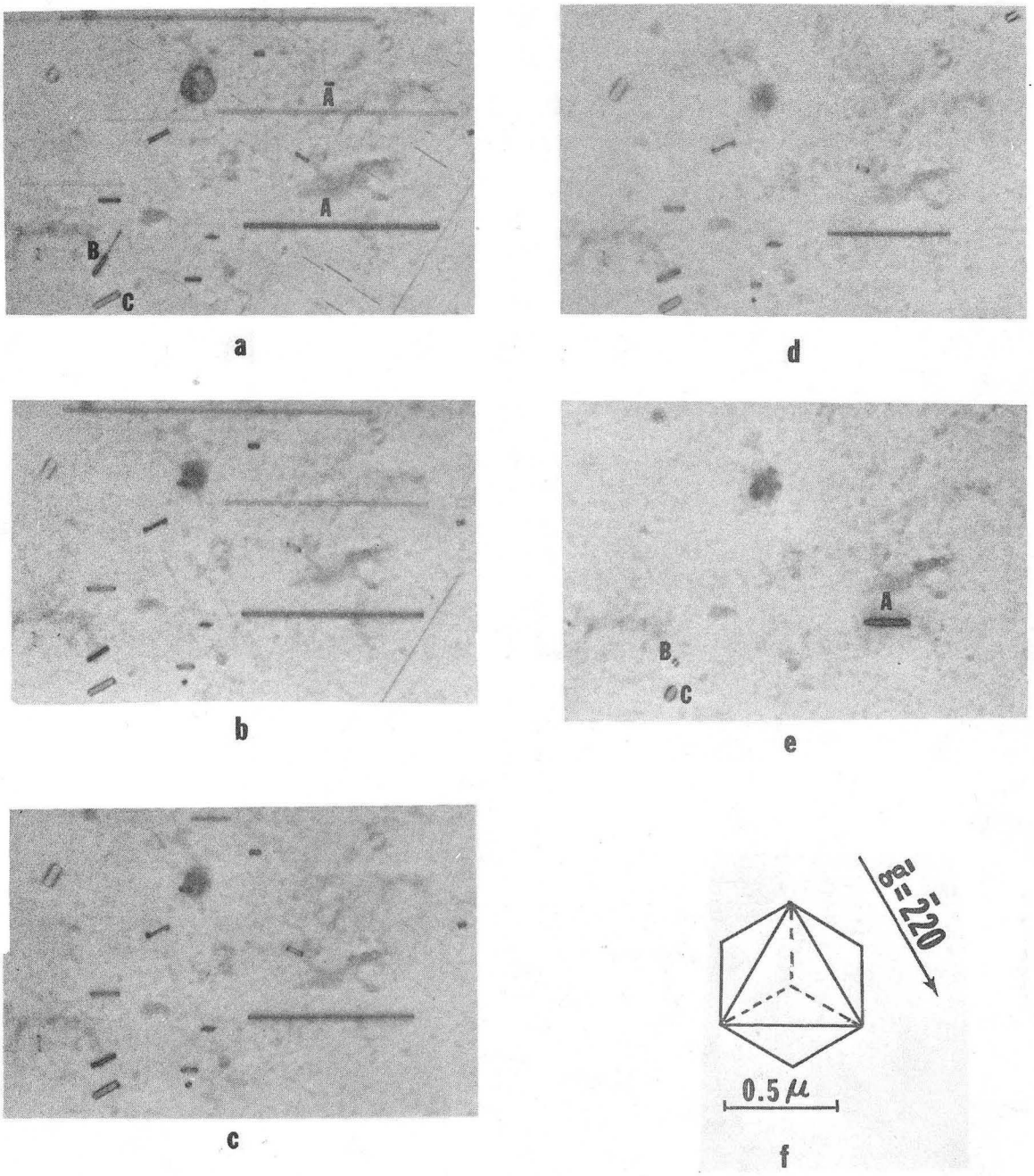

XBB 753-1846

Fig. 14

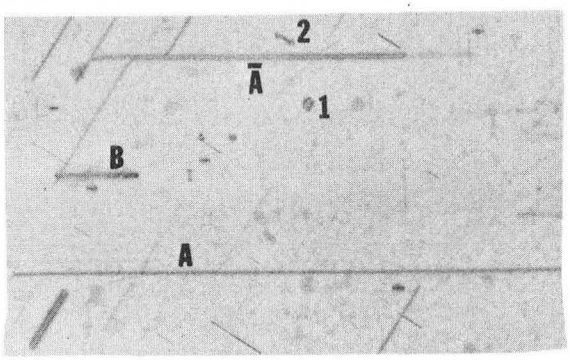

a

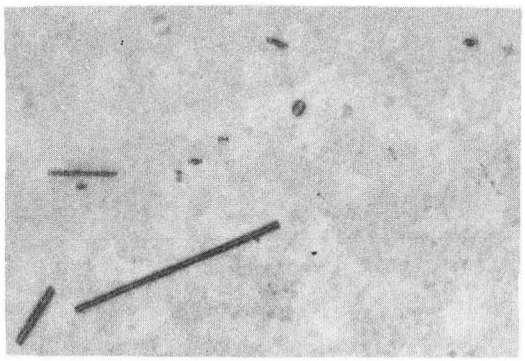

d

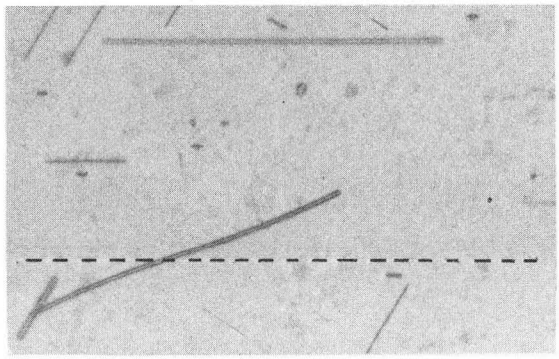

b

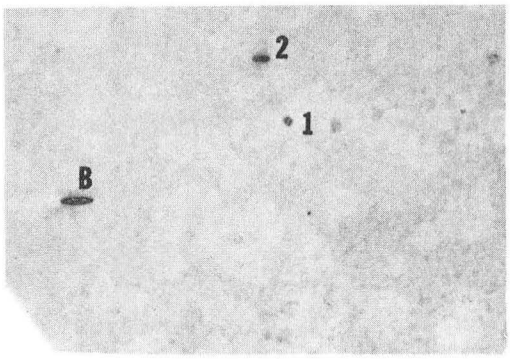

e

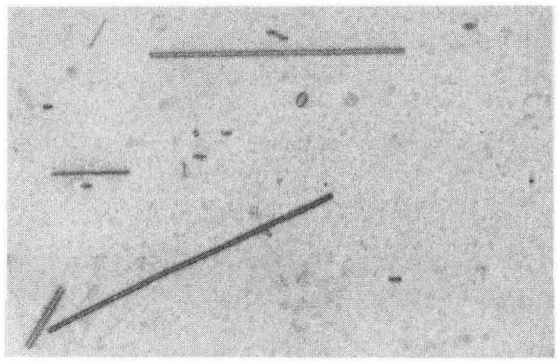

c

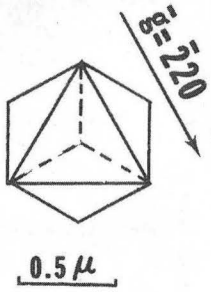

f

XBB 753-1845

Fig. 15

0 0 0 0 4 3 0 2 9 8 8

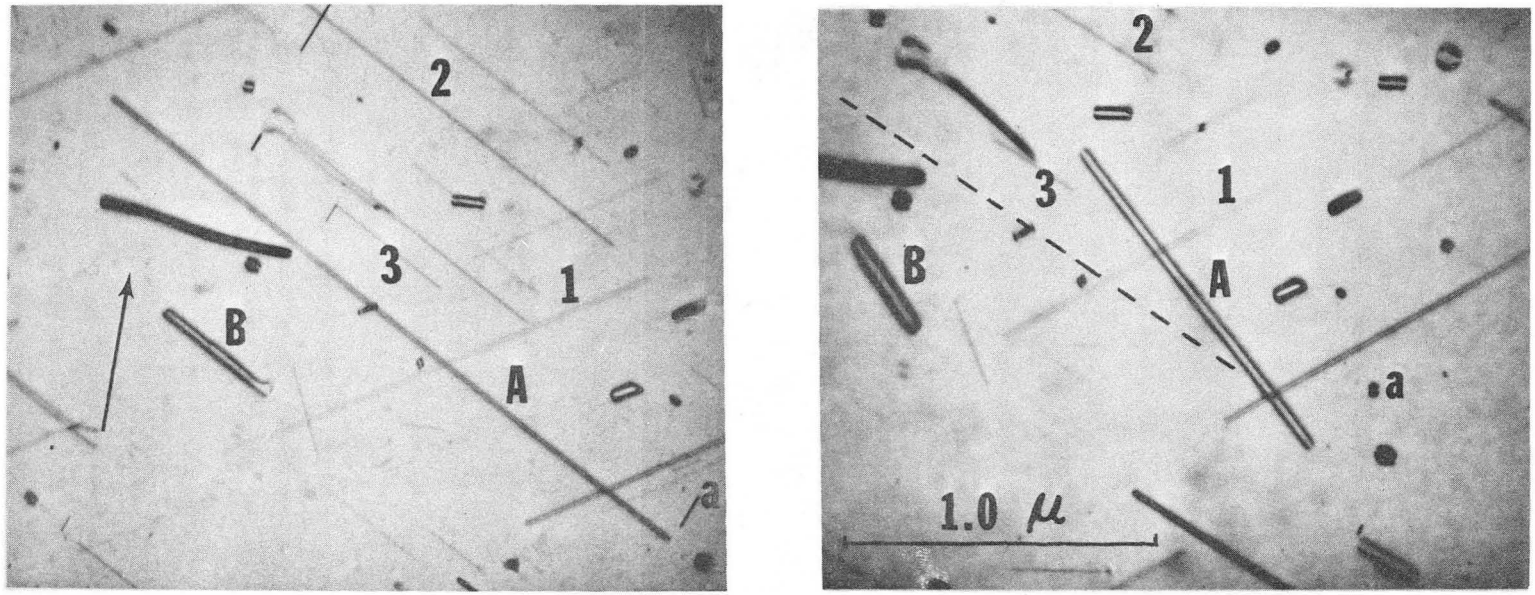

a b

XBB 7411-7749

Fig. 15A

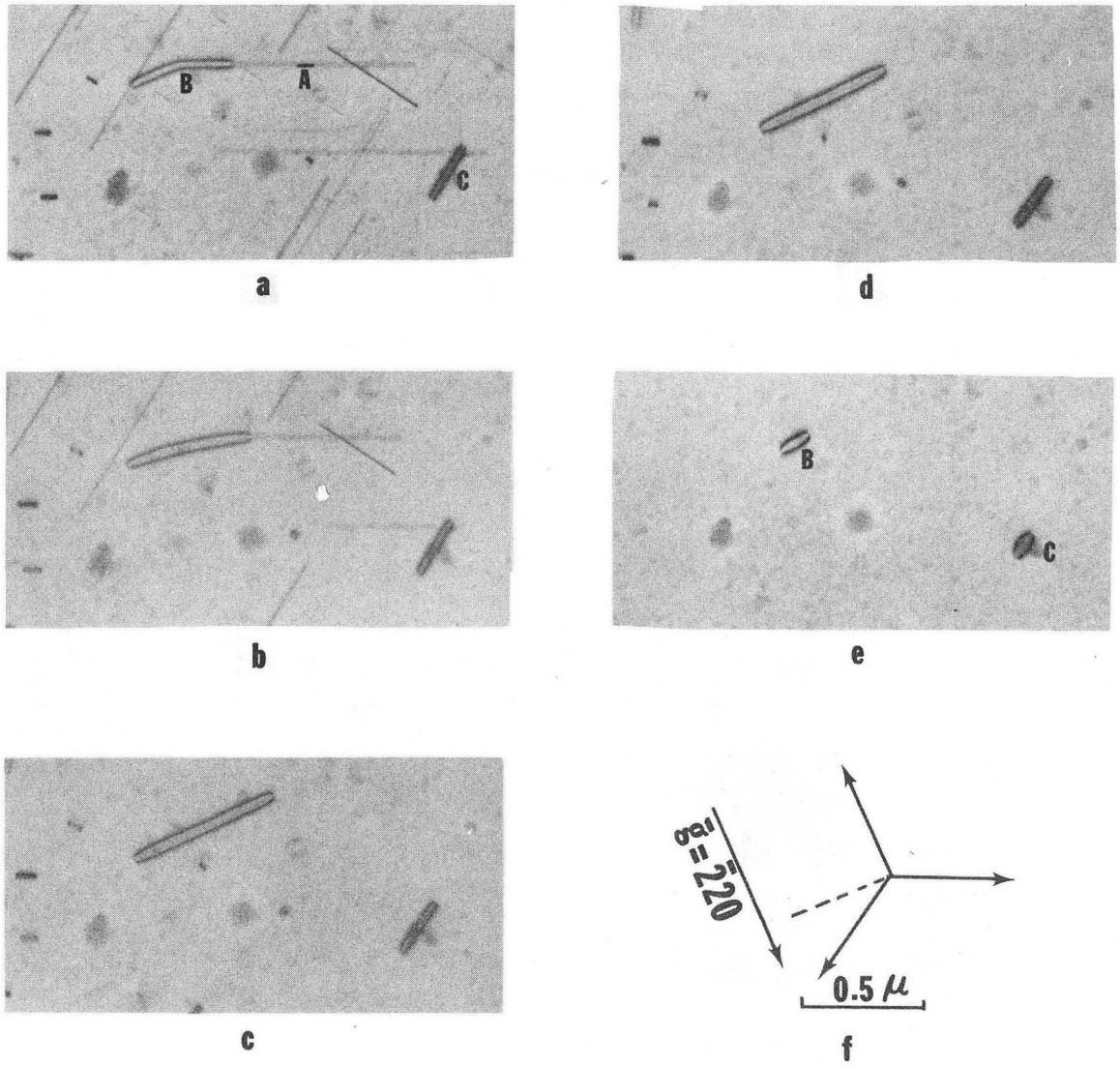

XBB 753-1848

Fig. 16

0 0 0 0 4 3 0 2 9 8 9

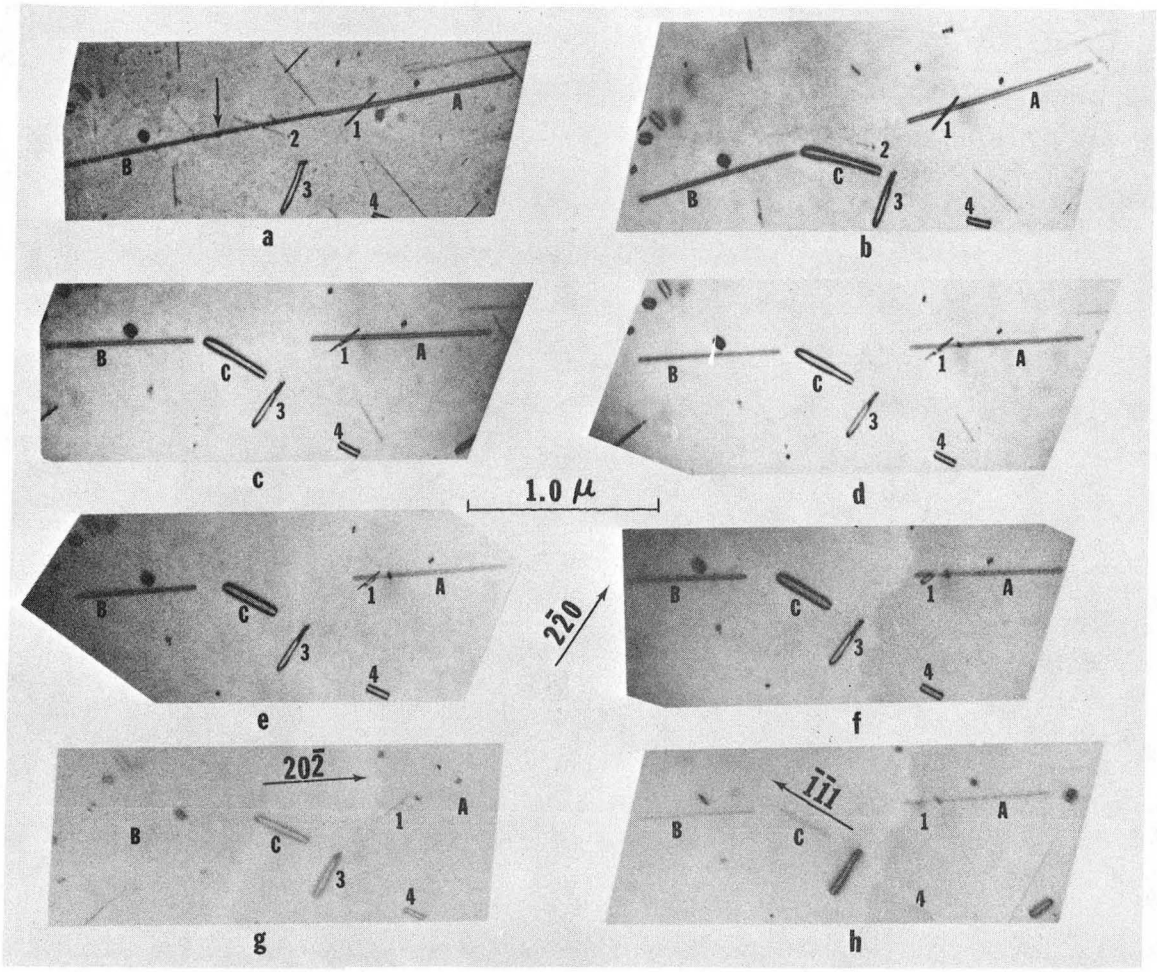

XBB 7411-7743

Fig. 17

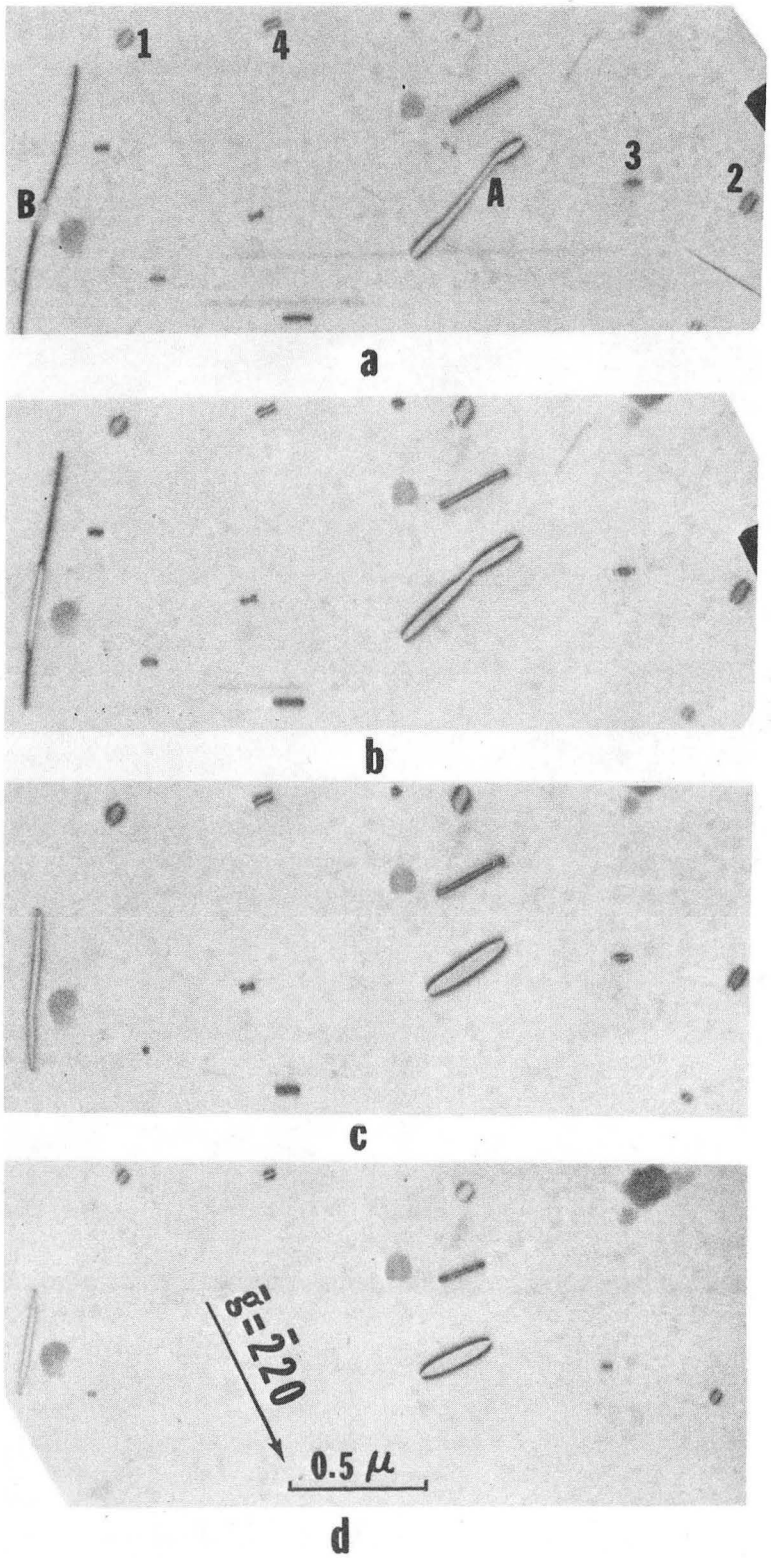

XBB 753-1844

Fig. 18

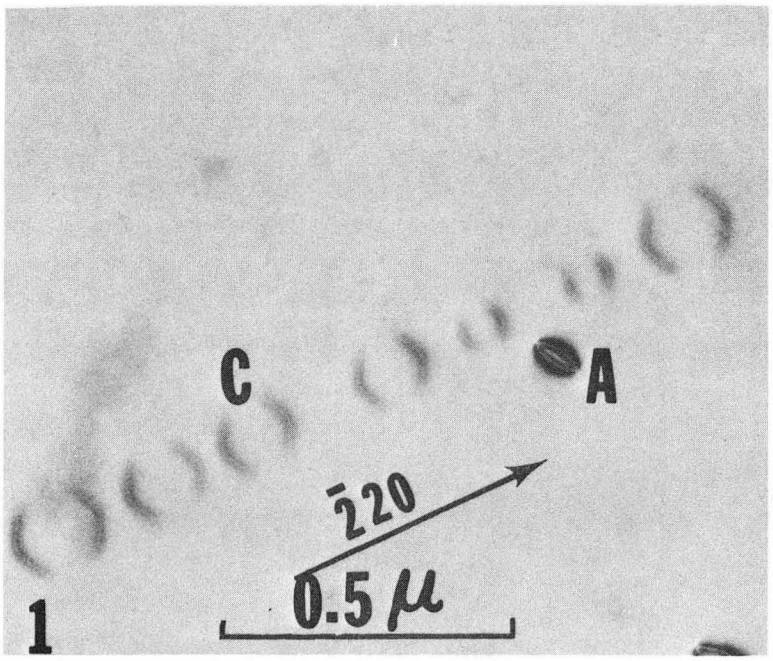

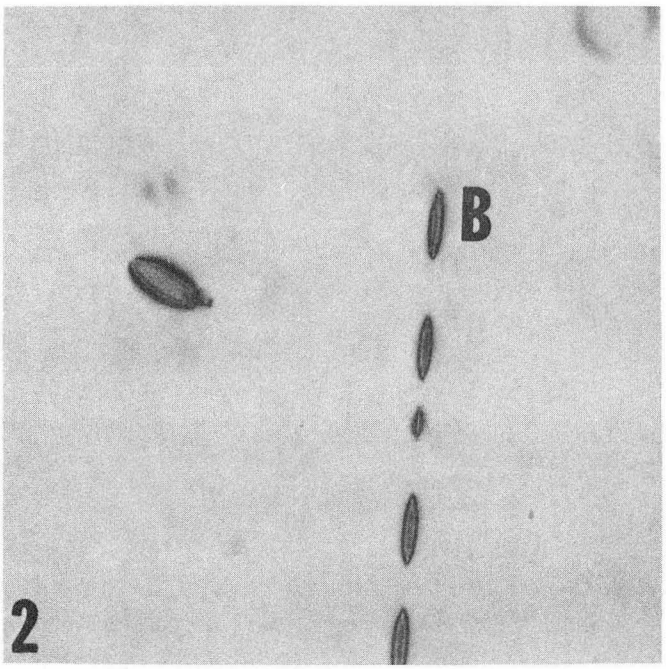

XBB 753-1851

Fig. 19

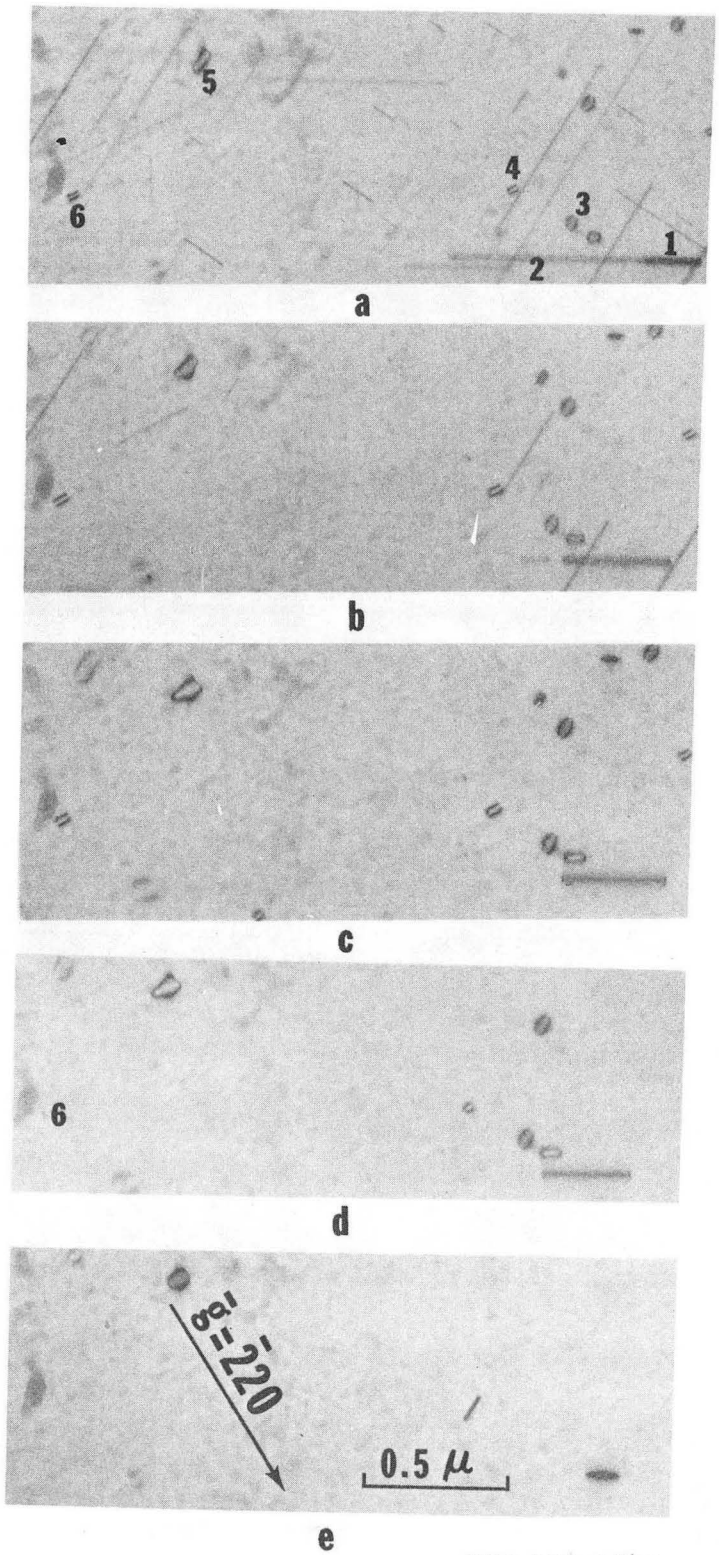

XBB 753-1842

Fig. 20

0 0 0 0 4 3 0 2 9 9 1

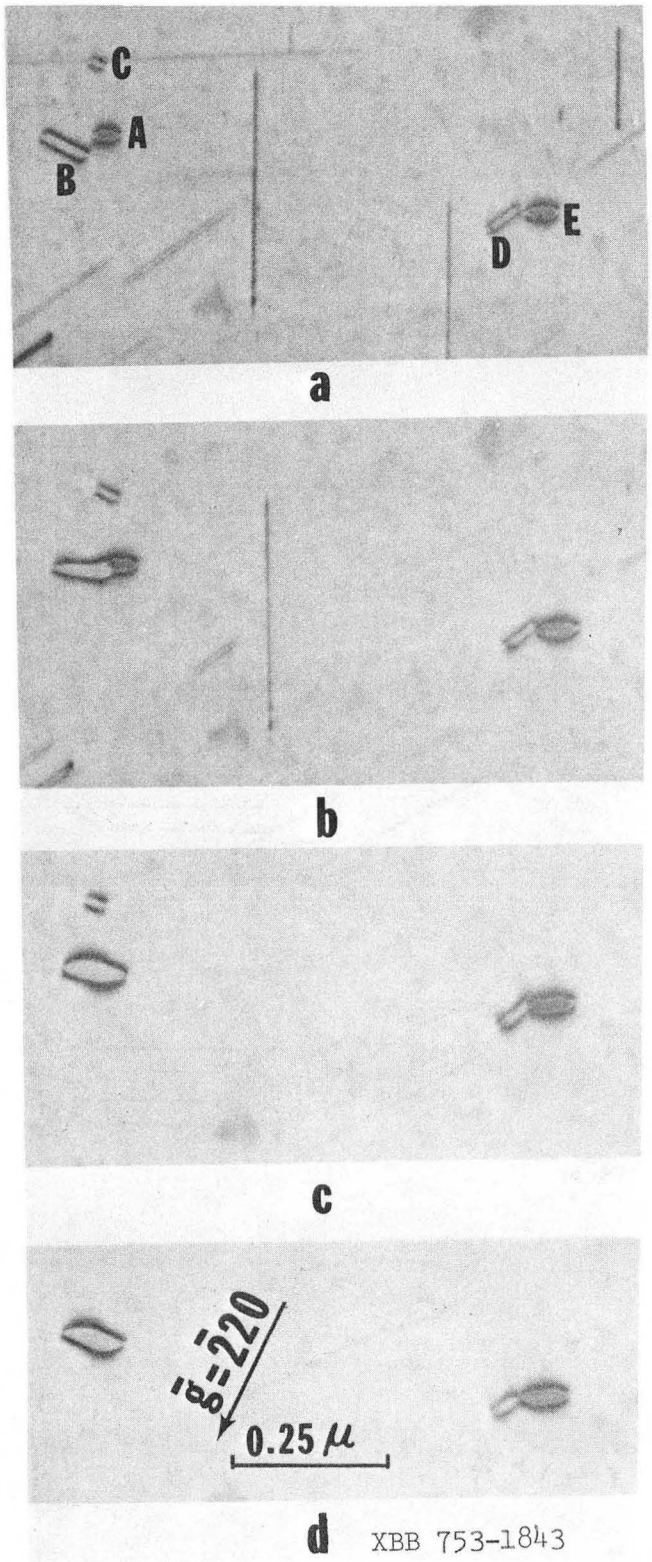

XBB 753-1843

Fig. 21

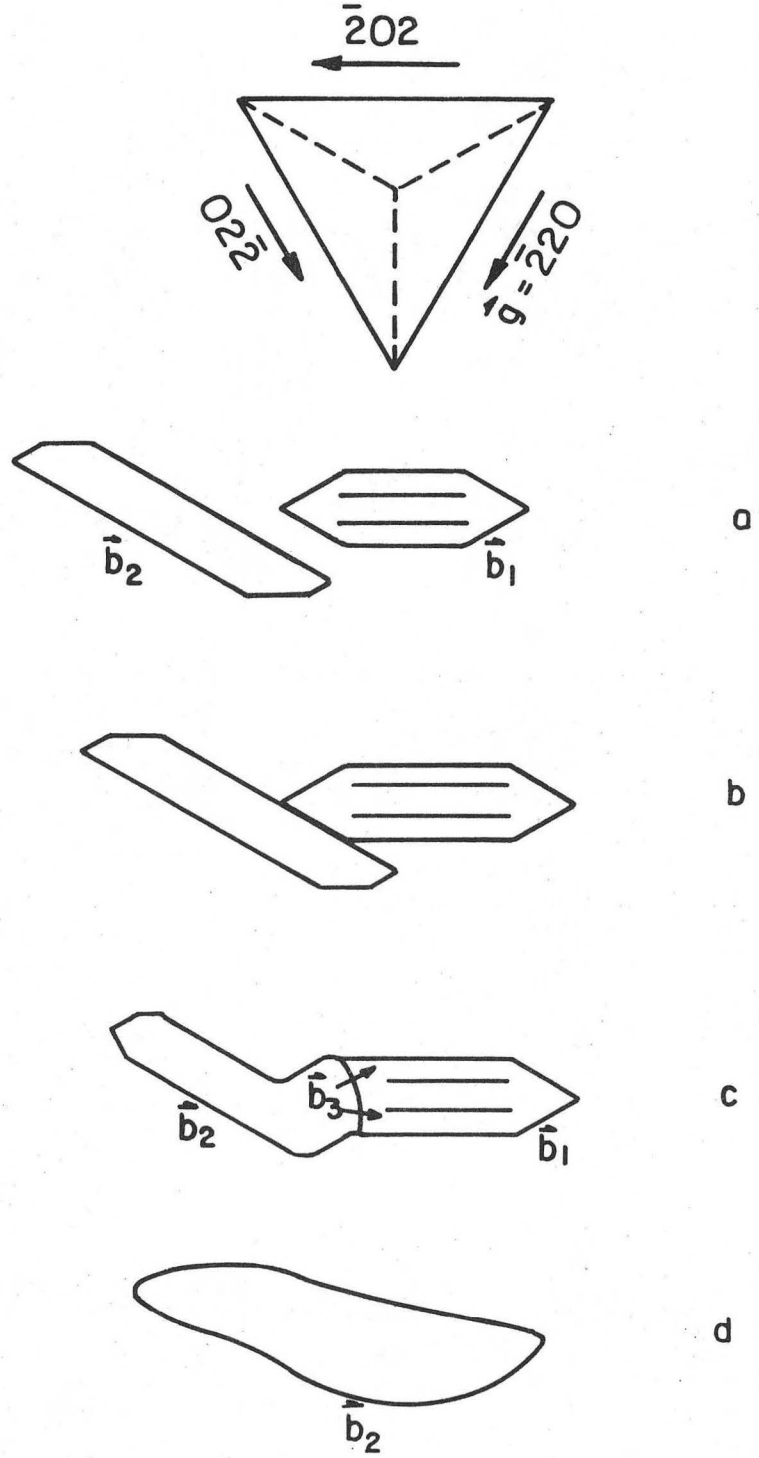

XBL 753-5927

Fig. 22

0 0 0 0 4 3 0 2 9 9 2

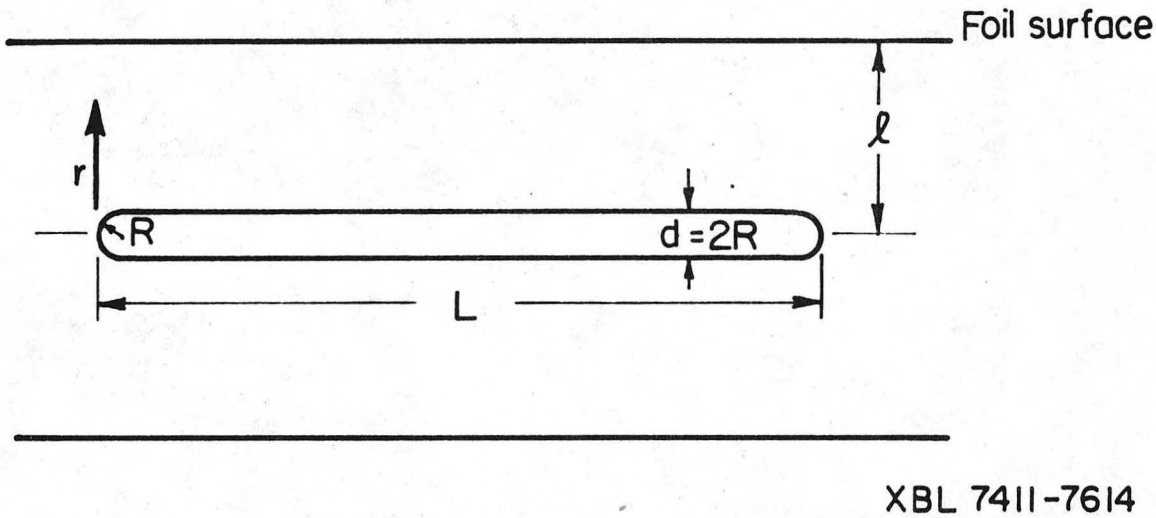

Fig. 23

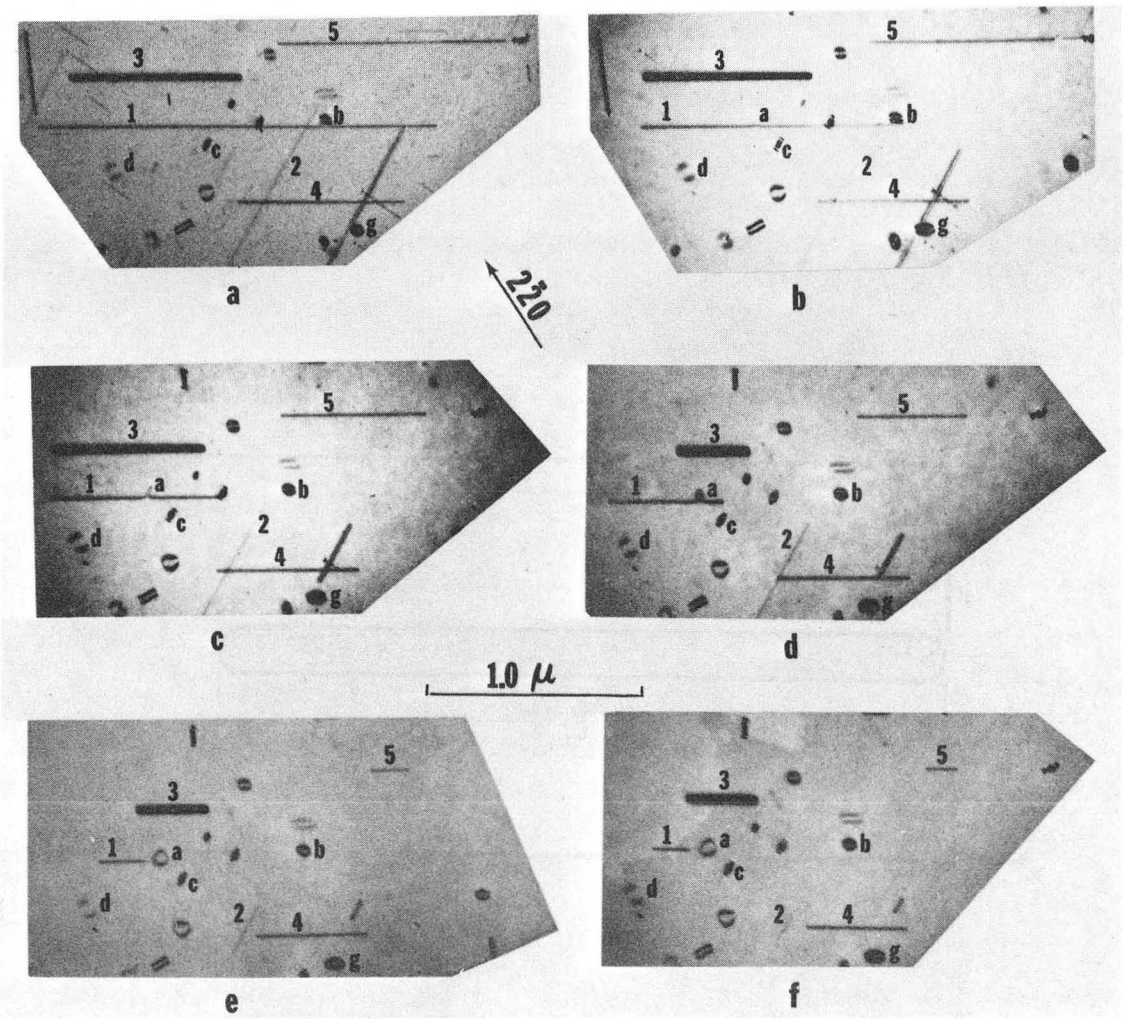

XBB 7411-7744

Fig. 24

0 0 0 0 4 3 0 2 9 9 3

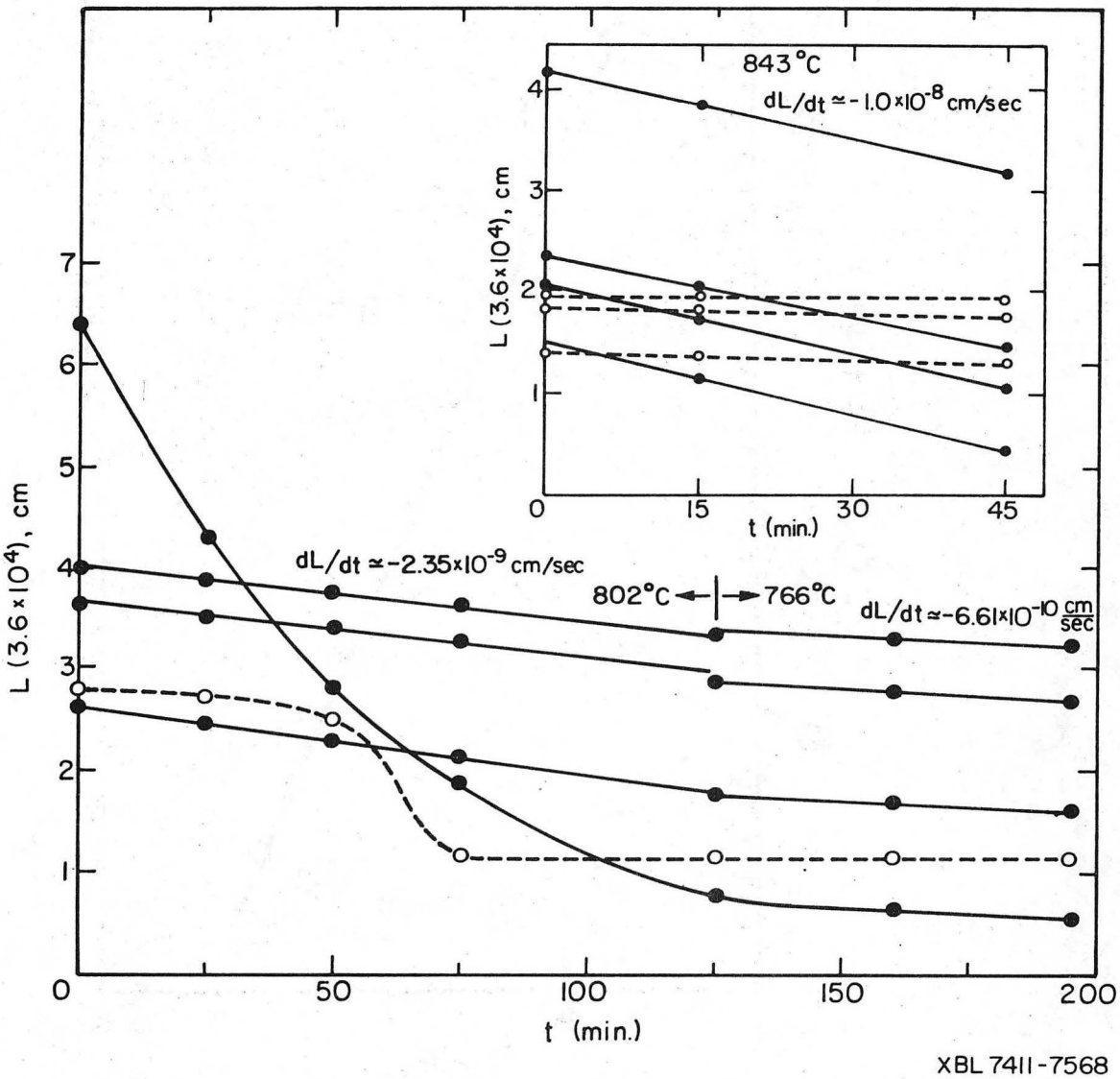

Fig. 25

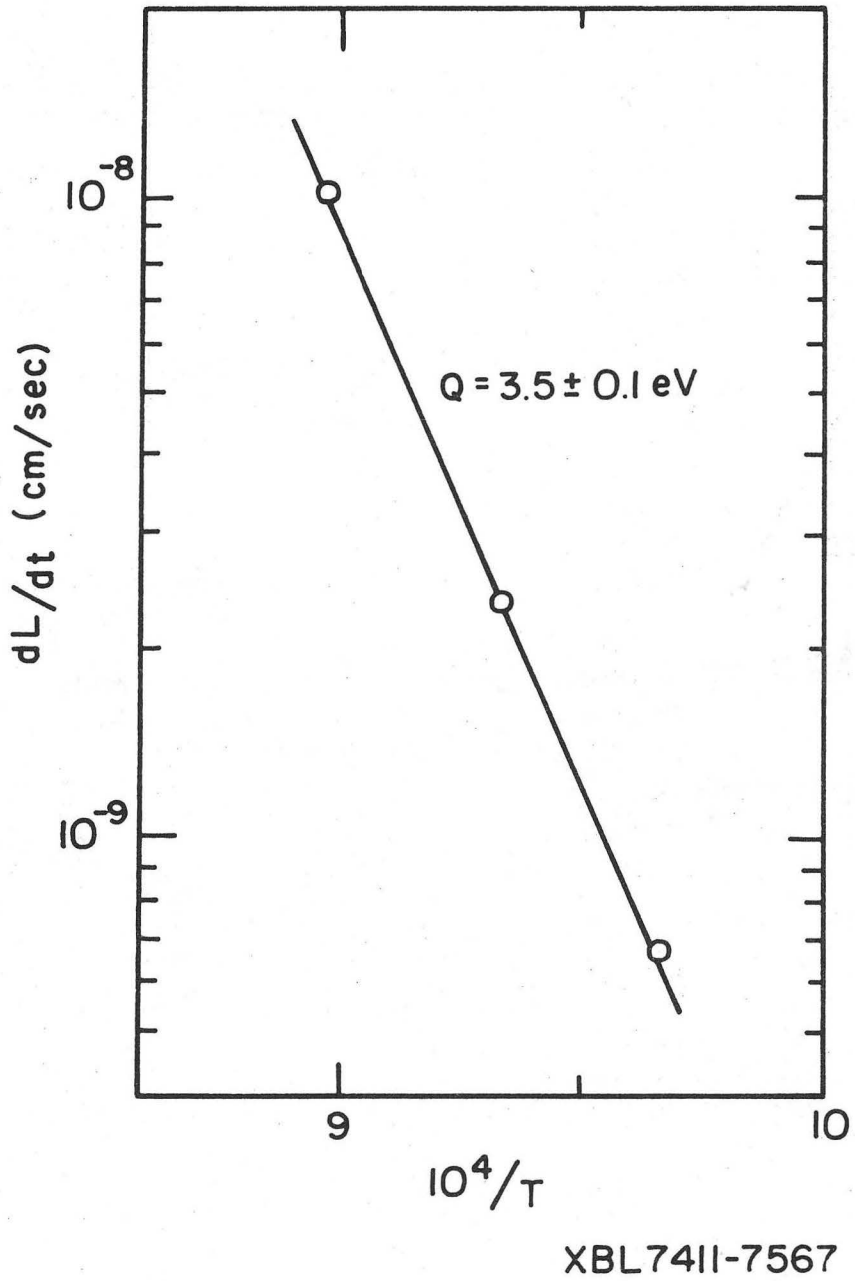

Fig. 26

0 0 0 0 4 3 0 2 9 9 4

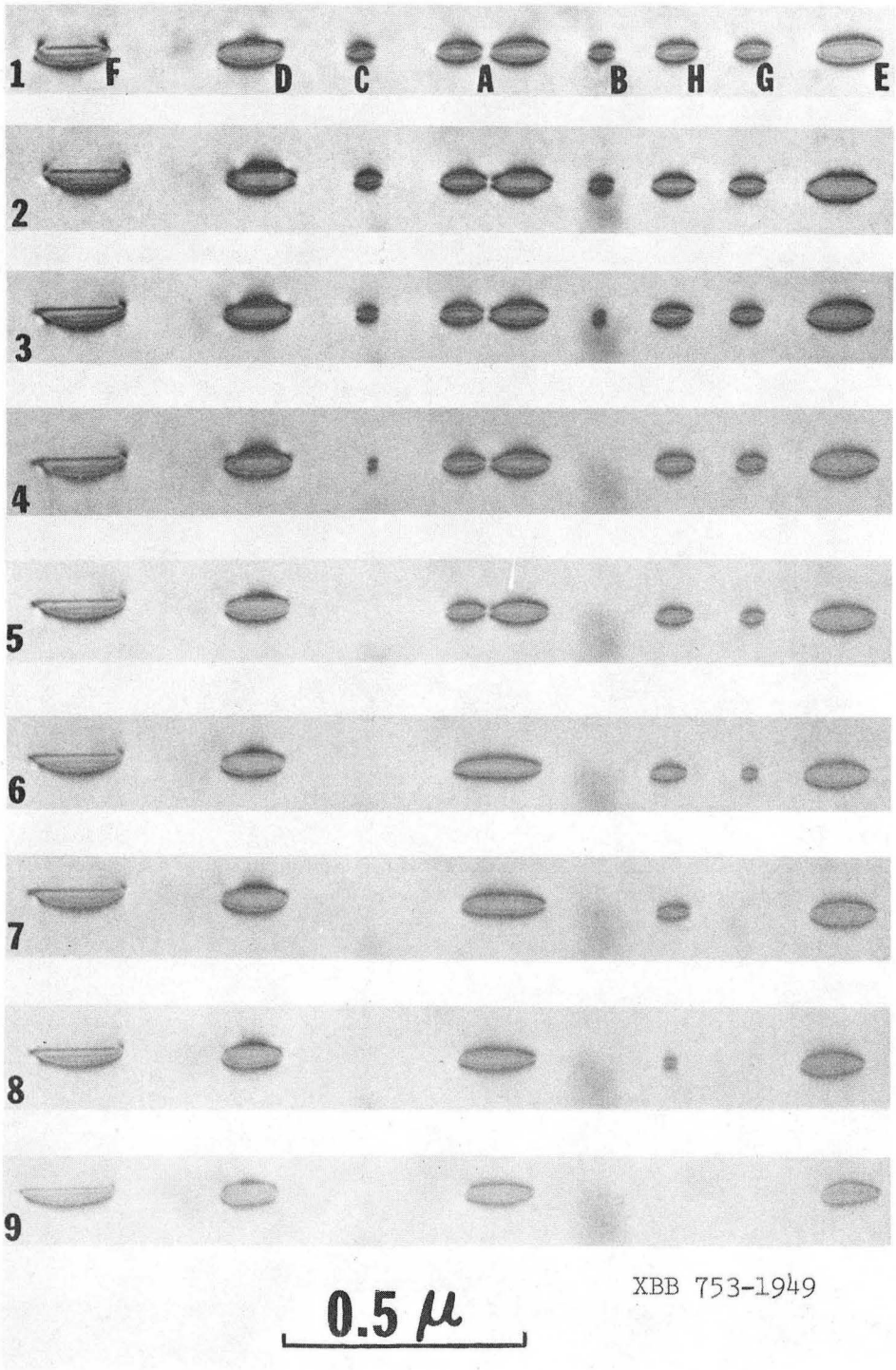

XBB 753-1949

Fig. 28

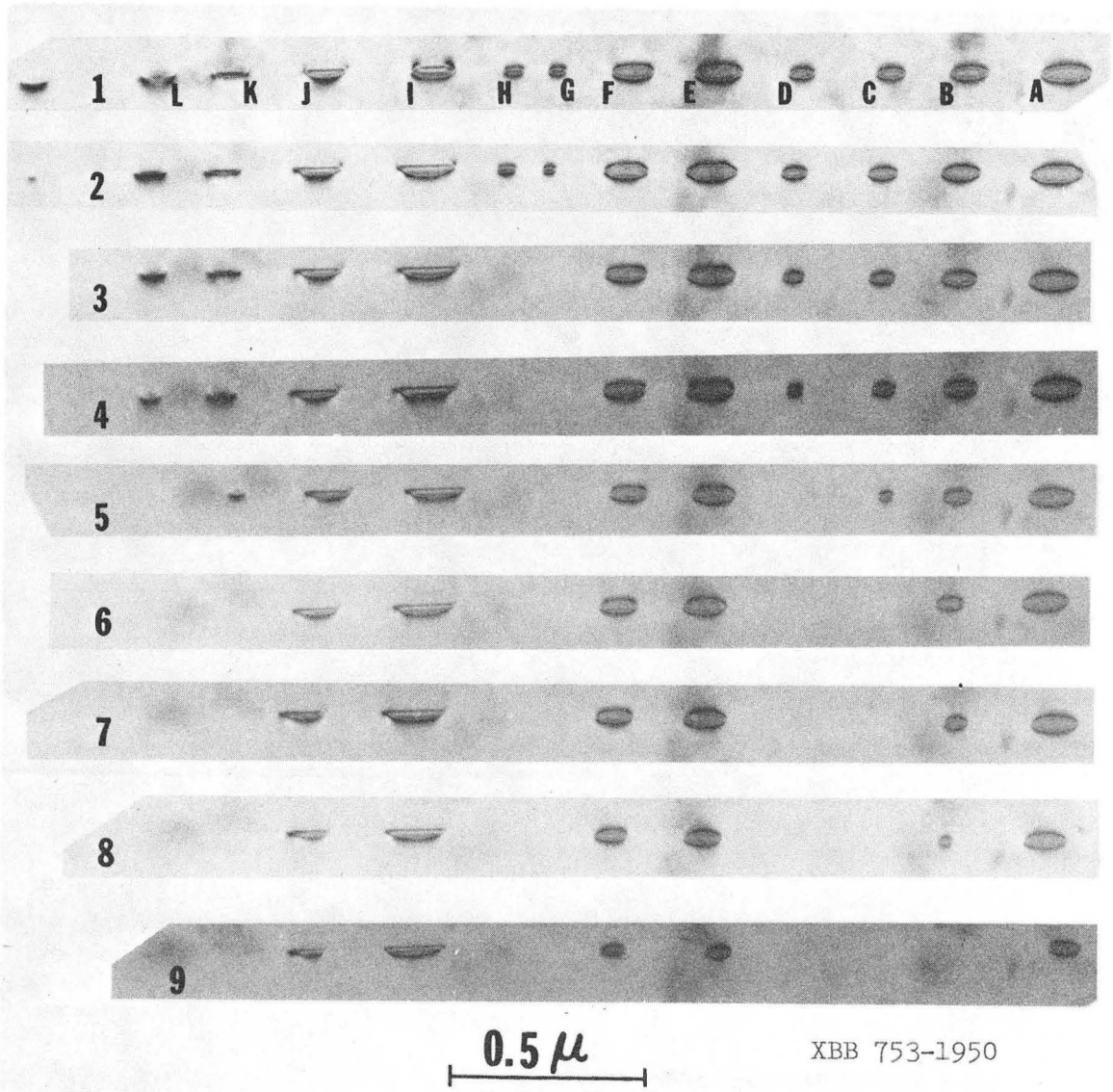

XBB 753-1950

Fig. 29

0 0 0 0 4 3 0 2 9 9 5

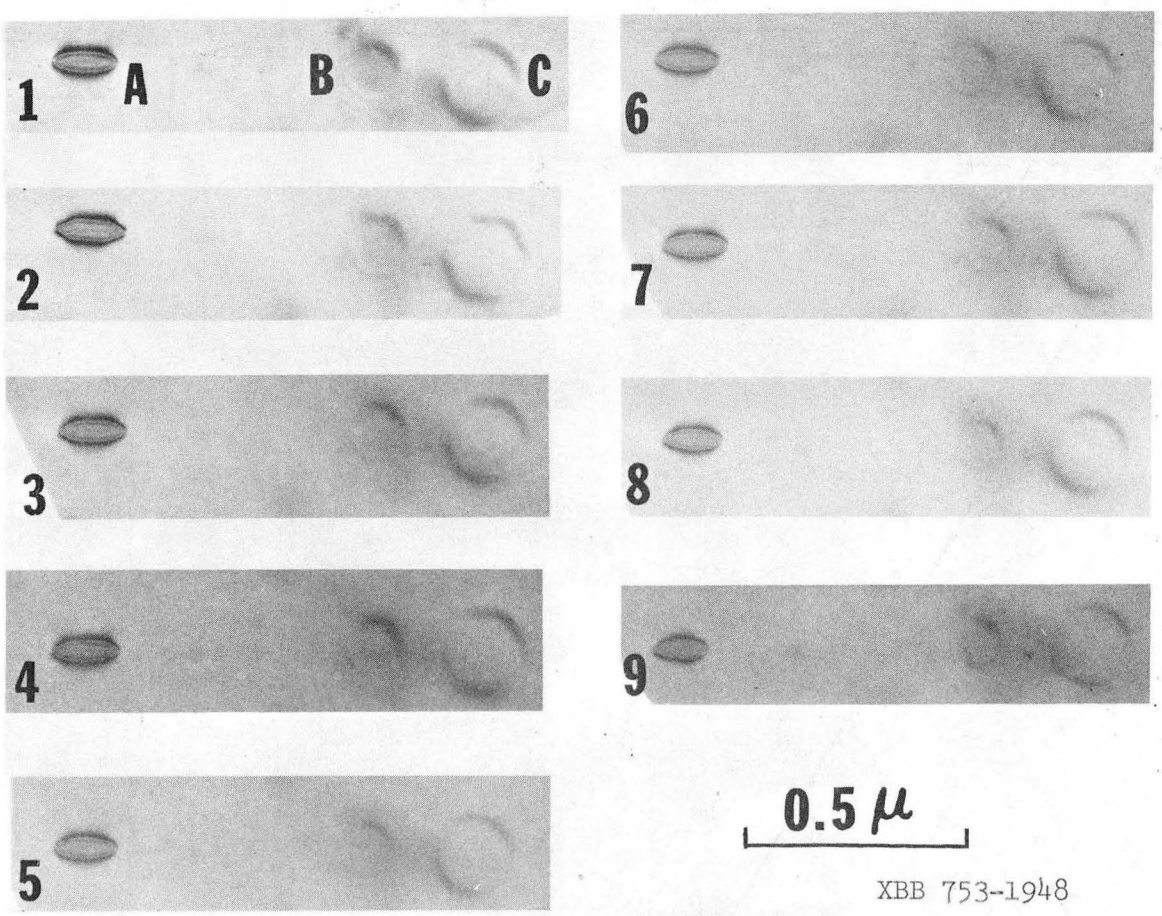

XBB 753-1948

Fig. 30

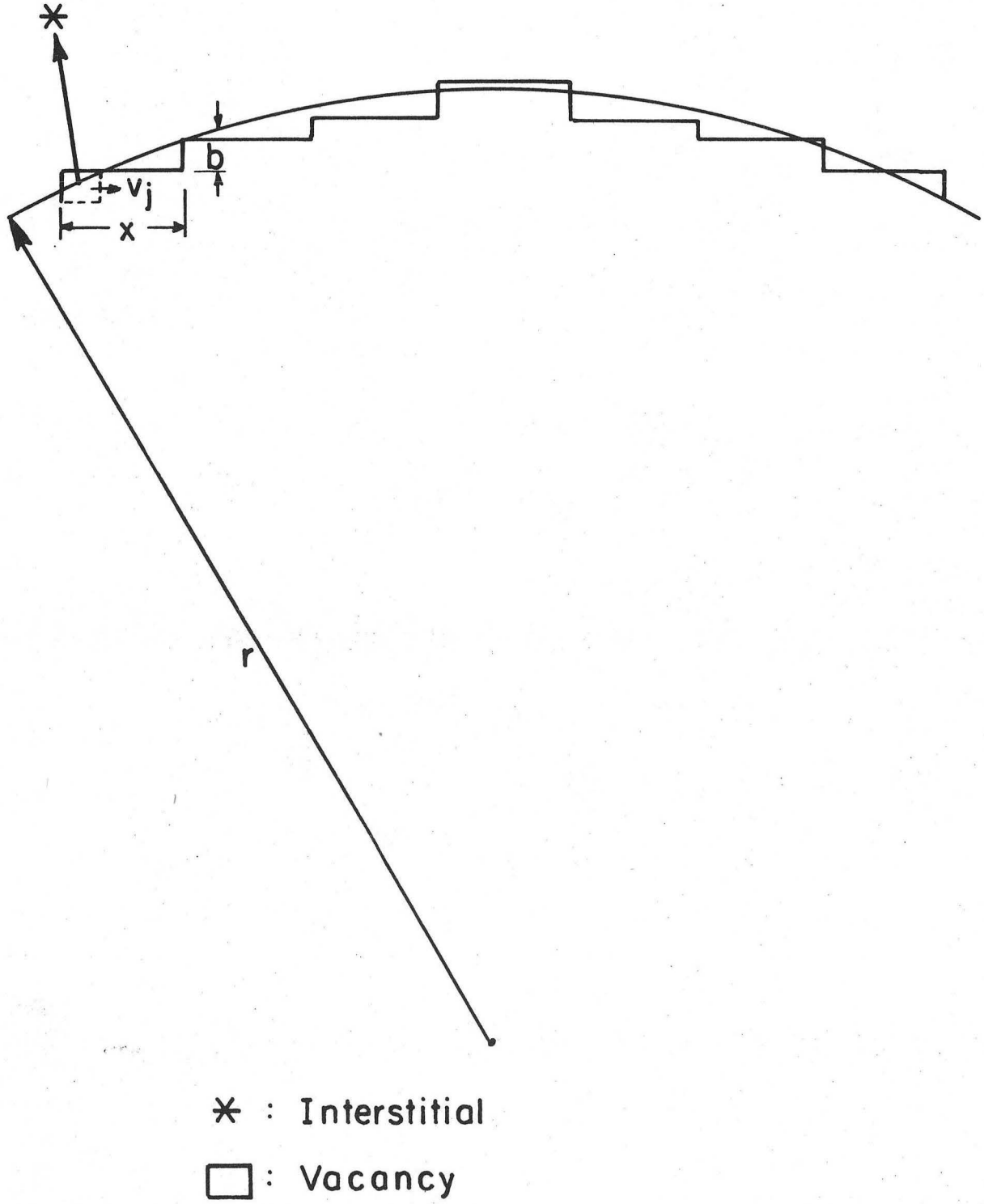

XBL 753-5956

Fig. 31

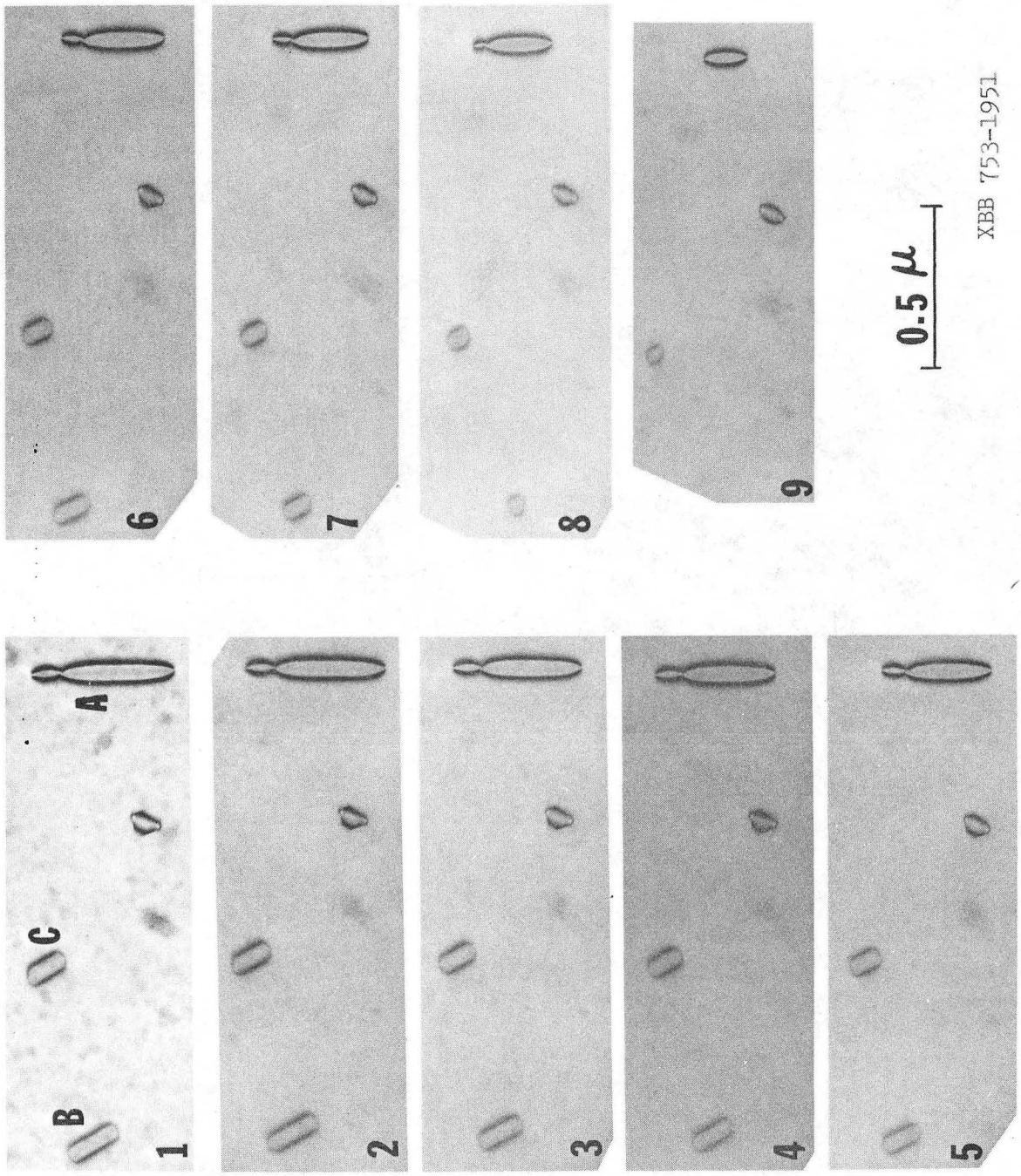

XBB 753-1951

Fig. 32

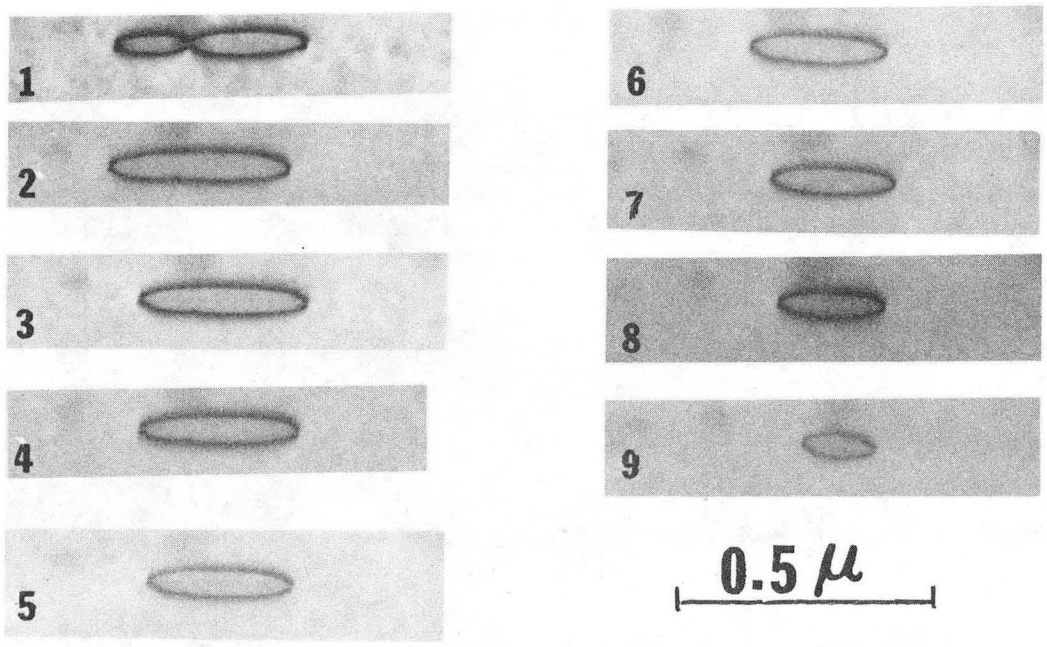

XBB 753-1952

Fig. 33

0 0 0 0 4 3 0 2 9 9 7

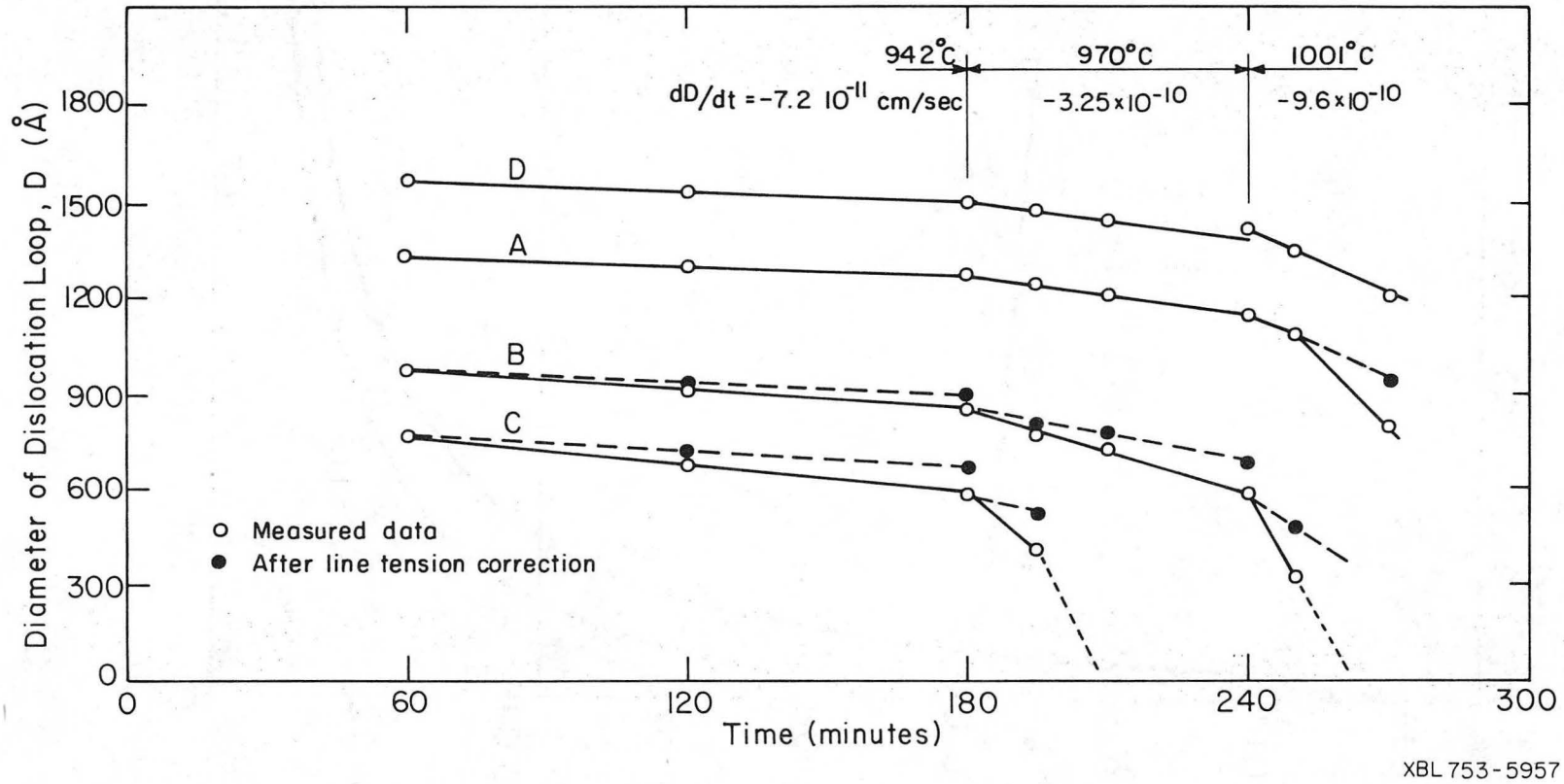

Fig. 34

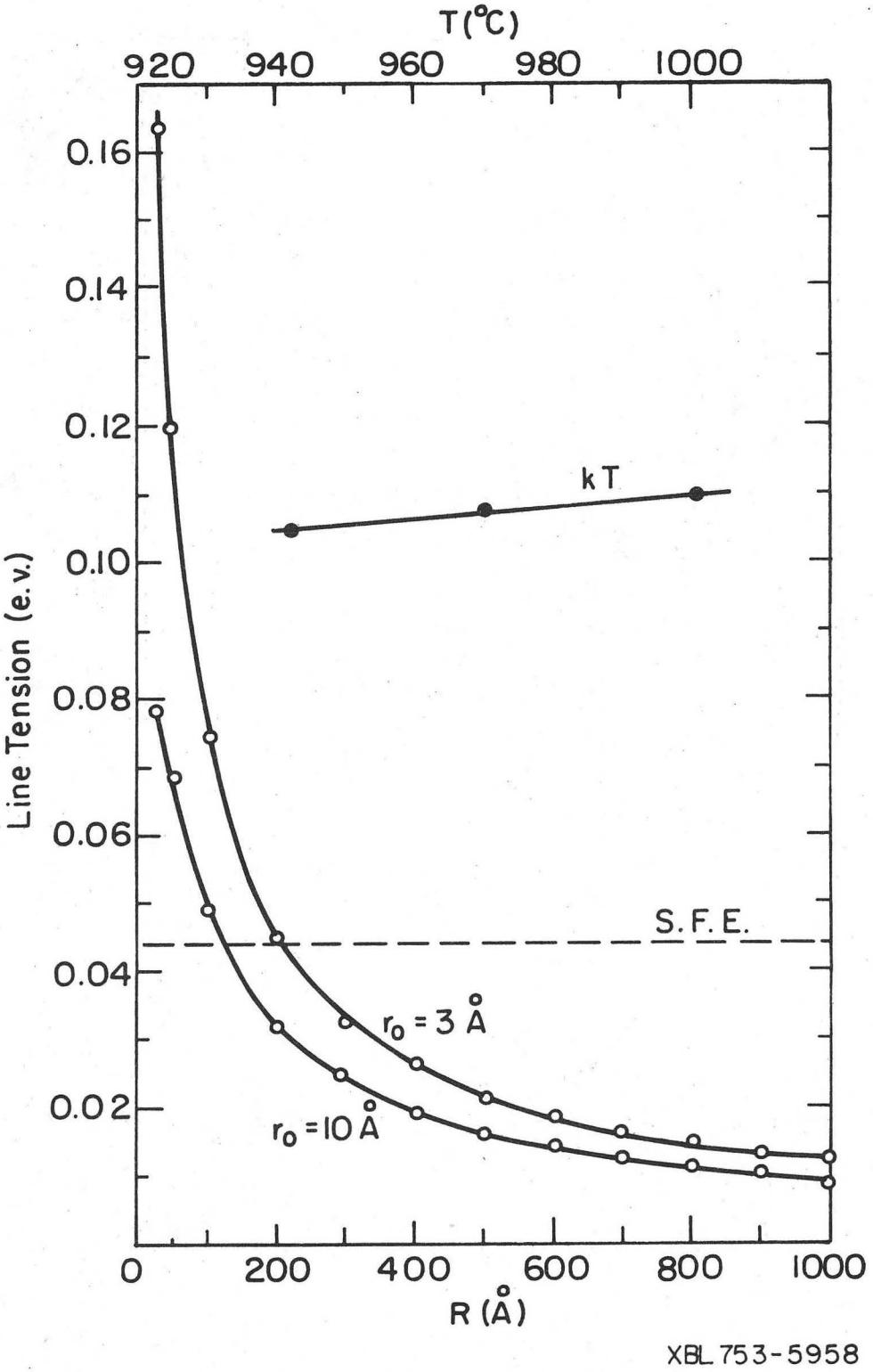
T(°C)
920
940
960
980
1000
0.16
0.14
0.12
0.10
0.08
0.06
0.04
0.02
Line Tension (e.v.)
kT
S.F.E.
r_0 = 3 Å
r_0 = 10 Å
0
200
400
600
800
1000
R (Å)
XBL 753-5958

Fig. 35

0 0 0 0 4 3 0 2 9 9 8

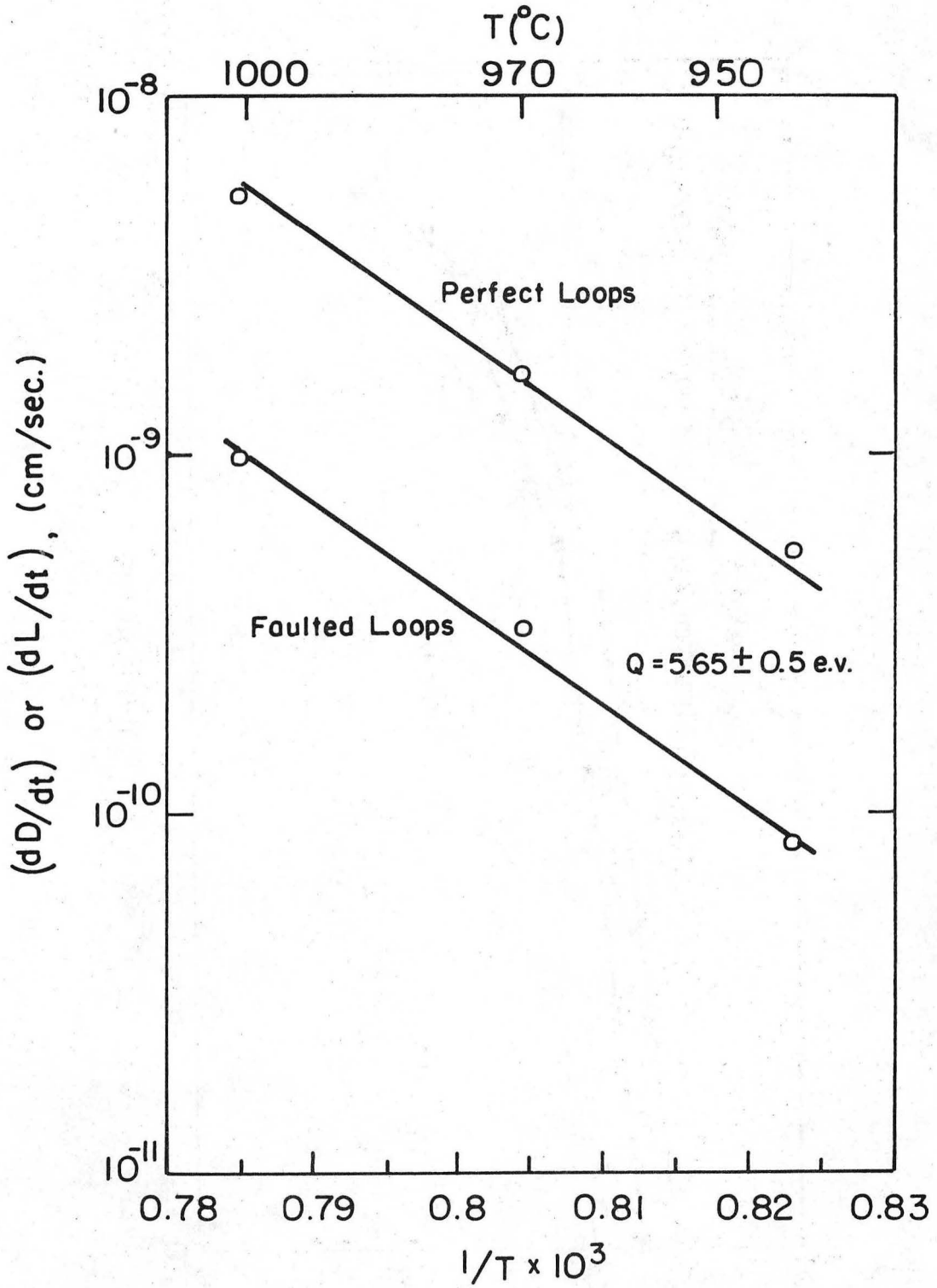

XBL753-5959

Fig. 36

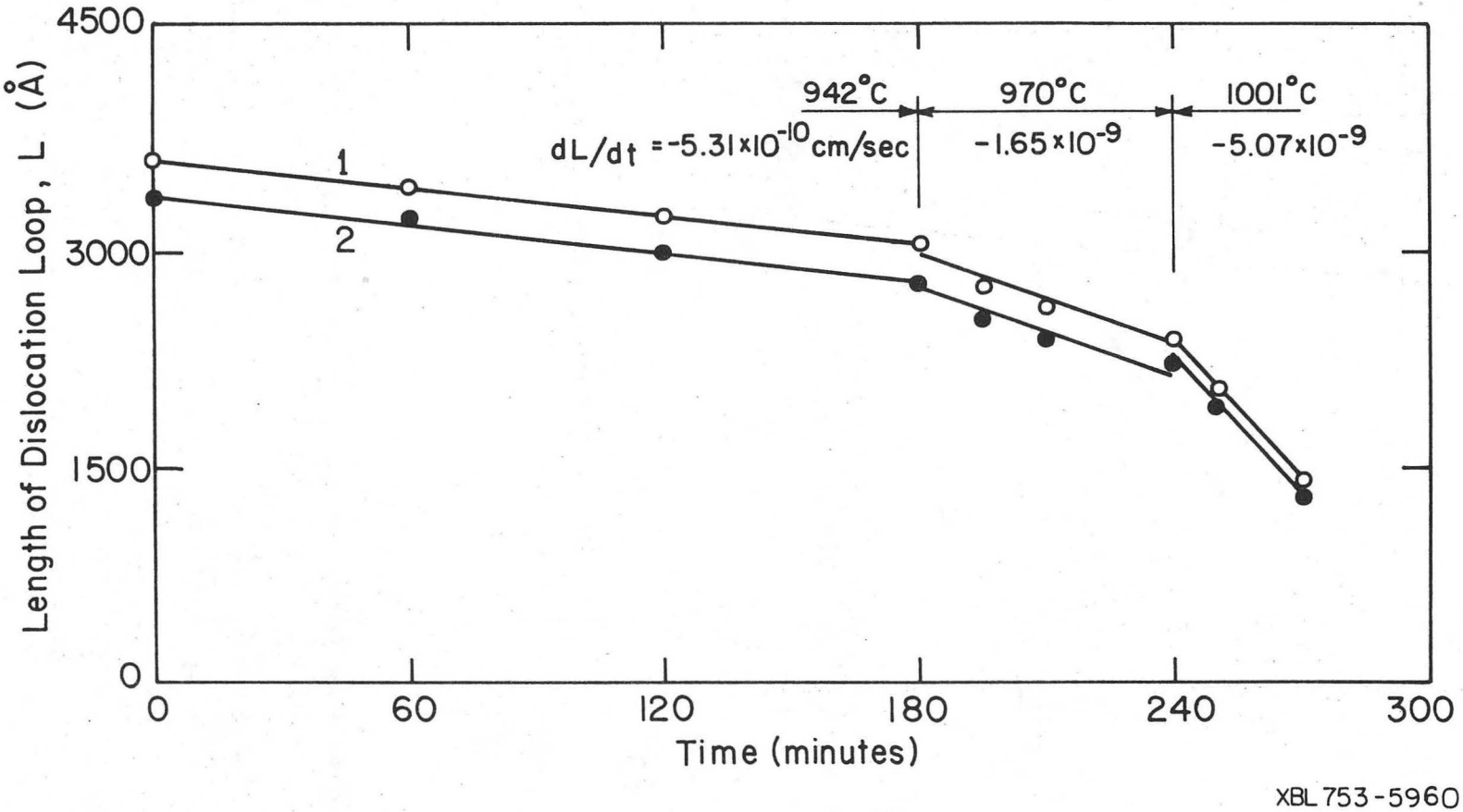
4500
3000
1500
0
Length of Dislocation Loop, L (Å)
0
60
120
180
240
300
Time (minutes)
942°C
970°C
1001°C
dL/dt = -5.31×10^-10 cm/sec
-1.65×10^-9
-5.07×10^-9
1
2
XBL 753-5960

Fig. 37

0 0 0 0 4 3 0 2 9 9 9

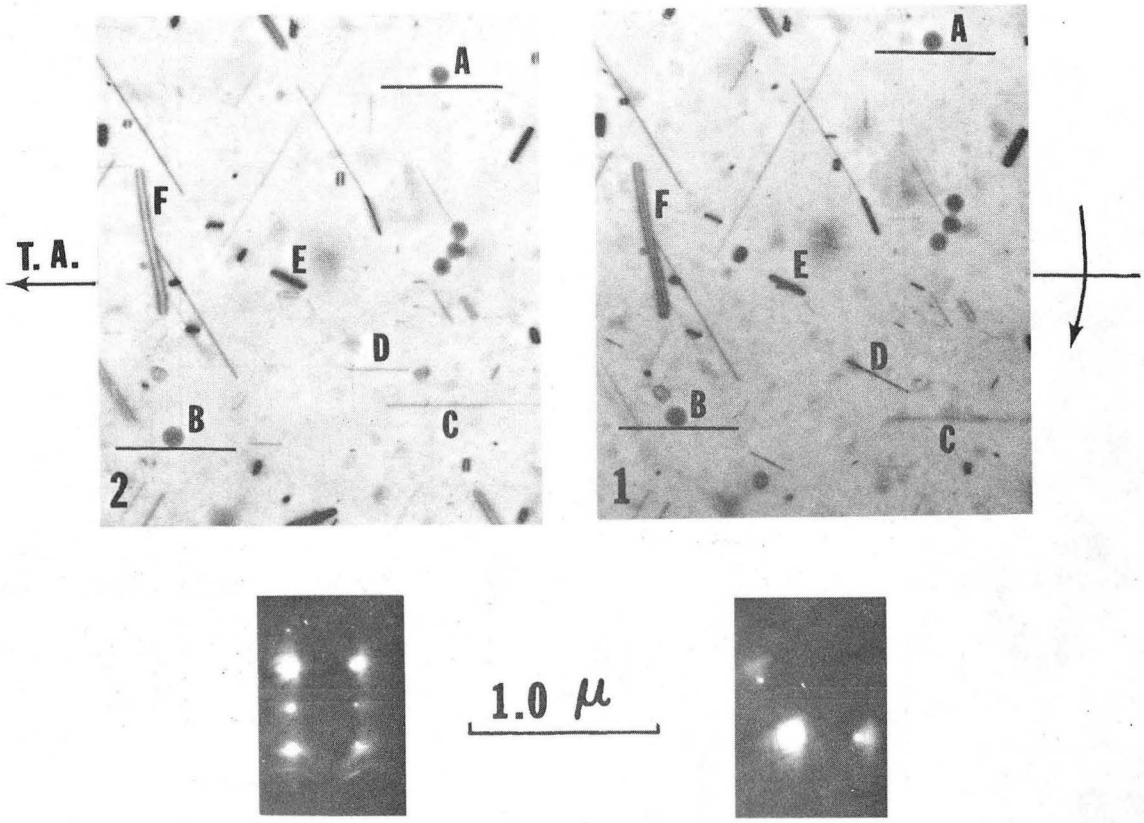

XBB 753-1947

Fig. 38

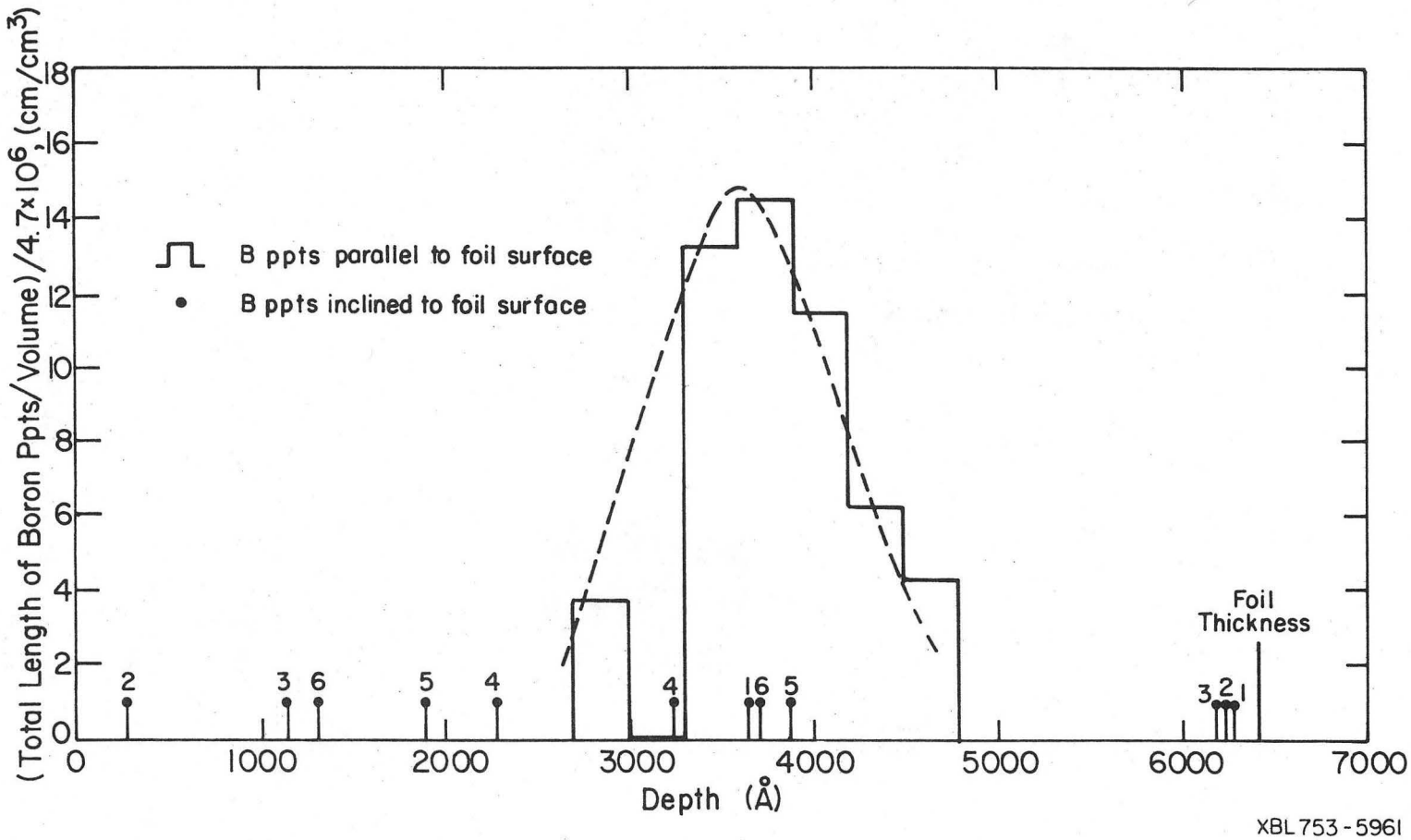
(Total Length of Boron Ppts/Volume)/4.7×10^6 (cm/cm^3)
0
2
4
6
8
10
12
14
16
18
B ppts parallel to foil surface
B ppts inclined to foil surface
2
3 6
5
4
4
16 5
3 2 1
Foil Thickness
0
1000
2000
3000
4000
5000
6000
7000
Depth (Å)
XBL 753-5961

Fig. 39

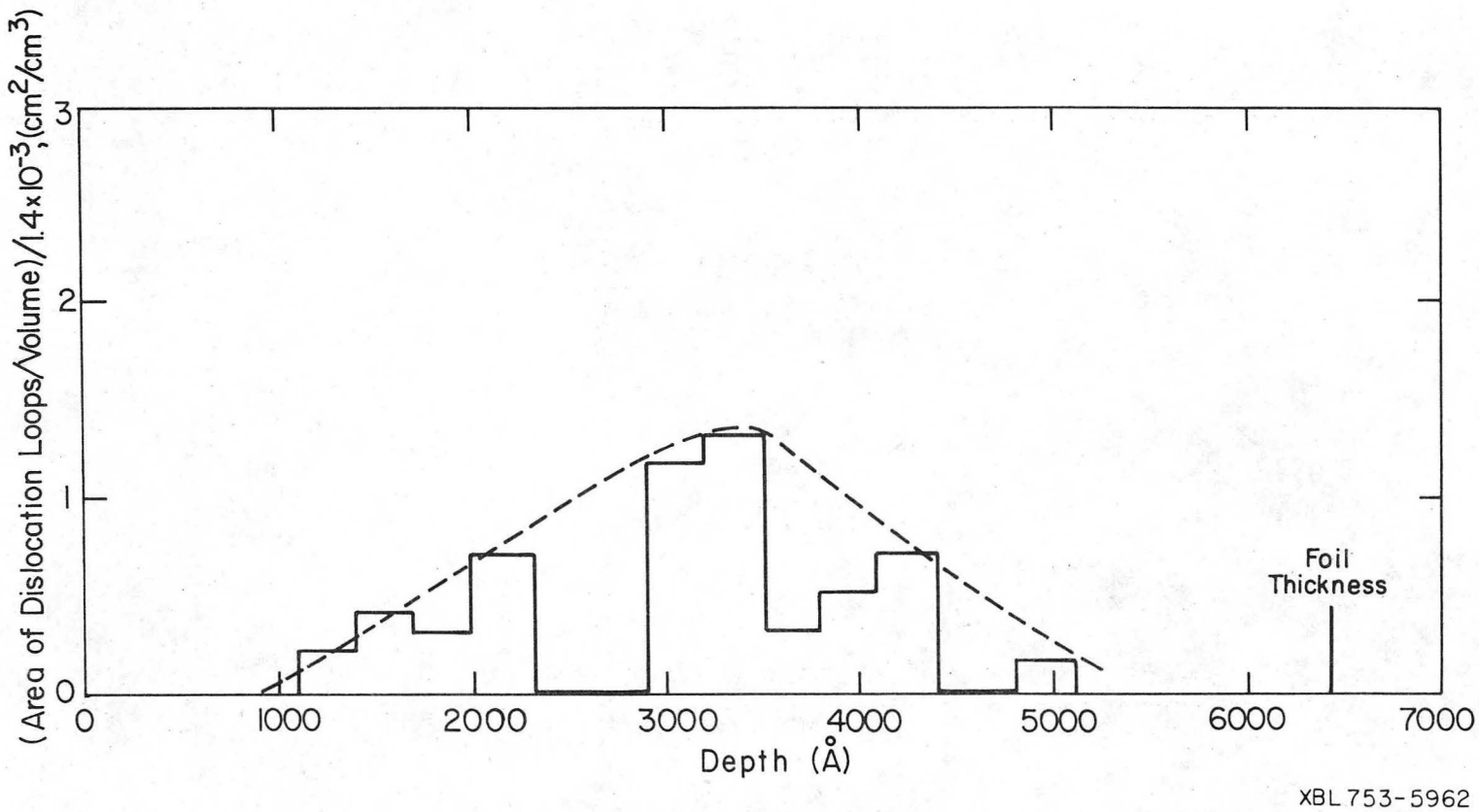

Fig. 40

0 0 0 0 4 3 0 3 0 0 0

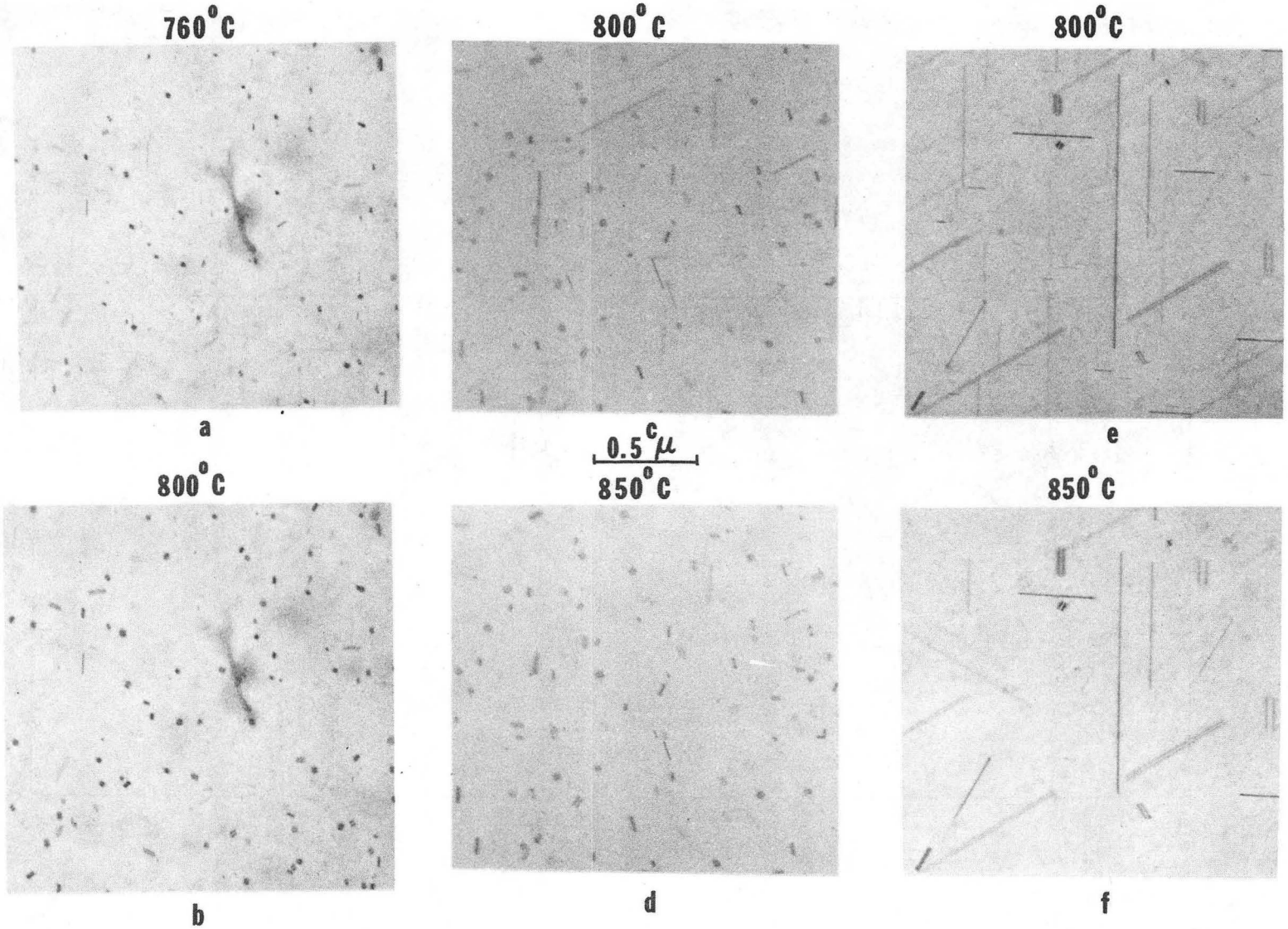

Fig. 41

XBB 753-1849

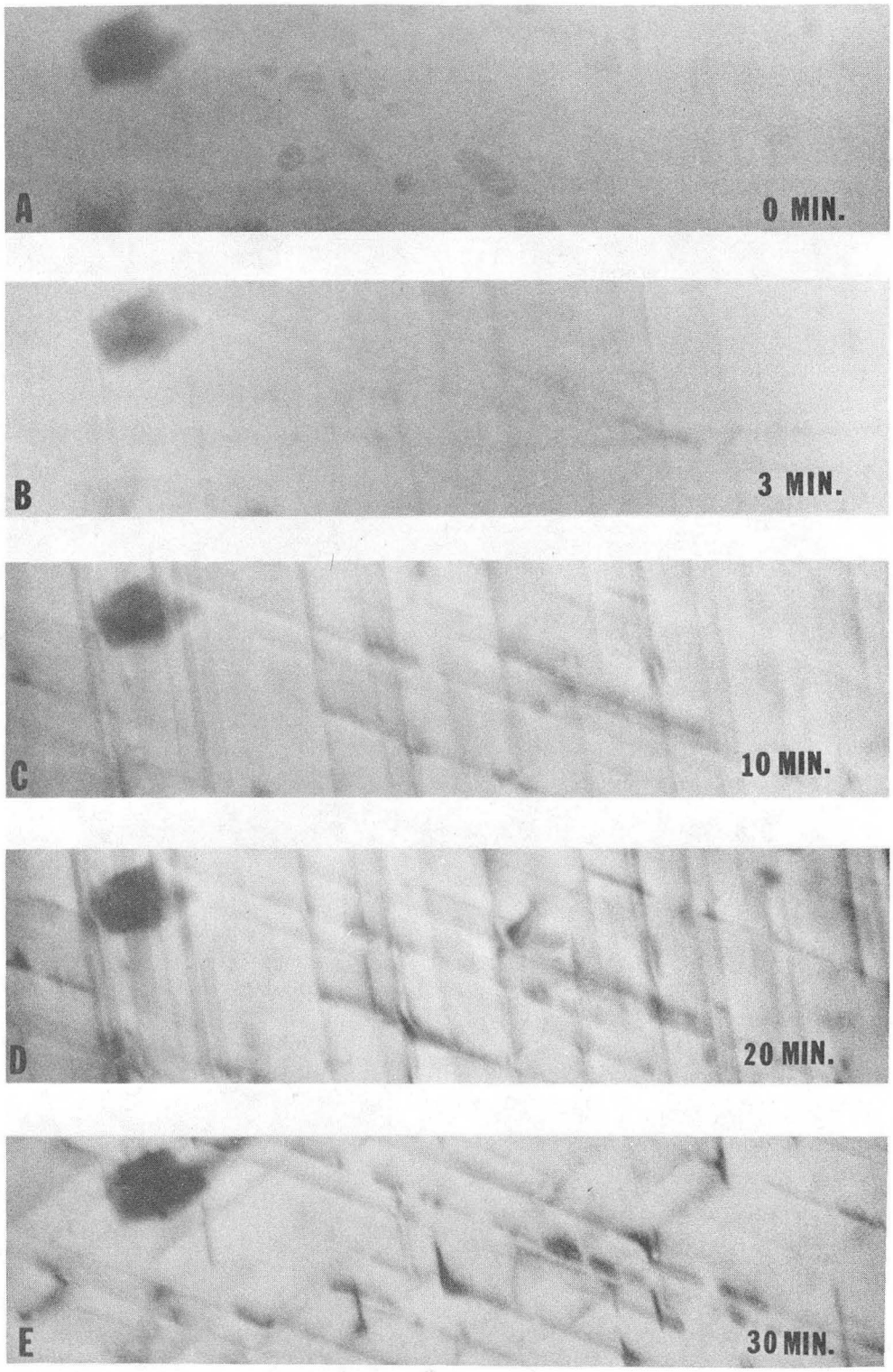

XBB 753-1857

Fig. 42

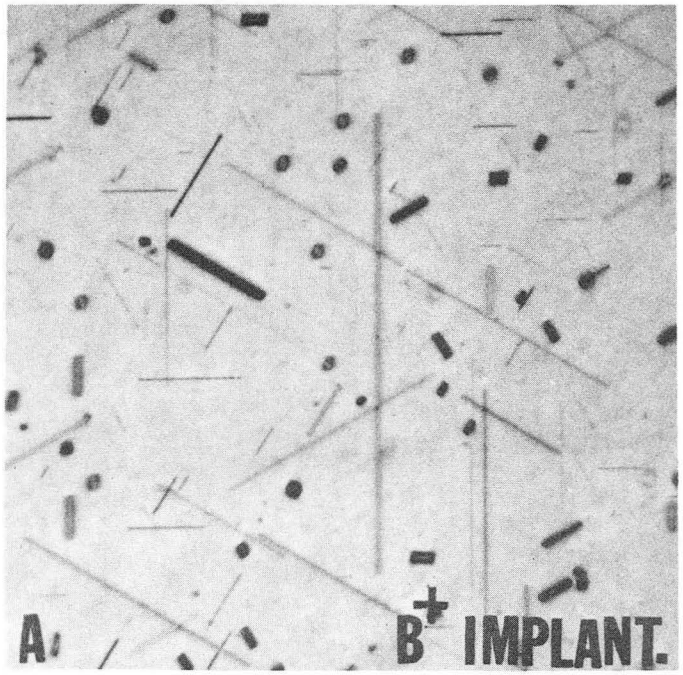

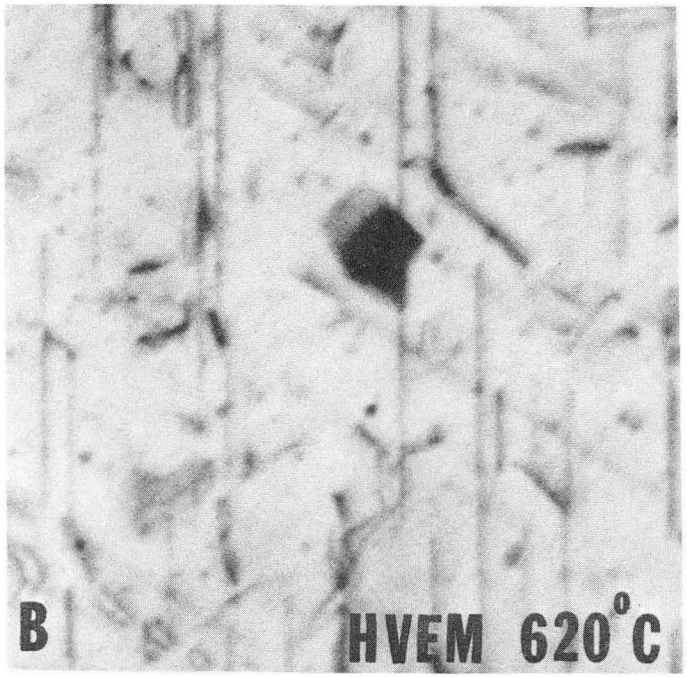

XBB 753-1852

Fig. 43

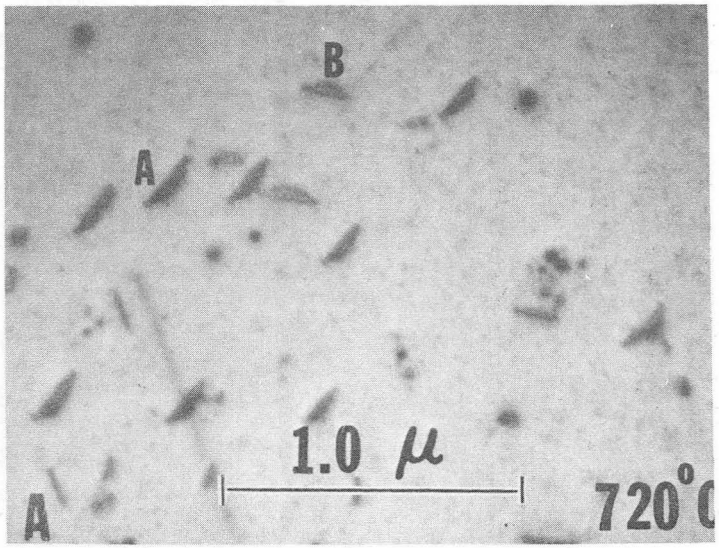

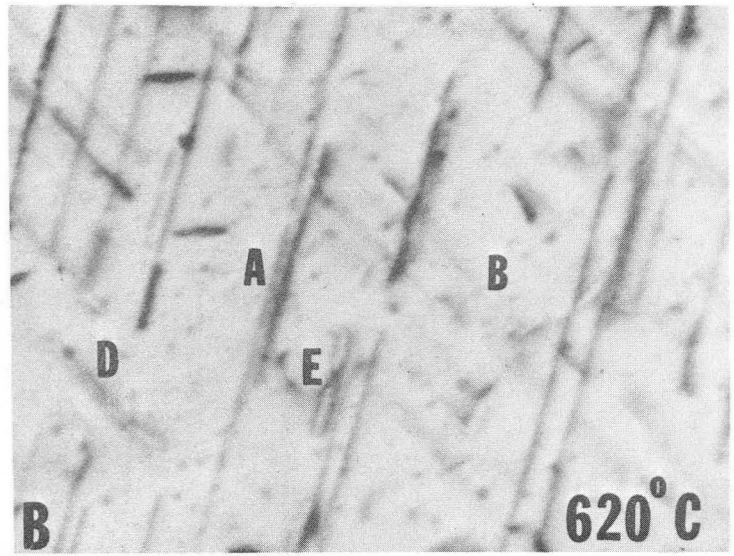

XBB 753-1853

Fig. 44

0 0 0 0 4 3 0 3 0 0 2

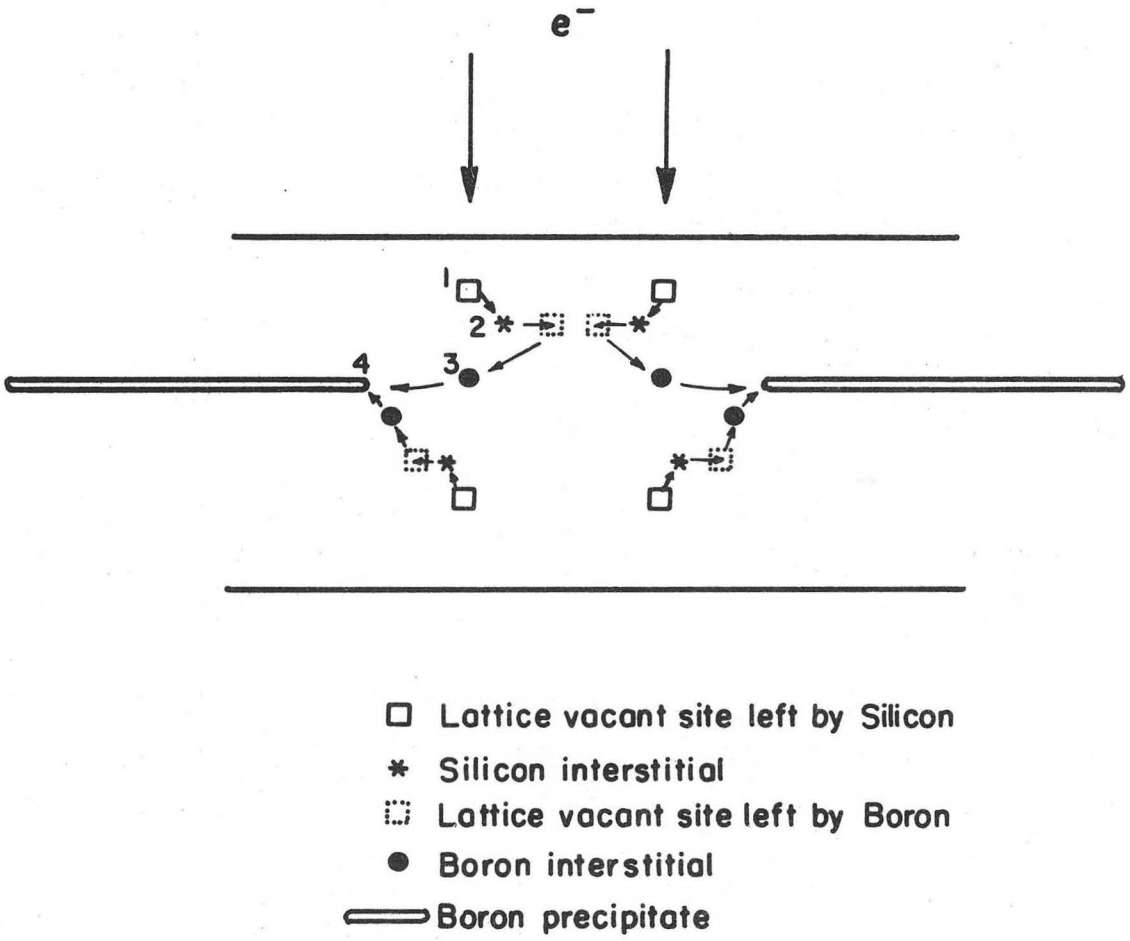

XBL 754-6196

Fig. 45

0 0 0 0 4 3 0 3 0 0 3

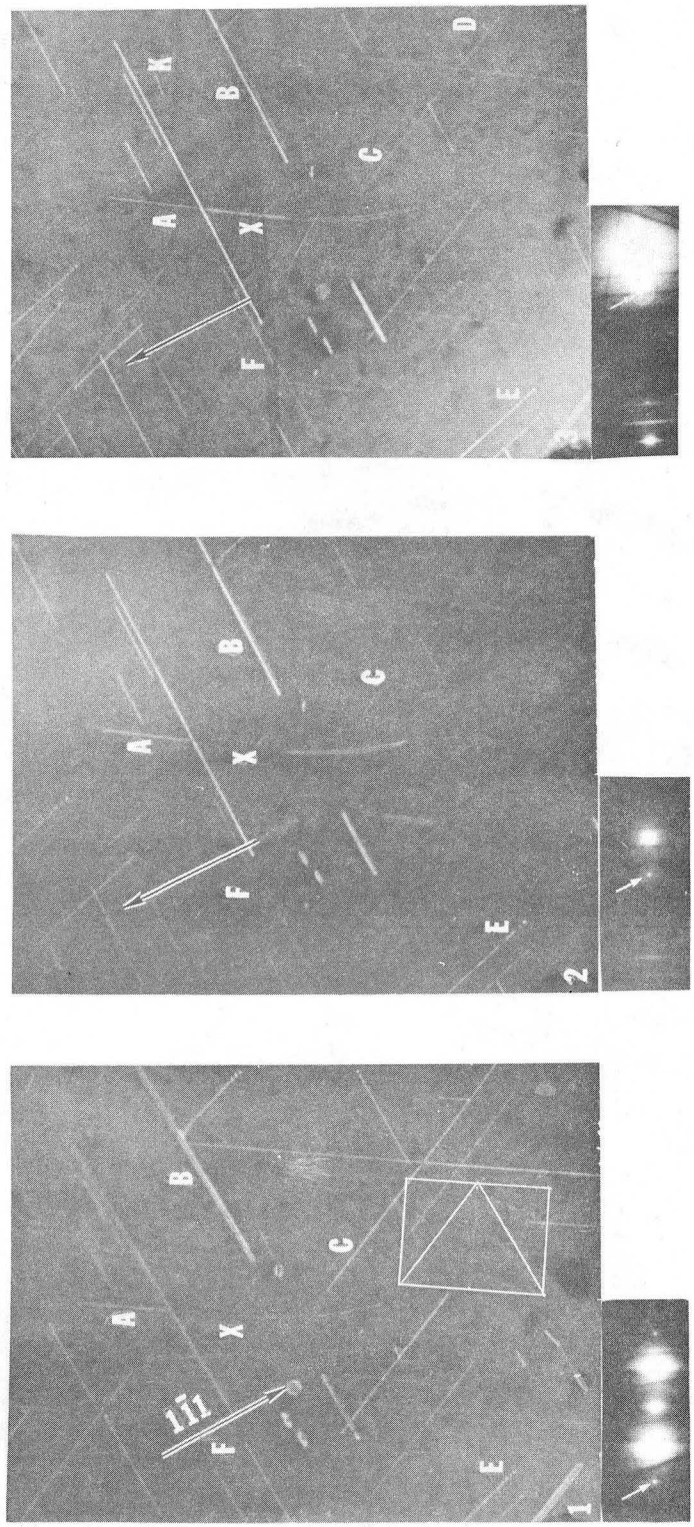

XBB 754-3183

0 0 0 0 4 3 0 3 0 0 4

LEGAL NOTICE

This report was prepared as an account of work sponsored by the United States Government. Neither the United States nor the United States Energy Research and Development Administration, nor any of their employees, nor any of their contractors, subcontractors, or their employees, makes any warranty, express or implied, or assumes any legal liability or responsibility for the accuracy, completeness or usefulness of any information, apparatus, product or process disclosed, or represents that its use would not infringe privately owned rights.

TECHNICAL INFORMATION DIVISION
LAWRENCE BERKELEY LABORATORY
UNIVERSITY OF CALIFORNIA
BERKELEY, CALIFORNIA 94720